Electrochemical Storage of Lithium in Silicon - Morphological Analysis from the Atomistic Scale to the Macroscale

Dissertation

zur Erlangung des akademischen Grades

Doctor rerum naturalium
(Dr. rer. nat.)

im Fach Physik
eingereicht an der

Mathematisch-Naturwissenschaftlichen Fakultät
der Humboldt-Universität zu Berlin

von

M.Sc. Arne Ronneburg

Präsident der Humboldt-Universität zu Berlin
Prof. Dr.-Ing. Dr. Sabine Kunst

Dekan der Mathematisch-Naturwissenschaftlichen Fakultät
Prof. Dr. Elmar Kulke

Erste/r Gutachter/in: Prof. Dr. Matthias Ballauff

Zweite/r Gutachter/in: Prof. Dr. Gerd Schneider

Dritte/r Gutachter/in: Prof. Dr. Svetlana Santer

Tag der mündlichen Prüfung: 23.04.2021

Curiosity is the key to problem solving

— **Galileo Galilei**
Italian physicist and engineer

Abstract

Silicon electrodes receive great interest as potential electrode material in lithium-based batteries due to their one order of magnitude higher capacity. This is accompanied by a volume expansion of up to 310 %, leading to an accelerated capacity loss of the electrodes. The volume expansion creates mechanical stress, leading to fracturization of the electrode and the continuous growth of the solid-electrolyte-interphase (SEI) layer under the consumption of active material.
The aim of this thesis is to investigate the morphological changes of silicon electrodes during lithiation/delithiation. Especially *operando*-techniques are well-suited to investigate these morphological changes since they allow us to precisely link structural data and the electrochemical state. Single-crystal silicon electrodes were used since this is a well-defined model system without additives and therefore well-suited to study the lithiation process. In total, three different projects were conducted during this thesis:
The first project uses *operando* neutron reflectometry (NR) and *in-situ* electrochemical impedance spectroscopy (EIS) to analyze the morphology change of the silicon surface on the nanometer-scale. The growth and shrinkage of the lithiated layers within the electrode as well as the lithium concentration was determined with this method. An SEI-layer forms on top of the silicon electrode in the delithiated state, which hinders the lithium uptake in the initial part of the subsequent lithiation. Once this layer is electrochemically dissolved, the lithiation takes place. EIS reveals an increased charge transfer resistance in the delithiated state, which is in line with the observed layer formation. The second project analyzes the morphology-change of the electrode on the µm-scale. Here the fracturization of the silicon electrode is investigated by *operando* X-ray phase-contrast radiography. Again, *in-situ* EIS was performed to probe the electrochemical properties of the sample, but also additional *ex-situ* Laue diffraction and focussed ion beam scanning electron microscopy (FIB/SEM) was done tho reveal depth-dependent information. A rectangular fracturization pattern was observed during the delithiation, which vanished again during the lithiation. The fractures reappear on the same position again in the subsequent cycle. Although the pattern spreads over the electrode with cycle number, the average size of the fracture pattern unit stays constant. The third project investigates the influence of an artificial coating layer on the lithiation process. Again *operando* NR was chosen as analysis tool. The artificial coating decreased the formation of the SEI-layer within the first cycles, but did not suppress it completely. The increase of the charge transfer resistance value in the delithiated state can still be found. However, this layer degraded already in an early stage of cycling, resulting in the occurence of side reactions afterward.

Zusammenfassung

Silizium-Elektroden werden aufgrund ihrer um eine Größenordnung höheren Kapazität als mögliches Elektrodenmaterial in Lithium-Ionen-Batterien betrachtet. Diese Kapazität geht jedoch mit einer Volumenausdehnung von bis zu 310 % einher. Dies begünstigt einen schnellen Kapazitätsabfall und erzeugt mechanische Spannungen und Risse in der Elektrode. Die Ausdehnung führt auch zu einem kontinuierlichen Wachstum der SEI-Schicht. Dies geschieht unter Verbrauch von Elektrolyt und elektrochemisch aktivem Material und ist daher eine weitere Alterungserscheinung.Ziel dieser Arbeit ist es daher, die Morphologie-Änderung der Siliziumelektrode während des Lithiierungs-Prozesses besser zu verstehen. Dazu wurden insbesondere *operando*-Methoden gewählt, da sie eine direkte Verknüpfung von Struktur und elektrochemischem Zustand der Zelle ermöglichen. Eine Silizium-Einkristall-Elektrode wurde als Modellsystem genutzt. Hier kann der Lithiierungsvorgang an einem Modellsystem studiert werden, ohne den Einfluss von Binder, Leitfähigkeits-Zusätzen oder spezieller Morphologien. Diese Arbeit besteht aus 3 Teilen:
Im ersten Teil wurde Neutronenreflektometrie (NR) genutzt, um die Morphologie-Änderung auf der Nanometerskala einer Siliziumelektrode zu untersuchen. Das Wachsen/Schrumpfen der lithiierten Zone im Silizium wurde beobachtet und die Lithium-Konzentration bestimmt. Auf der Oberfläche der Elektrode wächst im delithiierten Zustand eine Grenzschicht, welche die Lithiierung verhindert. Nachdem diese Schicht aufgelöst ist, kann Lithium eingelagert werden. Zusätzlich wurde mittels elektrochemischer Impedanzspektroskopie (EIS) ein erhöhter Ladungs-Transfer-Widerstand im delithiierten Zustand bestimmt. Dies deckt sich mit dem beobachteten Grenzschicht-Wachstum.
Im zweiten Teil wurde die µm-Skala analysiert. Hierbei wurde *operando* Röntgen-Phasenkontrast-Radiographie genutzt sowie zusätzliche EIS-Messungen, Mikroskopie-Techniken und Laue-Diffraktion. Ein rechteckiges Riss-Gitter wurde dabei im delithiierten Zustand beobachtet, welches sich während der Lithiierung schließt. Dieses Gitter ist entlang der Kristallachsen des Siliziums orientiert. Im nächsten Zyklus entsteht das Gitter am selben Ort wieder, und breitet sich mit steigender Zyklenzahl über die Elektrode aus. Die durchschnittliche Größe der Gitterzellen bleibt jedoch konstant. Fokussierte Ionenstrahl-/Rasterelektronen-Mikroskopie liefert Zusätzliche Tiefeninformationen.
im dritten Teil wurde der Einfluss einer künstlichen Grenzschicht auf die Lithiierung untersucht. Erneut wurde NR genutzt. Die künstliche Schicht verringert das Wachstum der SEI-Schicht, unterdrückt es jedoch nicht komplett, da weiterhin eine erhöhter Ladungs-Transfer-Widerstand im delithiierten Zustand beobachtet wird. Nach 2 Zyklen ist die Grenzschicht degradiert, und Seitenreaktionen können beobachtet werden.

Contents

Chapter 1

Introduction

1.1 Motivation

Without any doubt, batteries are of high importance for our daily life. They serve as a power source for mobile applications such as watches or mobile phones. Moreover, electric cars experience increasing interest again to protect the environment and decrease greenhouse gas release. A sustainable electrical power supply based on renewable energy sources also requires energy storage systems such as batteries due to the fluctuating nature of wind and solar energy. Therefore, each improvement in battery technology has a big influence in many parts of our modern life.
The history of batteries began in the 18^{th} century. First electrochemical experiments were accidentally conducted by Galvani, while he studied the anatomy of a frog. Around 1800 Alessandro Volta introduced the Voltaic pile [1]. This was the first electrical power supply available and paved the way for many new findings, such as the electrolysis of water, electric light, or the synthesis of unknown compounds. Of course, these batteries were not as powerful as the modern state-of-the-art

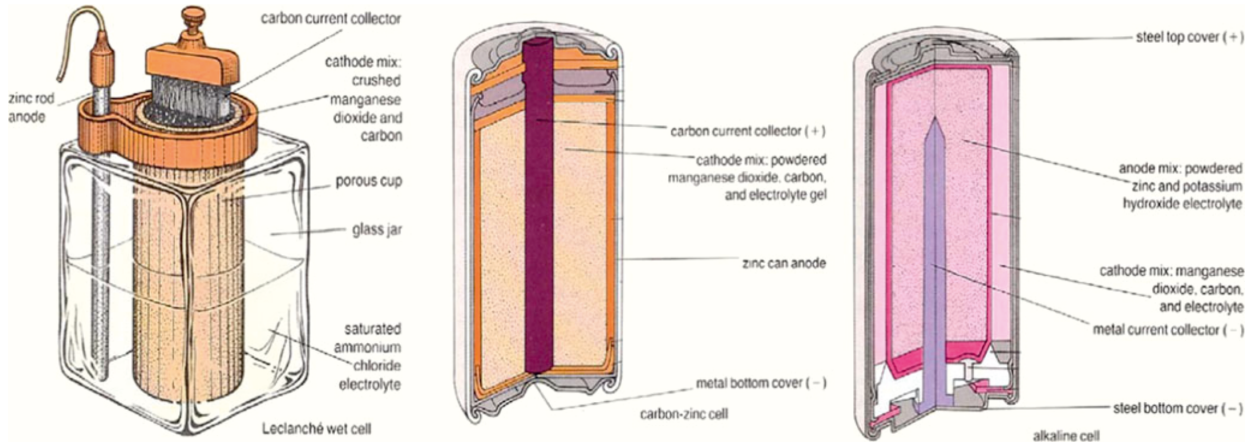

Figure 1.1: Evolution of the battery. On the left is the Leclanchè cell invented in 1866. Their today's counterparts are shown in the middle (carbon-zinc cell) and on the right (alkaline cell). The general principle is still similar. Taken from [1], with permission from Springer Nature.

battery, which is the lithium-ion-battery(LIB). Fig. 1.1 shows the historic Leclanchè cell and its modern adaptations. Figure 1.2 shows the general working principle of a modern LIB [2]. The setup consists of two electrodes in contact with an electrolyte, lithium ions serve as redox-active species. A half cell reaction occurs at each electrode, namely oxidation (on the anode) and reduction (on the cathode), which sum up into a redox-reaction. Each half cell reaction has a specific working potential. The overall cell voltage is the difference between the individual working potentials of the half cells. Therefore, the cell voltage depends on the employed materials. Fig. 1.3 gives an overview of several materials commonly used as anode or cathode and their working potential [2].
The capacity of the half cell is determined by the employed materials, too. In conventional electrodes such as graphite, Lithium ions are stored within the electrodes via an intercalation mechanism, meaning the lithium is inserted into the electrode's crystal lattice [3]. The available storage sites and, therefore, the storage capacity depend on the amount of available material. Common electrodes for LIBs are graphite as anode and metal oxides (such as $LiCoO_2$ or $LiFePO_4$) [4]. Figure 1.3 also gives an overview of several electrode capacities. An ionic conductor, the electrolyte, connects both electrodes. This enables an ionic current between the two electrodes. Different organic solvents and dissolved lithium salts are employed as electrolyte [5, 6]. The electrolyte should be stable towards the electrodes, meaning it should exhibit a large stability window or form a stable SEI-layer to suppress further decomposition [7–11]. However, also the formation of a stable SEI-

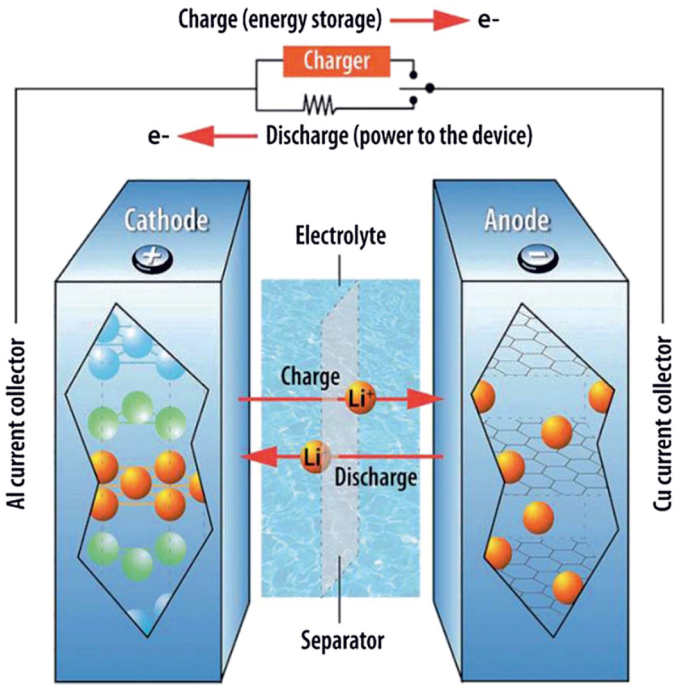

Figure 1.2: Scheme of a Lithium-ion battery (LIB). During discharge, lithium is oxidized on the anode. The ions travel from the anode to the cathode through the electrolyte whereas the electrons move through the outer connection, where the electrical consumer is connected. The inverse process happens during charge. See also 2.5 for further information. Taken from [2] with permission from RSC.

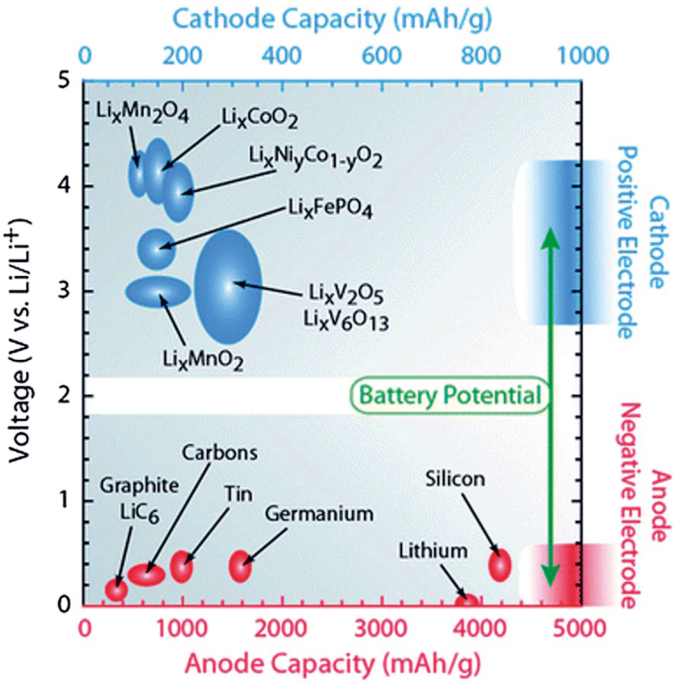

Figure 1.3: Voltage of various electrode materials. The cell voltage is the difference between the cathode potential and the anode potential. Currently, graphite is the most used anode. Taken from [2]. Permission granted from RSC.

layer can suppress the electrolyte decomposition [10]. The electron passes through the electrical connection on the outside and electrical work can be done. LIB show the highest specific capacity and power density among the available battery systems [1, 12, 13].

However, LIB as the state-of-the-art battery system also has some drawbacks, which come with the potential for further improvements. One drawback is the usage of flammable materials and the danger of lithium plating and dendrite formation [12, 14]. This may induce an internal short circuit in the cell and a self-ignition. Here battery systems based on non-flammable electrolytes may help, although their performance is still limited compared to their conventional counterpart. Also, the suppression of lithium dendrite formations would increase operational safety.

The second drawback is the current electrode materials specific capacity (see fig. 1.3). Several different materials are used for the positive electrode, depending on the purpose of the system. Some examples are $LiFePO_4$ or $LiCoO_2$ or mixtures of them [3, 15]. Here much research is done on future electrode materials such as sulfur or oxygen [16]. However, the primary material for the negative electrode up to now is graphite [3, 16, 17]. It exhibits a theoretical specific capacity around 375 mAh/g or 837 mAh/ml and works via lithium intercalation into the graphite lattice, forming LiC_6 [3, 16, 18]. New electrode materials need to be employed to increase the ratio of lithium atoms per host matrix atom and therefore increase the electrode capacity. Silicon is one of the most promising candidates to replace graphite as anode [3, 18, 21]. It exhibits a theoretical gravimetric and volumetric capacity of 4200 mAh/g and 9660 mAh/ml, respectively, which is one order of magnitude

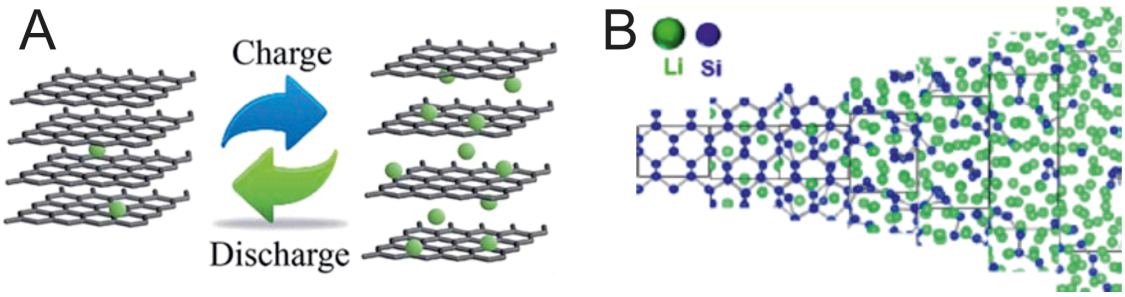

Figure 1.4: Intercalation electrodes and alloying electrodes in comparison. Part A: graphite as an example of intercalation electrodes. Lithium ions are inserted between the carbon layers, causing a small volume expansion [17]. Taken from [19], permission from RSC is gratefully acknowledged. Part B: silicon as an example of an alloying electrode. Here a lithium-silicon alloy is formed, causing a volume expansion of up to 310% [3]. Reprinted with permission from [20]. Copyright 2012 American Chemical Society.

higher than current graphite electrodes [3, 18]. The reason for this difference is a different storage mechanism. In silicon electrodes, an alloy with up to 4.4 Li-atoms per silicon atom forms upon lithiation (see also fig. 1.4). Moreover, silicon is abundant, non-toxic, widely used in industry, and the formation of dendrites is hindered [21–23].

However, the high lithium uptake results in a volume expansion of the silicon of up to 310 % [3]. This is demonstrated in figure 1.4. Mechanical stress is created within the silicon and fractures form. This leads to mechanical degradation and pulverization of the electrode [3, 18, 21]. Furthermore, a solid-electrolyte-interphase (SEI) layer is formed on the silicon electrode, which originates from the decomposition of electrolyte components. The silicon electrode's electrochemical potential is outside of the stability window of the commonly used electrolytes [18, 21, 24]. Upon lithiation, silicon expands, leading to an increased contact area of the silicon electrode with the electrolyte. This initiates a further growth of the SEI-layer, consuming electrolyte and active material [21].

Numerous studies were conducted on crystalline silicon electrodes to understand the lithiation mechanism and the mentioned drawbacks. Sharma *et al.* performed one of the first studies on silicon electrodes, revealing four distinct Li-Si-phases, their stoichiometric ratios, and the associated equilibrium potential (in ascending Li-concentration: $Li_{12}Si_7$, Li_7Si_3, $Li_{13}Si_4$, and $Li_{22}Si_5$) [26]. Unfortunately, the stepwise voltage behavior shown in fig. 1.5 is only observed at elevated temperatures around 415 °C. At room temperature, a sloping plateau around 100 mV is present, indicating the formation of an amorphous Li-Si-interphase [3, 21]. Here the formation of the Li-Si-equilibrium phases is kinetically hindered [3, 21]. However, also the formation of the Li-Si equilibrium phases was proposedd in the literature [21]. After delithiation amorphous silicon remains [3]. Obrovac *et al.* and Li *et al.* also studied this amorphization [27, 28]. They found a decreasing intensity of the Si(110) and Si(220)-diffraction peak during lithiation, caused by the amorphization. At the end of the lithiation process, another crystalline phase forms, which is $Li_{15}Si_4$. This phase is only metastable and requires electrode potentials lower than 60 mV vs. Li/Li^+ [27, 28].

In the subsequent delithiation process, a two-step process is observed. The highly lithiated phase $Li_{15}Si_4$ is consumed and an amorphous phase with lower lithium content forms. Once the highly

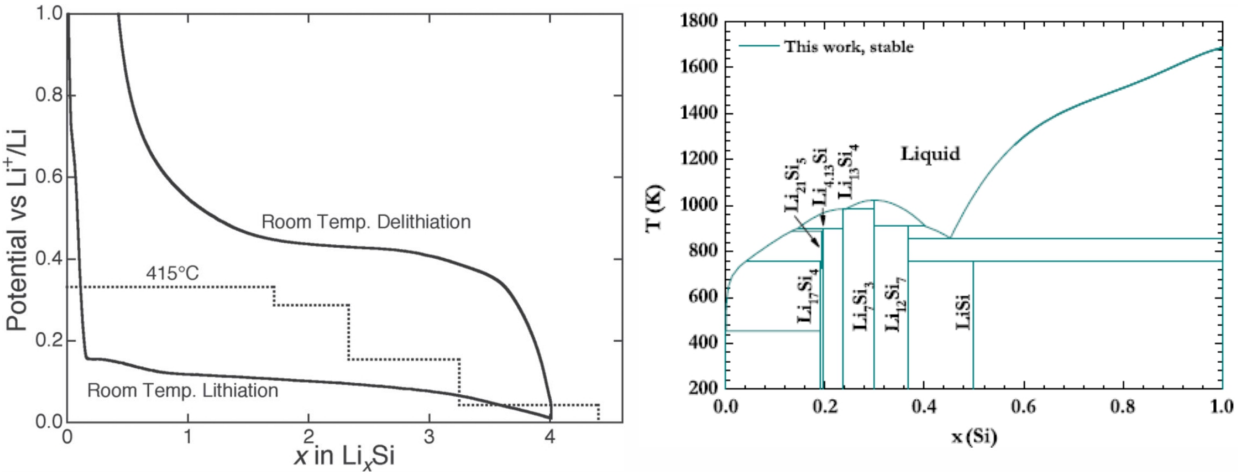

Figure 1.5: On the left: Voltage-curve vs. lithiation degree of a silicon electrode. The solid line denotes the room-temperature curve, whereas the dashed line denotes the high-temperature curve at 415 °C. With descending voltage, the following equilibrium phases are formed: $Li_{12}Si_7$, Li_7Si_3, $Li_{13}Si_4$, and $Li_{22}Si_5$. Taken from [3], permission from John Wiley and Sons is gratefully acknowledged. On the right: theoretical phase diagram of the Li-Si system. The formation of different phases is shown. Not all of them are observed during the lithiation process. Reprinted from [25] with permission from Elsevier.

lithiated phase is depleted, also the second phase is dissolved. After complete delithiation, only amorphous silicon remains [27, 28]. Therefore, the subsequent lithiation shows a slightly different lithiation curve, starting already at 300 mV [28]. Fig. 1.6 illustrates the formation of the different phases.

As mentioned above, a large volume change of the silicon matrix accompanies the lithiation process, followed by the mechanical degradation through cracks [18, 30, 31]. These findings were supported by Ma *et al.*, who calculated upper limits for the size of different morphologies at a given lithiation degree to avoid the fracturization [32]. The relationship between the volume expansion and the lithiation was quantified by Jerliu *et al.*, using neutron reflectometry of a thin a-Si layer [33]. Chevrier *et al.* and Huang *et al.* also found expansion coefficients based on simulations [34, 35]. However, the volume expansion is not always isotropic, as shown by Liu *et al.* and Lee *et al.* [36, 37]. The reason for the fracturization is the mechanical tension arising from the volume change. Here different regions of tensile and compressive forces were found [38, 39].

The knowledge about the reason for the fracturization has led to different strategies to overcome this drawback. One strategy is the use of nanostructured materials, such as particle-based structures, nanotubes and -wires, or porous materials [18]. The particular morphology can balance the volume expansion and mechanical pressure. Therefore the fracturization is hindered. The morphology implies a high surface-to-volume ratio, which may lead to an increased capacity loss due to SEI-layer formation [40, 41].

A second method is capacity-limited cycling, as employed by Obrovac *et al.* [29]. This leads to less mechanical forces within the silicon and therefore suppresses fracturization, at the expense of lithium storage capacity.

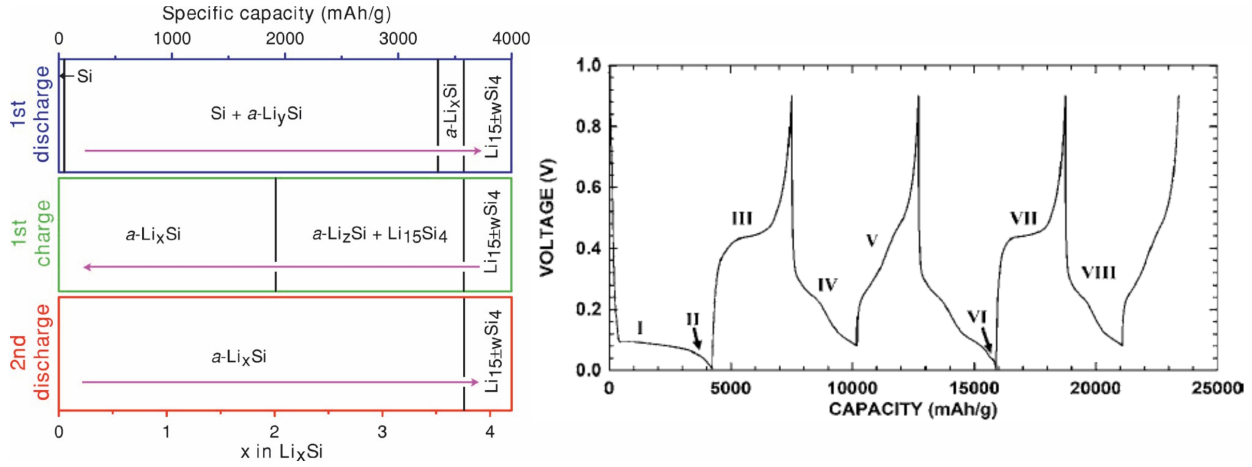

Figure 1.6: Left: Formation of different phases during first lithiation of crystalline silicon and the subsequent delithiation and lithiation. First amorphous Li_ySi and Si coexist since the silicon needs to be transformed into the amorphous state before lithiation. In the final state of the lithiation, crystalline $Li_{15}Si_4$ is formed if the voltage is sufficiently low. During delithiation, the highly lithiated $Li_{15}Si_4$ phase is diluted first, forming phases with lower lithium content. Afterward, the lowly-lithiated phase is dissolved, leaving amorphous silicon. In the subsequent lithiation, no amorphization occurs, the lithiation of silicon can start directly. x, y, and z represent a varying ratio between Li and Si. Reproduced with permission from [28], Copyright IOP Publishing Ltd. The corresponding voltage curve is shown on the right part. Clear differences between the first and second lithiation can be found, arising from the amorphization process. Taken from [29]. Copyright IOP publishing Ltd.

Surface coatings were also used to suppress the cracking of silicon electrodes [42–44]. Here a rigid layer on the silicon shall mitigate the mechanical forces arising from the lithiation and suppress the fracturization process [45]. The use of additives to the electrolyte (e.g., fluoroethylene carbonate) tackle this issue since these additives form a polymeric coating on the electrode surface [46, 47]. This approach is also used to suppress the continuous growth of the SEI-layer. The protective layer shall prevent direct contact between the silicon and the electrolyte, and therefore, no decomposition of the electrolyte takes place. The coating has to fulfil several requirements therefore, such as high ionic conductivity and mechanical robustness [9].

A variety of experimental techniques were employed to analyze the lithiation process. For most of these techniques, three different modes of operation are possible: ***ex-situ***, ***in-situ*** and ***operando***.

Ex-situ: The terminus *ex-situ* means 'outside of the original place'. Here a sample is removed from the whole system and characterized individually. An example is the characterization of the electrodes after disassembling the cell using microscopy techniques [48]. In this way, a specific part can be investigated very precisely. On the other hand, the disassembling of the cell and the sample preparation (*e.g.*, cleaning or transfer into the microscope device) may change the system. Therefore, the interpretation of the results has to be done with special care.

In-situ: The terminus *in-situ* means 'in place'. The sample is characterized within the whole system. The cell is not disassembled, but the cell operation is stopped. An example is a reflectometry

measurement taken while the sample remains unchanged. An example is a Li-Si cell, which remains in the open-circuit-voltage mode during measurement [43, 49]. This allows us to characterize a system in a given state, *e.g.*, showing the existence of layers on the electrode. Compared to *ex-situ* studies, this is technically more challenging since the cell is not disassembled and the characterization has to be done through the encasing. The absorption of the cell housing decreases the signal and may also introduce additional signals, which should be taken into account and, if possible, be removed before the data analysis. The cell operation stops, and no dynamic processes can be studied.

Operando: The terminus *operando* means 'working'. Here the whole system is characterized under working conditions, which is the difference to *in-situ* studies. For these studies, the cell is not disassembled, and also the cell operation continues. This implies that the data acquisition time has to be much smaller than the typical timescale of the sample operation. Otherwise, the acquired data cannot be related to a specific operational state. An example is a reflectometry measurement taken from an electrochemical cell during cycling [50, 51]. Here the acquisition time of a measurement is in the order of minutes, whereas the timescale of a cell cycle is several hours. In this way, the individual processes during cycling can be probed, *e.g.*, the growth of the lithiated zone within the silicon.

Operando studies are even more technically challenging than *in-situ* experiments since the measurements need to be fast (compared to the cell operation). Usually, a unique cell design is needed to improve the signal-to-noise ratio, *e.g.*, by inserting a X-ray transparent window. Of course, special care has to be taken to sustain the system's proper behavior also in the *operando* setup. Otherwise, artifacts caused by an insufficient cell design may lead to wrong interpretations of the results. An example would be the incorporation of humidity from the ambient air, which may change the processes within the sample.

From these three, *operando*-techniques are best-suited to elucidate the aging-related processes in a battery. For *ex-situ* studies, the cell needs to be disassembled, which may destroy the electrode's integrity and may change the solid-electrolyte-interface (SEI)-layer. *In-situ* studies only reveal information from a steady-state since the cell operation stops. Therefore, cycle-dependent aging could be observed, such as the fracturization of the silicon electrode after several cycles. However, only *operando* studies can resolve the cracking process and therefore give insights into the kinetics of the system. *In-situ* and *operando* analysis are the method of choice to understand the aging-related processes in batteries more in detail [52].

1.2 Objective and Scope

This thesis elucidates two aging-processes in the Li-Si-system, namely the fracturization caused by the volume expansion and the growth of the SEI-layer. Two *operando*-analysis techniques (neutron reflectometry and X-ray phase-contrast imaging) are employed to gain insights into the time-dependency of the associated processes. (100)-crystalline silicon wafers are used as electrodes since this is a well-defined model system with simple morphology and allows us to study the lithiation

without the influence of binders and conductive agents.

Chapter 2 contains a short introduction to the most relevant **electrochemical subjects**. The experimental techniques **electrochemical impedance spectroscopy (EIS)**, **reflectometry**, and **X-ray phase-contrast-imaging** will be introduced together with a description of the neutron and X-ray instruments used. The custom-made data analysis algorithms are described since *operando*-techniques benefit largely from automatized data evaluation.

Chapter 3, 4, and 5 are dedicated to the three research projects processed during this doctoral thesis:

Chapter 3 deals with the morphological changes on the microscale. A crystalline silicon wafer was lithiated galvanostatically, while *operando* neutron reflectometry measurements were performed. The growth and shrinkage of the lithium-rich layer within the silicon electrode and the SEI-layer on top of the silicon was studied. The resulting morphology changes were related to the cell voltage. Different processes related to the SEI-layer cause a charge loss during cell operation. Furthermore, *in-situ* EIS reveals insights into the electric properties. Parts of this chapter were also published [53].

Chapter 4 deals with the cracking of the silicon electrode. Macroscopic morphology changes during the (de-)lithiation process were studied. Again, a crystalline silicon wafer was lithiated. A voltage-controlled cell operation promoted the formation of different Li-Si equilibrium phases. *Operando* phase-contrast imaging was employed since this technique is highly sensitive to material interfaces. Here the cyclewise growth of a checkerboard-like fracturization pattern was observed and the voltage-dependency of the fracturization was studied. *In-situ* impedance spectroscopy and *ex-situ* focussed ion beam/scanning electron microscopy were used as complementary measurements. Parts of this chapter were also published [54].

In **chapter 5**, the influence of an artificial coating (namely aluminum oxide) on the lithiation process is discussed. As described previously, protective layers are one possible way to suppress the aging of silicon electrodes. Therefore, the lithiation of crystalline silicon coated with a thin layer of aluminum oxide was studied. Again, *operando* neutron reflectometry was employed to probe the lithiation on the nanoscale due to its high sensitivity to thin layers. The artificial coating prevents the formation of a charge-blocking SEI-layer successfully in the first cycles, but degraded later on, leading to parasitic side reactions.

The conclusions of all these three research projects is discussed in **chapter 6**.

Chapter 2

Experimental methods and theoretical background

2.1 Electrochemical concepts

Electrochemistry is a part of physical chemistry and deals with the interplay of chemical and electrical processes. The change of an electrical potential enables or disables processes. An example is the decomposition of water during electrolysis or the electroplating of zinc as resistance to corrosion. Also, batteries are electrochemical systems. Interfaces are of high importance for electrochemistry since charge transfer processes take place there. Electrochemical processes can be either exergonic or endergonic, depending on the change of the Gibbs free energy. Electrochemistry is of high importance nowadays since it is the basis for electrochemical energy storage (batteries), the electrolysis of water, fuel cells, and many more.

2.1.1 Faraday's law of electrolysis

Faraday's law connects the charge flow and material conversion within an electrochemical system. It describes the relationship between the conversion of material and the amount of charge involved in this conversion. An example is the plating of metal on one of the electrodes in an electrochemical cell. The law was first described in 1833 [55]:

$$Q = n_{\mathrm{mol}} \cdot z_{\mathrm{e}} \cdot F \tag{2.1}$$

Here, Q denotes the amount of charge, n is the molar amount of material, and z is the charge number of the ions involved in the electrochemical process. F is the Faraday-constant, which is equal to the amount of charge needed to plate one mol of ions with the charge number of one. Therefore, the constant is determined as [56]:

$$F = 96485.3365 \text{ C/mol}.$$

2.1.2 Nernst-equation

The electrode potential in a half cell depends on the electrode's standard potential and on the activity of the ions involved in the redox-reaction. The equation, which describes this relation, is called Nernst-equation, which will be introduced now, based on chapter 3 in [55]. The chemical potential μ_i of a material i can be calculated from the chemical potential under standard conditions μ_i^0 and the chemical activity α_i:

$$\mu_i = \mu_i^0 + R_{\text{gas}} T \cdot \ln(\alpha_i) \tag{2.2}$$

R_{gas} denotes the universal gas constant, which has a value of 8.3144621 J/(mol · K) [56]. T denotes the temperature.

A phase boundary exists since a two-phase system is assumed. Here charge transfer processes take place. The energy W_{el} needed to transfer one mol of z_e-times charged ions through a phase boundary is:

$$W_{el} = -z_{\text{e}} \cdot F \cdot \Delta\Phi = -z_{\text{e}} \cdot F \cdot (\Phi_{Ox} - \Phi_{Red}) \tag{2.3}$$

Here, Φ_{Ox} and Φ_{Red} denote the electrical potential of the oxidized and reduced species, respectively. Consequently, $\Delta\Phi$ is the potential difference across the phase boundary, which is the sum of the Galvani-potential and the Volta-potential. The former one denotes the difference of the electrical potential in the bulk material, whereas the latter one denotes the potential difference arising from excess charges. The electrochemical potential of a material $\mu_{EC,i}$ is therefore given by:

$$\mu_{EC,i} = \mu_i^0 + R_{\text{gas}} T \cdot \ln(\alpha_i) - z_{\text{e}} \cdot F \cdot \Phi_i \tag{2.4}$$

By assuming an equilibrium between the oxidized and reduces species:

$$\mu_{EC,ox} = \mu_{EC,red} \tag{2.5}$$

$$\mu_{Ox}^0 + R_{\text{gas}} \cdot T \cdot \ln(\alpha_{Ox}) - z_{\text{e}} \cdot F \cdot \Phi_{Ox} = \mu_{Red}^0 + R_{\text{gas}} \cdot T \cdot \ln(\alpha_{Red}) - z_{\text{e}} \cdot F \cdot \Phi_{Red} \tag{2.6}$$

$$\Rightarrow \Delta\Phi = \Phi_{Ox} - \Phi_{Red} \tag{2.7}$$

$$\Delta\Phi = \frac{\mu_{Ox}^0 - \mu_{Red}^0}{z_{\text{e}} \cdot F} + \frac{R_{\text{gas}} \cdot T}{z_{\text{e}} \cdot F} \cdot \ln\left(\frac{\alpha_{Ox}}{\alpha_{Red}}\right) \tag{2.8}$$

The first part of equation 2.8 is the so-called standard electrode potential E^0, given as difference to the standard hydrogen electrode. Therefore, also $\Delta\Phi$ will be related to the standard hydrogen electrode and is denoted as E. This gives the Nernst-equation:

$$E = E^0 + \frac{R_{\text{gas}} \cdot T}{z_{\text{e}} \cdot F} \cdot \ln\left(\frac{\alpha_{Ox}}{\alpha_{Red}}\right) \tag{2.9}$$

The electrochemical voltage series summarizes the standard potential E^0 of several redox reactions [56].

2.2 Electrochemical impedance spectroscopy

The impedance spectroscopy is a commonly used technique for the characterization of batteries [57]. A broad introduction into the fundamentals and capabilities is given in [58]. The cell voltage U is periodically changed and is frequency-dependent $U(\omega)$. This allows us to determine the frequency-dependent impedance $Z(\omega)$ of a specimen, *e.g.*, a battery. A small perturbation signal U_{pert} is superimposed with a given equilibrium potential U_{eq}:

$$U(\omega) = U_{\text{eq}} + U_{\text{pert}} \sin(\omega t) \tag{2.10}$$

Here the angular frequency ω is used, which is the frequency multiplied by 2 π. A linear relationship between perturbation and answer is assumed since the perturbation signal shall be small. This leads to a perturbation current I_{pert} as described by Ohm's law:

$$U_{\text{pert}} = Z(\omega) I_{\text{pert}} \tag{2.11}$$

$$U_{\text{pert}} \sin(\omega t) = Z(\omega) I_{\text{pert}} \sin(\omega t + \phi) \tag{2.12}$$

While varying the frequency ω, the impedance $Z(\omega)$ can be calculated from the measured current. Also a sinusoidal variation of a direct current is possible, leading to an alternating voltage. The coefficient ϕ describes the phase shift between the current I_{pert} and the voltage U_{pert} and is also frequency-dependent. For non-zero values of the phase shift, the impedance contains a real and an imaginary part. The impedance data can be evaluated using an equivalent circuit with different elements or the distribution of relaxation times. Both methods will be discussed below.

2.2.1 Electrical equivalent circuit model

One possibility to analyze impedance spectra is the method of equivalent circuits. Several electrical elements are combined in series or parallel to model the spqcimen's electrical behavior within the observed frequency range. Figure 2.1 shows an example of an equivalent circuit together with the frequency-dependent impedance. The overall impedance can be calculated using eq 2.13 and 2.14 for linear and parallel circuits, respectively.

$$Z_{\text{series}} = \sum_{i=0} Z_i \tag{2.13}$$

$$Z_{\text{parallel}} = \frac{\prod_{i=0} Z_{\text{i}}}{\sum_{i=0} \prod_{j \neq i} Z_j} \tag{2.14}$$

One of the basic elements for an equivalent circuit is the ideal resistor, also called Ohmic resistor. The behavior follows Ohm's law, also for alternating current of arbitrary frequency. Therefore the phase angle is zero. An example in an electrochemical cell is the solution resistance R_{sol}.

$$Z_{\text{resistor}}(\omega) = R \tag{2.15}$$

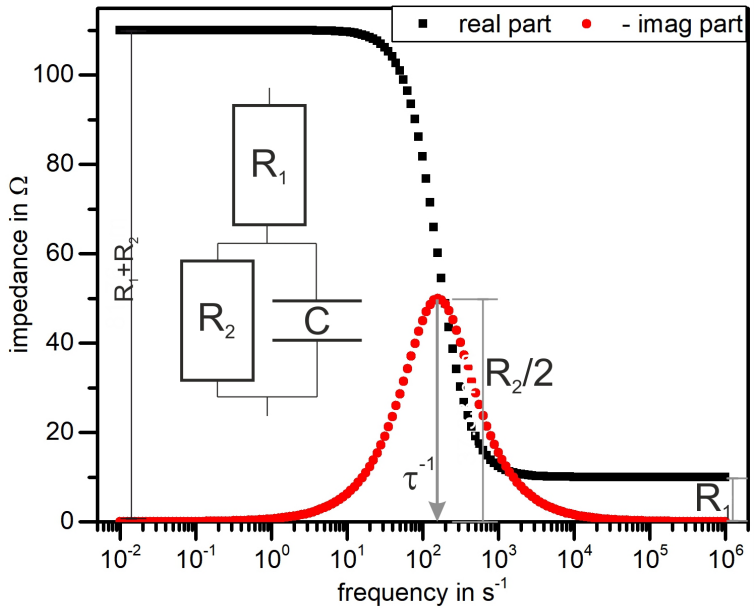

Figure 2.1: Simulated impedance spectra and the associated equivalent circuit. The circuit consists of a resistor R_1 in series with an R-C-element (capacitor C and resistor R_2 in parallel). From the impedance plot, the values for R_1 and R_2 can be extracted as well as the relaxation time $\tau = R_2 \cdot C$

The solution resistance does not depend on the frequency. It can be directly obtained from the offset of the real part of the impedance at high frequencies. This refers to R_1 in fig. 2.1 and equals 10 Ω. Another standard element is the electromagnetic coil with the inductance L. Usually, it does not describe processes inside the electrochemical cell but models the inductive behavior of the wires which are used for the measurement. The induced voltage in a coil is proportional to the time derivative of the current:

$$U = L \cdot \frac{\mathrm{d}I}{\mathrm{d}t} \tag{2.16}$$

Now we assume a sinusodial current:

$$I = I_0 \sin(\omega t) \tag{2.17}$$

Therefore, the voltage is given by:

$$U = L I_0 \omega \cos(\omega t) \tag{2.18}$$

The impedance is the quotient of the amplitude of the voltage $\overline{U}$ and the amplitude of the current $\overline{I}$:

$$Z(\omega) = \frac{\overline{U}}{\overline{I}} = L\omega \tag{2.19}$$

A phase angle of $\pi/2$ needs to be added since the phase shift between sine and cosine is $\pi/2$. Therefore, the complex impedance is given by:

$$Z(\omega) = \exp\left(i \cdot \frac{\pi}{2}\right) L\omega = i\omega L \tag{2.20}$$

Typical inductance values are in the order of 10^{-7} Ωs or lower. Therefore, the inductance is only significant at high frequencies.

Capacitors are also widely used in equivalent circuits. They can store electrostatic energy within an electrical field. If a voltage is applied to a capacitor, a specific charge Q is stored within the capacitor. During this process, the current drops exponentially. Therefore, a capacitor blocks the electrical current in the limit of low frequencies of the alternating voltage. An example is an insulating layer on an electrode or the electrical double layer.
The voltage of a capacitor is given by:

$$U = \frac{1}{C} \cdot \int_0^\infty I \cdot \mathrm{d}t = -\frac{1}{\omega C} \cdot \cos(\omega t) \tag{2.21}$$

Here, C denotes the capacitance value of the capacitor. Again, a sinusoidal current is assumed. The phase shift is $-\pi/2$. The impedance is given by:

$$Z_{\mathrm{capacitor}}(\omega) = \frac{\overline{U}}{\overline{I}} = \frac{-i}{\omega C} \tag{2.22}$$

Closely related to the capacitor is the Constant Phase Element (CPE). It models the behavior of an imperfect capacitor (*e.g.*, with a leakage current or a pseudocapacitance). An example of a CPE is a coating layer on an electrode with high resistance or pinholes for ion transport.

$$Z_{\mathrm{CPE}}(\omega) = \frac{1}{Q_0 \omega^\psi} \exp\left(-\frac{i\pi}{2}\psi\right) \tag{2.23}$$

The unit of Q_0 is s^ψ/Ω and depends on the exponent ψ. For ψ =0, the CPE acts as a resistor with a resistance $R = \frac{1}{Q_0}$. The CPE behaves like an ideal capacitor with the capacitance value Q_0 for ψ =1.
The Warburg-Element with the Warburg-constant $\mathrm{A_w}$ is a special case of the CPE with $\psi = 0.5$. It describes an impedance caused by a diffusion of ions from or to the electrode. This may occur at very high currents or low diffusion rates.

$$Z_{\mathrm{Warburg}}(\omega) = \frac{A_{\mathrm{W}}(1-i)}{\sqrt{\omega}} \tag{2.24}$$

Of course, also combinations of these elements are used. A combination of capacitor and resistor in parallel (R-C-unit) is of particular interest since it models a charge transfer process. The product of the resistance value R and the capacitance value C equals to the time constant τ of the relaxation [58]:

$$Z_{\mathrm{RC}}(\omega) = \frac{1}{\frac{1}{R} + i\omega C} = \frac{R}{1 + i\omega\tau} (\tau = RC) \tag{2.25}$$

The capacitor can be replaced by a CPE, leading to a broadening of the relaxation. According to Lasia [58], the dispersion of such an element is given by :

$$\frac{Z(\omega) - Z_\infty}{Z_0 - Z_\infty} = \int_0^\infty \frac{\tau G(\tau)}{1 + i\omega\tau} \mathrm{d}\ln(\tau) \tag{2.26}$$

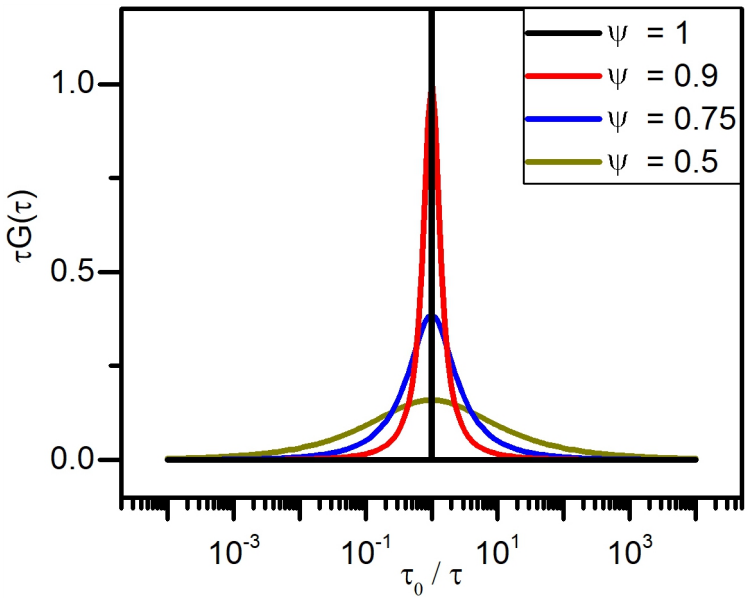

Figure 2.2: Time constant distribution function and their dependency on the exponent α. For low values of α, the distribution around the relaxation time τ_0 gets broader. For ψ =1, Dirac's delta function can be found. Adapted from [58] with permission from SpringerBooks.

Z_0 and Z_∞ denote the impedance values for a frequency of zero and infinity, respectively. $G(\tau)$ denotes the time constant distribution function. For a CPE, this is given by [58]:

$$G(\tau) = \frac{1}{2\pi\tau} \frac{\sin((1-\psi)\pi)}{\cosh(\psi \ln(\tau/\tau_0)) - \cos((1-\psi)\pi)} \tag{2.27}$$

Again, ψ denotes the exponent of the CPE (eq. 2.23). For $\psi = 1$, $G(\tau)$ simplifies to Dirac's delta function $\delta(\tau_0)$ and models the usage of simple R-C-units. For $\psi < 1$, the distribution broadens around τ_0 (Fig. 2.2).

2.2.2 Distribution of relaxation times

Another approach to analyze impedance spectra is the distribution of relaxation times. Here a sum of RC-units is used to fit the obtained impedance spectra and gain insights into the system's dynamics, but also different approaches are reported in the literature [58–61]. For experimental data, the relaxation time distribution function $\gamma(\tau)$ is approximated by a sum of R-C-units. As mentioned in eq. 2.25, each RC-unit has a specific time constant τ. This time constants can be distributed now within the inverse of the frequency range. Thereafter, the resistance value of each individual RC-unit is determined. In this way, charge transfer processes through an interface can be modeled.

$$Z_{\mathrm{DRT}} = \int_0^\infty \frac{\tau\gamma(\tau)}{1+i\omega\tau} \mathrm{d}\ln(\tau) = \sum_j^n \frac{R_j}{1+i\omega\tau_j} \tag{2.28}$$

The obtained charge transfer resistances serve as grid points for the distribution of relaxation times at the corresponding relaxation time τ.

2.2.3 Correction of time drift in impedance data - the Z-HiT algorithm

The measurement of an impedance spectrum is not instantaneous since a range of frequencies is probed. Depending on the exact measurement conditions, this may take up to several minutes. As an example: An impedance spectra on a Li-Si-coin cell, 1 MHz to 0.1 Hz, 15 pts/decade, 'low-noise mode', took on a GAMRY interface 1000 roughly 10 minutes. Within this time, different processes may change the sample, *e.g.*, wetting processes or the formation of surface layers and ion diffusion. This leads to a drift in the impedance spectra and, therefore, to artifacts in the data.
A common way to validate the obtained impedance data is the Kramers-Kronig-relation [58]. Unfortunately, the Kramers-Kronig relations require experimental data in the frequency range from zero to infinity, which is impossible to achieve due to experimental limitations. This problem can be solved using the ZHiT-correction (german: Zweipol-Hilbert-Transformation) [62], which is based on the Kramers-Kronig-relations. It assumes that the system acts as a two-pole, meaning there is no delay between excitation and response of the system.

$$\ln|Z(\omega)| \approx \ln|Z(0)| + \frac{2}{\pi}\int_{\omega_s}^{\omega_0} \phi(\omega)\,\mathrm{d}\ln(\omega) + \frac{\pi}{6}\frac{\mathrm{d}\phi(\omega_0)}{\mathrm{d}\ln(\omega)} \tag{2.29}$$

Equation 2.29 is used for the correction. Here, the modulus of the impedance is calculated from the phase, but also the inverse way is possible. ω_0 denotes the frequency, which is corrected. ω_s is the starting point of the integration, which can be chosen arbitrarily. The need of the correction is shown in fig. 2.3. The equivalent circuit shown on the upper part of the image was used to simulate

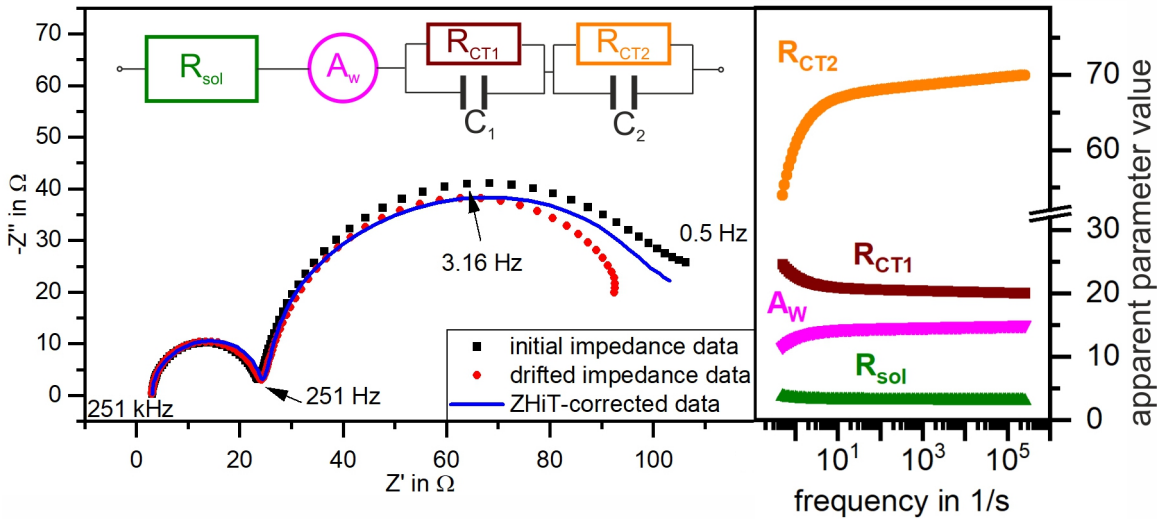

Figure 2.3: On the left: Nyquist-plot of a simulated impedance spectrum with a constant drift. The equivalent circuit employed for the simulation is shown in the upper part. The black symbols denote the initial impedance values, whereas the red symbols denote the measured ones. Especially at low frequencies, differences can be found since the measurement takes longer at low frequencies. The blue line denotes the ZHiT-corrected values, which are closer to the initial impedance values. Several frequencies are indicated in the plot. The time-dependent shift of the parameters is shown on the right as a function of the measurement frequency.

an impedance spectrum (black dots in the left part). The red dots denote the impedance spectrum, which would be measured. Here a drift of the system during the measurement is included. The corresponding parameter drift is shown in the right part of the image. At lower frequencies more time is needed to acquire the data, so a constant drift causes a larger parameter change. The blue line shows the impedance spectrum corrected by the ZHiT-algorithm. A custom-made python script that performs the ZHiT-correction is electronically available. Also, a Mathematica-script developed by Dr. Sebastian Risse can be found in the additional folder. The source code of the simulation showing the need of the ZHiT-correction can be found in the folder, too.

2.3 Reflectometry

Reflectometry is a powerful technique to study the surface of a sample or buried interfaces within the sample. The length scales for layers probed with reflectometry depend on the available instrumental resolution and range from the sub-nanometer regime to several hundred nanometers. The technique was introduced by Lyman G. Parrat in 1954 [63] and uses the angle/wavelength-dependent reflectivity of a sample to gain information about the surface-near structure and composition. An introduction to this technique is given by Daillant *et al.* [64]. For the derivation below, chapter 3 of [64] was used.

In this work, mostly neutrons are used for reflectivity measurements due to some distinct advantages. The energy of neutrons used for structure analysis is in the order of several meV, corresponding to a wavelength in the order of nanometers and therefore matching typical interatomic distances. Neutrons penetrate deeper into matter than X-rays since they interact with the nucleus, whereas X-rays interact with the electron shell. Therefore, neutrons can be used to analyze buried interfaces within a sample. Contrary to X-rays, neutrons are highly sensitive to different isotopes. The substitution of different isotopes within the sample can be used to highlight different parts. A very important example of this is the substitution of the hydrogen isotopes ^{1}H and ^{2}H.

The reflection of neutrons on the sample surface can be handled as an elastic scattering process. Therefore, the modulus of the incident and reflected wave vector are equal. The momentum transfer $\vec{q}_z$ perpendicular to the sample surface is used as the independent variable. This allows us to compare the results of experiments using a different wavelength of the incoming radiation. For specular reflectivity $\vec{q}_z$ can be calculated as:

$$q_z = |\vec{k}_{out} - \vec{k}_{in}| = \frac{4\pi}{\lambda} \sin\theta \tag{2.30}$$

Here, λ denotes the wavelength of the incident wave, θ is the incident angle. Only specular reflections will be discussed here, which means the reflected angle is equal to the incident angle.

The reflectivity of materials is linked to differences in the refractive index, as described by the Fresnel formulas [65]. For neutrons and X-rays, the refractive index n of materials differs only slightly from unity. Only a small difference can be found. This difference is called scattering length density (SLD) and is a complex number. Therefore, the refractive index for X-rays and neutrons

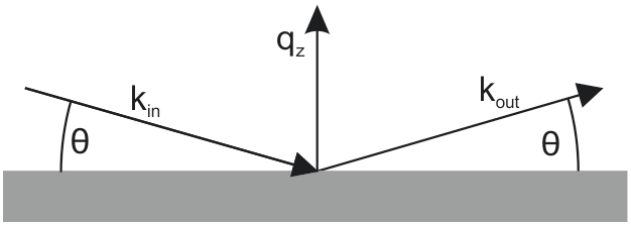

Figure 2.4: The elastic scattering on the surface. The modulus of the incident wave vector is equal to the modulus of the reflected wave vector. The difference between both is the momentum transfer, which is perpendicular to the sample surface

can be written as:

$$\begin{aligned} n &= 1 - \frac{\lambda^2}{2\pi} SLD - i\frac{\lambda}{4\pi}\kappa \\ &= 1 - \delta - i\beta \end{aligned} \tag{2.31}$$

SLD denotes the coherent part δ of the refractive index n in eq. 2.31. The SLD of each compound can be calculated by multiplying the scattering length b with the number of scatterers per volume N, *e.g.*, per unit cell of a crystal. The coherent scattering length b was determined for several different elements [66]. The scattering length density of compounds can be calculated by adding up the product of scattering length b_i with the corresponding number density individual species N_i:

$$SLD_{mixture} = \sum_i b_i \cdot N_i = \sum_i \frac{SLD_i \cdot V_i}{V_{total}} \tag{2.32}$$

The scattering length density is also sensitive to mass density changes of material since the number density and the mass density are directly proportional to each other.
The linear absorption coefficient κ in eq. 2.31 describes the attenuation of the beam caused by incoherent scattering and absorption. For X-rays, the absorption is usually one to two orders of magnitude lower than the SLD, whereas the absorption of neutrons is three or more orders of magnitude lower than this value. Therefore the incoherent part β is neglected.

2.3.1 Single interface

At an interface between two materials with different refractive indices n an incident wave gets deflected. Snell's law of refraction describes this phenomenon [65]:

$$n_1 \cos\theta_1 = n_2 \cos\theta_2 \tag{2.33}$$

Here, index 1 denotes the incident beam's media, whereas index 2 denotes the media of the refracted beam. n is the refractive index, θ is the angle of the incident or refracted beam to the interface. If the refractive index n_1 is greater than the refractive index n_2, total reflection can be observed. Here the angle of the refracted beam θ_2 is equal to zero. The upper limit for the incident angle θ_c can be calculated by:

$$\cos\theta_c = \frac{n_2}{n_1} \tag{2.34}$$

This can be simplified using the small-angle approximation for the cosine since both refractive indices are close to unity:

$$\theta_c^2 = 2\frac{n_1 - n_2}{n_1} \tag{2.35}$$

The critical angle θ_c can be rewritten using equation 2.31:

$$\theta_c = \sqrt{\frac{\lambda^2}{\pi}(SLD_2 - SLD_1)} \tag{2.36}$$

$$q_c = 4\sqrt{\pi(SLD_2 - SLD_1)} \tag{2.37}$$

Therefore, up to an angle θ_c, the interface reflects the whole incident beam. The Fresnel law of reflection describes the reflection coefficient ρ of the interface also at higher angles [64]:

$$\rho = \frac{n_1 \sin\theta_1 - n_2 \sin\theta_2}{n_1 \sin\theta_1 + n_2 \sin\theta_2} \tag{2.38}$$

Making use of the trigonometric identity and Snell's law of refraction(eq. 2.33), we obtain:

$$\rho = \frac{n_1 \sin\theta_1 - n_2\sqrt{1 - \cos^2(\theta_1)\left(\frac{n_1}{n_2}\right)^2}}{n_1 \sin\theta_1 + n_2\sqrt{1 - \cos^2(\theta_1)\left(\frac{n_1}{n_2}\right)^2}} \tag{2.39}$$

$$= \frac{n_1 \sin\theta_1 - \sqrt{2\,(\delta_1 - \delta_2) + \sin^2(\theta_1){n_1}^2}}{n_1 \sin\theta_1 + \sqrt{2\,(\delta_1 - \delta_2) + \sin^2(\theta_1){n_1}^2}} \tag{2.40}$$

For the last step, 2.31 was used. Quadratic terms of δ were neglected. Now the small-angle approximation is used as well as 2.35 for the critical angle:

$$\rho = \frac{n_1\theta_1 - \sqrt{2(\delta_1 - \delta_2) + {n_1}^2{\theta_1}^2}}{n_1\theta_1 + \sqrt{2(\delta_1 - \delta_2) + {n_1}^2{\theta_1}^2}} \tag{2.41}$$

Formula 2.35 is used to replace the scattering length density difference as well as the small-angle assumption:

$$\rho = \frac{n_1\theta_1 - \sqrt{n_1^2\theta_1^2 - \theta_c^2}}{n_1\theta_1 + \sqrt{n_1^2\theta_1^2 - \theta_c^2}} \tag{2.42}$$

Total reflection still occurs for $\delta_1 < \delta_2$ since the radicant may get negative otherwise for small angles. For large angles, i.e., $\theta_1 >> \theta_c$ equation 2.41 can be simplified further:

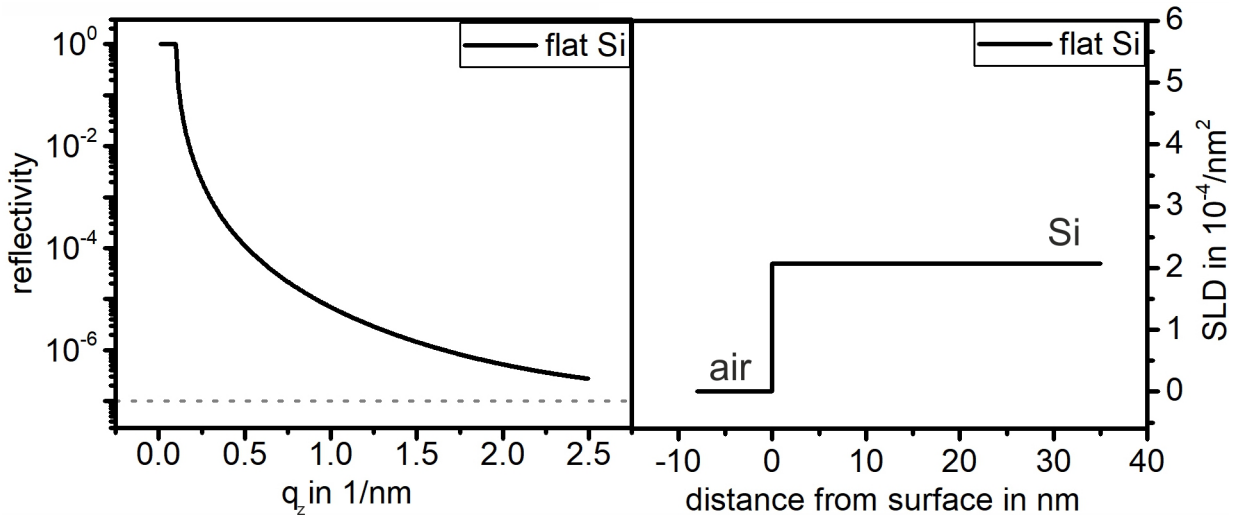

Figure 2.5: Simulated neutron reflectivity curve (left) and corresponding SLD-profile (right) of a flat silicon surface. The dashed horizontal line indicates the background noise

$$\rho = \frac{\theta_c^2}{4n_1^2\theta_1^2} \implies \mathrm{P} = |r|^2 \propto \theta_1^{-4} \tag{2.43}$$

Now eq. 2.30 and 2.36 are used to replace the angles within the equation. The result gives the q-dependent reflectivity P of a single interface, as also shown in figure 2.5:

$$\mathrm{P} = \frac{16\pi^2 \Delta SLD}{q_z^4} \tag{2.44}$$

2.3.2 Two interfaces - a single layer

The reflectivity of a single interface is the basis for the treatment of several interfaces. The simplest system with more than one interface is one well-defined layer on a substrate. Here two interfaces are present. Figure 2.6 illustrates the situation. As shown, internal reflections need to be taken into account. The reflection coefficient ρ_{total} can be written as:

$$\begin{aligned}\rho_{\mathrm{total}} = \rho_{01} & \\ &+ \tau_{01}^{\mathrm{trans}} \rho_{12} \tau_{10}^{\mathrm{trans}} \exp\left(2i\vec{k_1}\cdot\vec{d_1}\right) \\ &+ \tau_{01}^{\mathrm{trans}} \rho_{12}\rho_{10}\rho_{12} \tau_{10}^{\mathrm{trans}} \exp\left(4i\vec{k_1}\cdot\vec{d_1}\right) \\ &+ \ldots \\ &+ \tau_{01}^{\mathrm{trans}} \rho_{12} \tau_{10}^{\mathrm{trans}} \left(\rho_{10}\rho_{12}\exp\left(2i\vec{k_1}\cdot\vec{d_1}\right)\right)^h\end{aligned} \tag{2.45}$$

Here, ρ_{01} denotes the reflection coefficient of the interface between layer 0 and layer 1. A similar notation is used for the transmission coefficients τ^{trans}. A geometrical series is used since both, the reflection coefficient r and the transmission coefficient τ^{trans}, are smaller than unity:

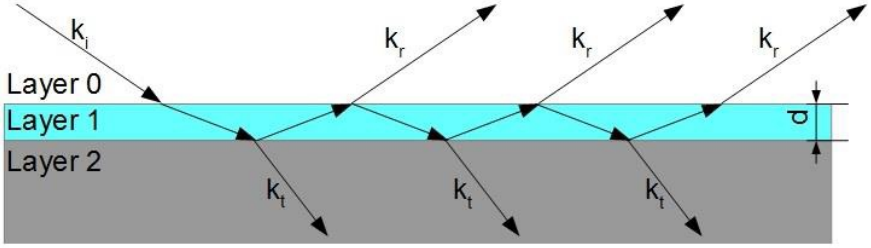

Figure 2.6: The beam path in a single layer system. On both interfaces, multiple reflections occur. The resulting reflectance shows several local minima and maxima.

$$\rho_{\text{total}} = \rho_{01} + \tau_{01}^{\text{trans}}\tau_{10}^{\text{trans}}\rho_{12}\sum_{h=0}^{\infty}\left(\rho_{01}\rho_{12}\exp\left(2i\vec{k_1}\cdot\vec{d_1}\right)\right)^h \tag{2.46}$$

The solution of a geometrical series is well-known. Therefore, eq.2.46 simplifies to:

$$\rho_{total} = \frac{\rho_{01} + \rho_{12}\exp\left(2i\vec{k_1}\cdot\vec{d_1}\right)}{1 + \rho_{01}\rho_{12}\exp\left(2i\vec{k_1}\cdot\vec{d_1}\right)} \tag{2.47}$$

Again, the square of the reflection coefficient r_{total} is the reflectivity P. The reflectivity P is given by:

$$\mathrm{P} = \frac{\rho_{01}^2 + \rho_{12}^2 + \rho_{01}\rho_{12}\cos(2k_1d_1)}{1 + \rho_{01}^2\rho_{12}^2 + 2\rho_{01}\rho_{12}\cos(2k_1d_1)} \tag{2.48}$$

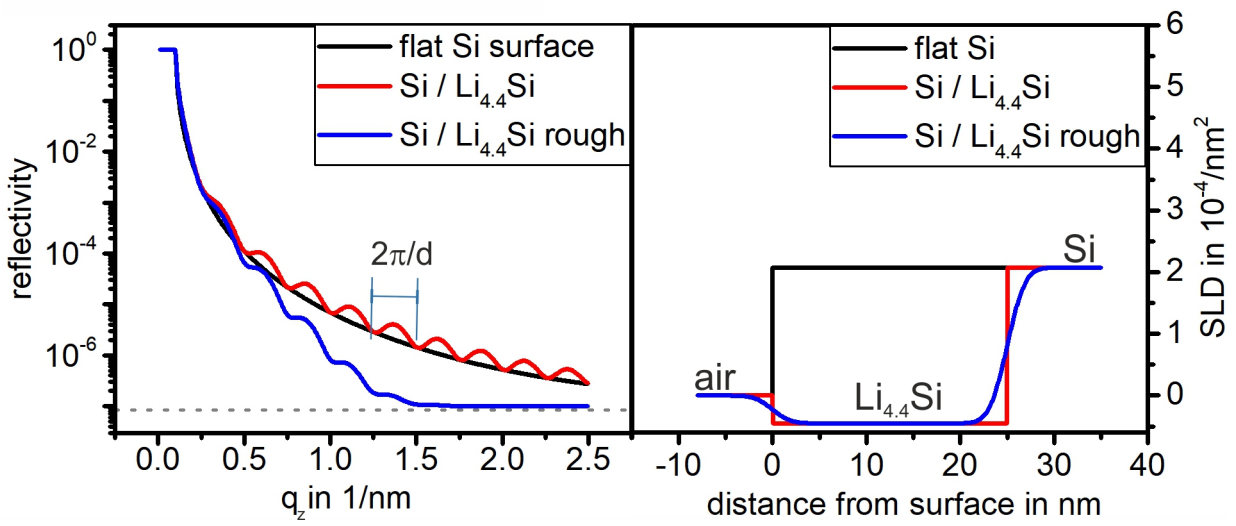

Figure 2.7: Simulated neutron reflectivity curve (left) and corresponding SLD-profile (right) of a flat silicon surface (black), a single flat lithiated layer (red), and the layer with roughness (blue). The dashed horizontal line indicates the background noise. An oscillation can be found on the reflectivity curves, which is inversely proportional to the associated layer thickness [67]

No surface is ideally flat. A certain roughness σ may be present. The refractive index near the interface changes from one bulk-value to the other, which can be modeled by several functions. Nevot and Croce suggested an error-function [68]. The reflection coefficients are modified then by an additional factor:

$$\rho_{rough} = \rho_{smooth} \exp\left(-2k_i k_t \sigma^2\right) \tag{2.49}$$

2.3.3 Multi-layer systems

The previous approach can be continued to a system with multiple layers. Each layer is handled separately then. This leads to the formula derived by Parrat in 1954 [63]:

$$\rho_{j-1,j}^{total} = \frac{\rho_{j-1,j} + \rho_{j,j+1} \exp(2ik_j d_j)}{1 + \rho_{j-1,j}\rho_{j,j+1} \exp(2ik_j d_j)} \tag{2.50}$$

Eq. 2.50 is a recursive formula. The reflectivity of the lowest layer (which is furthest away from the surface) is calculated first. Afterward the reflectivity of the layer above is calculated. The substrate is handled as a layer with an infinitive thickness. Therefore, the reflectivity of the backside of the sample is zero. $\rho_{j-1,j}^{total}$ denotes the reflection coefficient of the interface between layer *j-1* and *j*, including also multiple reflections.

An equivalent, but numerically faster approach is the use of the transfer-matrix-method introduced by Abelès [69]. An introduction can be found in [64]. For each layer, a propagation matrix is created, which describes the transmission of the incident wave through the layer. Reflection matrices describe the reflection at the interfaces. Afterward the matrices are multiplied to describe the reflection behavior of the complete sample:

$$\begin{pmatrix} H_{+,0} \\ H_{-,0} \end{pmatrix} = \underline{\mathrm{P}}_{0,1}\underline{T}_1 \ldots \underline{\mathrm{P}}_{N-1,N} \begin{pmatrix} H_{+,N} \\ H_{-,N} \end{pmatrix} = \underline{M} \begin{pmatrix} H_{+,N} \\ H_{-,N} \end{pmatrix} \tag{2.51}$$

$H_{+,j}$ and $H_{-,j}$ denote the upward and downward traveling wave in the j$^{\text{th}}$ layer, respectively. Both waves can be described by:

$$H_{\pm,j} = A_j^{\pm} \exp(\pm ik_{z,j} z) \tag{2.52}$$

Here, $k_{z,j}$ denotes the scattering vector in z-(depth)-direction in the j$^{\text{th}}$ layer. The reflection matrices $\underline{\mathrm{P}}_{j,j+1}$ can be calculated by:

$$\underline{\mathrm{P}}_{j,j+1} = \begin{pmatrix} p_{j,j+1} & m_{j,j+1} \\ m_{j,j+1} & p_{j,j+1} \end{pmatrix} p_{j,j+1} = \frac{k_{z,j} + k_{z,j+1}}{2k_{z,j+1}} n_{j,j+1} = \frac{k_{z,j} - k_{z,j+1}}{2k_{z,j+1}} \tag{2.53}$$

The transfer matrices $\underline{T}$ are calculated by:

$$\underline{T}_j = \begin{pmatrix} \exp(-ik_{z,j}d_j) & 0 \\ 0 & \exp(ik_{z,j}d_j) \end{pmatrix} \tag{2.54}$$

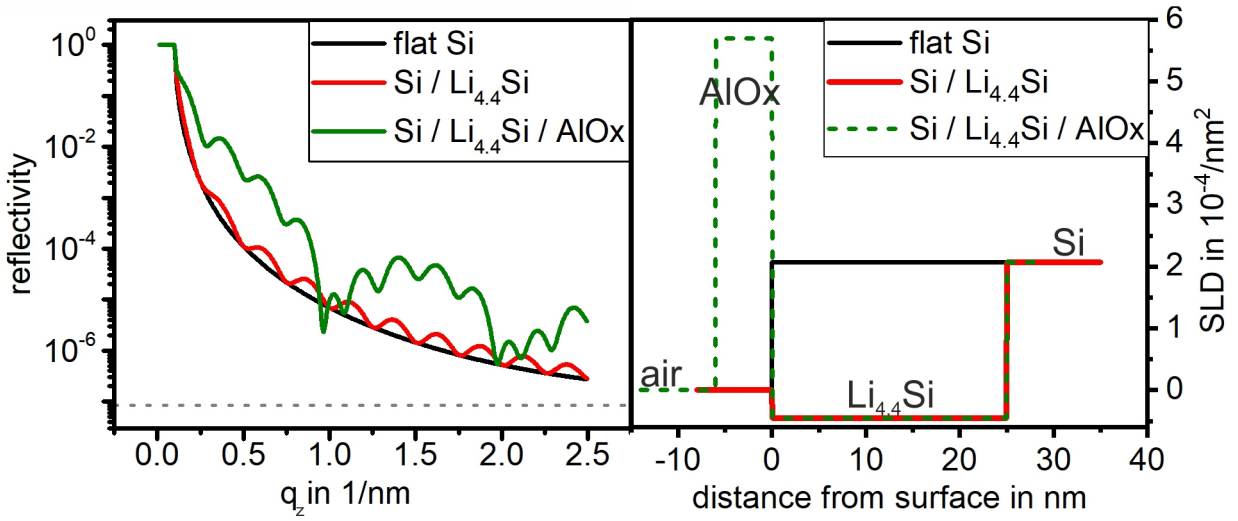

Figure 2.8: Simulated neutron reflectivity curve (left) and corresponding SLD-profile (right) of a flat silicon surface (black), a single flat lithiated layer (red), and an additional aluminum oxide layer on top (green). The dashed horizontal line indicates the background noise. A superposition of two different oscillations can be found, arising from the two layers [67].

These matrices are multiplied afterward. The resulting matrix $\underline{M}$ can be used to calculate the reflection coefficient of the whole sample:

$$r = \frac{\underline{M}_{12}}{\underline{M}_{22}} \tag{2.55}$$

Figure 2.8 shows the reflectivity of a two-layer system (6 nm aluminum oxide on a 25 nm $Li_{4.4}Si$-layer on top of a silicon substrate). The reflectivity curve shows a superposition of two oscillations (see also fig. 2.7). The number of layers increases the number of additional features in the reflectivity data. Furthermore, the occurrence of roughnesses influences the data also. Therefore, the analysis of reflectivity data can become a difficult task.

2.3.4 Neutron instruments

2.3.4.1 V6 - A neutron reflectometer at Helmholtz-Zentrum Berlin

The neutron instrument V6 was a reflectometer located at the BER II neutron reactor[70, 71]. The reactor ended operation at the end of 2019. A graphite monochromator created a beam with a wavelength of 0.466 nm ± 2 %. A beryllium filter cooled with liquid nitrogen was employed to cancel out higher frequency orders of the incident beam. Three different slits (two before and one after the sample) collimated the neutron beam. V6 operated with a vertical scattering plane, which also enabled measurements on liquid samples. For solid samples, a θ - 2θ geometry was used. The q_z-range is up to 4.68/nm for solid samples. Either a position-sensitive detector or pencil-detectors could be used to detect the incoming neutrons. The typical neutron flux was around $3 \cdot 10^4$ neutrons/cm^{2}s. A complete reflectivity pattern is acquired by changing the incident angle

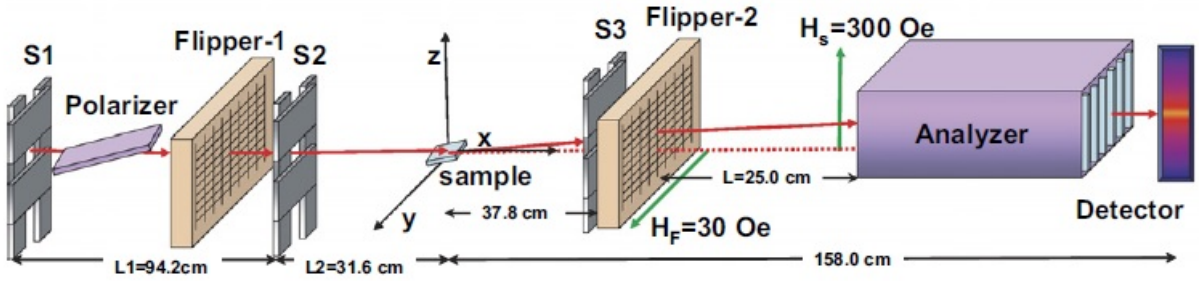

Figure 2.9: Setup of the neutron reflectometer V6 at BERII/Helmholtz-Center Berlin. No magnetic studies were done in this work, so the Flipper, Polarizer, and Analyzer were not used. Reproduced from [70] with permission from Elsevier.

stepwise. For small angles, the sample may get overilluminated, meaning the sample's projected surface is smaller than the height of the incident beam. Then a geometrical correction of the reflectivity pattern is required. A typical measurement for the systems used in this thesis took around two hours, meaning no *operando*-studies were possible on this instrument but preliminary characterizations. The beam path is shown in fig. 2.9, a sketch of the instrument is shown in fig. 2.10.

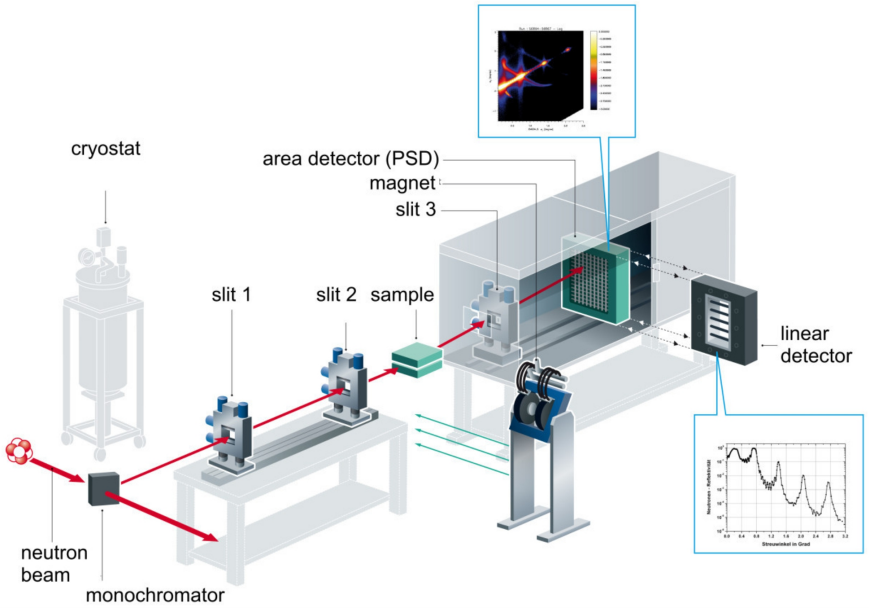

Figure 2.10: Schematic view of the Neutron reflectometer V6 at BERII/Helmholtz-Center Berlin.Neutrons are generated via a nuclear fission process. From a polychromatic beam, neutrons with a wavelength of 0.466 nm were extracted and used for structure investigations. Taken from [71] under CC BY 4.0-license.

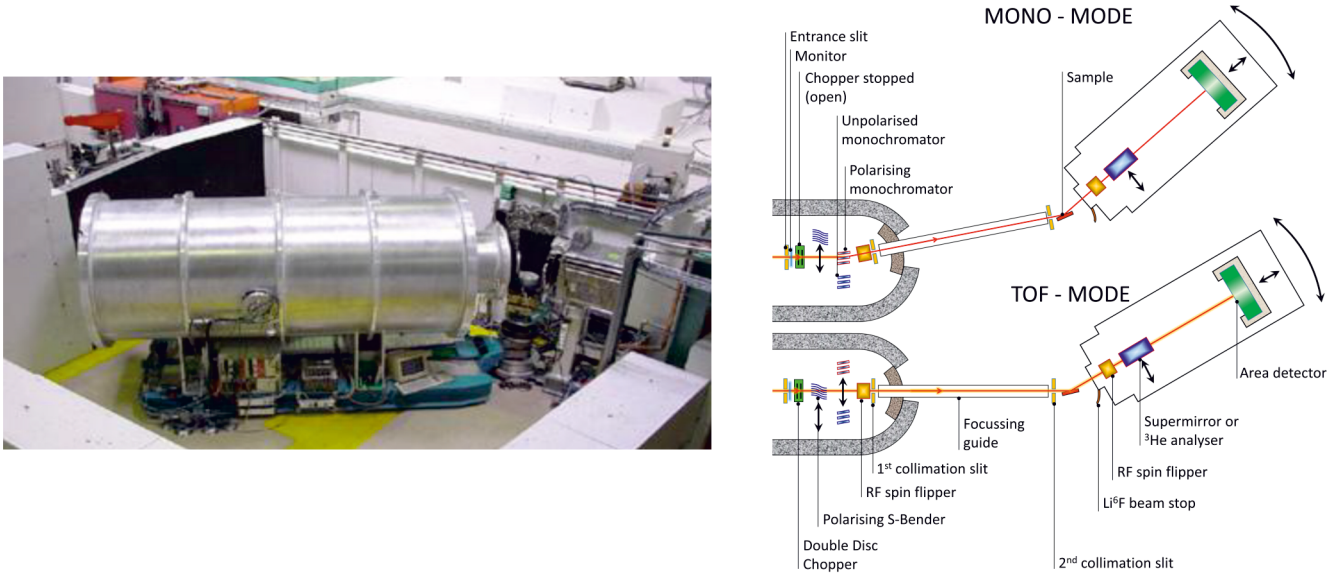

Figure 2.11: The D17 neutron reflectometer at the Institute Laue-Langevin. The left part shows a photograph of the instrument. The right part shows a sketch of the instrument. Two operation modes are possible, either a monochromatic mode or a TOF-mode [72]. A variable opening of the choppers allows to balance the experimental resolution and the neutron flux. Image taken from [73]

2.3.4.2 D17 - a neutron reflectometer at Institute Laue-Langevin

D17 is a neutron reflectometer at the Institute Laue-Langevon, Grenoble (France) [72]. It can operate in a monochromatic mode and a Time-of-flight(TOF)-mode.
The TOF-mode operates with a broad wavelength band, ranging from 0.2 to 2.7 nm. This enables the simultaneous reflectivity measurement over one order of magnitude in the momentum transfer since no change of the incident angle is necessary (eq. 2.30). Together with the high neutron flux of $9.6 \cdot 10^9$ neutrons/cm^{2}s at the sample position this enables the study of kinetic processes. For the TOF-mode, the incoming neutron beam is cut by a chopper-system, which allows us to calculate the neutron's wavelength based on its detection time. Furthermore, the chopper system defines the resolution of the wavelength and, therefore, the resolution of the momentum transfer q. A horizontal scattering plane is used at the instrument. A typical measurement time for the systems used in this thesis was roughly 5 minutes.

2.3.4.3 OFFSPEC - a neutron reflectometer at ISIS Neutron and Muon Source

OFFSPEC is one of the reflectometers at the ISIS Neutron and Muon source [74]. It is located at the target station TS2. Contrary to nuclear reactors, where neutrons are produced via fission of uranium atoms, a spallation source generates neutrons via the spallation process. Here a proton beam hits a target made of heavy elements (in the ISIS-facility a tungsten target is used). This repeats 10 times per second, which generates a neutron pulse each time. This pulse is used for TOF-reflectometry measurements at OFFSPEC. The wavelength ranges from 0.2 to 1.5 nm. The

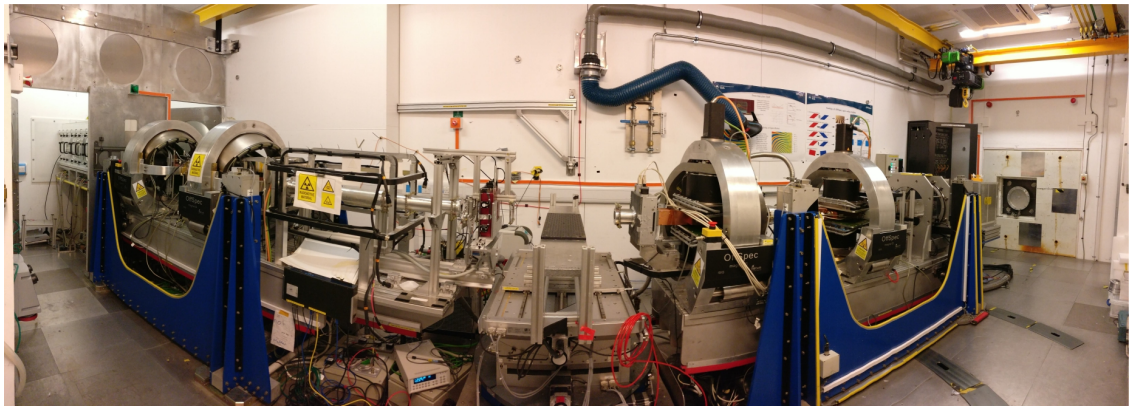

Figure 2.12: The OFFSPEC neutron reflectometer at the ISIS neutron and muon source. The photograph shows a panorama-view of the whole instrument. The neutron beam impignes from the left. Picture provided by the instrument scientist Joshaniel Cooper.

lower end of the wavelength band is cut off compared to other instruments at the same target since a bent neutron guide is used at this instrument. This reduces the instrument's background level arising from gamma-radiation and fast neutrons and enables offspecular measurements. However, this cuts off the lower end of the wavelength band, which would end at 0.09 nm otherwise. A typical measurement time for the systems used in this thesis was roughly 7 minutes.
From the three reflectometers used during this thesis, D17 was the instrument with the highest performance. Here the highest flux was available, which is also a consequence of the neutron source. The TOF-mode allows us to cover a certain q_z-range simultaneously, enabling fast scans for kinetic studies. Nevertheless, also V6 and OFFSPEC contributed with an essential part to this thesis. Table 2.1 gives an overview of the most important properties of the instruments.

instrument	V6	D17	OFFSPEC
location	HZB, Berlin	ILL, Grenoble	ISIS, Harwell
type of neutron source	Research reactor	Research Reactor	Spallation source
operation mode	monochromatic	monochromatic of TOF	TOF
data acquisition time	2 hours	5 minutes	7 minutes
wavelength in nm	0.466	0.2 to 2.7	0.2 to 1.5
q-range	up to 4.68/nm	0.02 to 20	0.06 to 3
q-resolution	2 %	0.5 to 20 %	2 to 5 %
remarks	liquid/solid samples	high flux	low noise

Table 2.1: Basic properties of the reflectometer used in this thesis.

2.4 Radiography

Radiography is a technique that creates images of samples in real space. This is contrary to scattering techniques such as reflectometry, which create images in the reciprocal space. Radiation with a high penetration depth is needed since the transmission through the specimen is employed to generate the image[76]. The first radiogram was taken by W.C. Röntgen in 1895, the discoverer of the X-rays. It shows a human hand and illustrates the difference in the absorption of X-rays by different materials.
Radiography can be subdivided into attenuation-contrast radiography and phase-contrast radiography [76]. The former one employs the imaginary part of the refractive index (the absorption), whereas the latter one uses the real part of the refractive index (the refraction)[76, 77]. A direct comparison of both techniques is illustrated in fig. 2.13, showing the highlighting effect of edges in phase-contrast imaging.
As already mentioned in eq. 2.31, the refractive index can be written as:

$$n = 1 - \frac{\lambda^2}{2\pi} SLD - i\frac{\lambda}{4\pi}\kappa = 1 - \delta - i\beta \tag{2.56}$$

The attenuation-based radiography employs the imaginary part of the refractive index to create 2D-projections of a specimen[78]. While X-rays pass through a sample, the amplitude of the corresponding wave decreases. Now we consider the incoming radiation as a plane wave:

$$A = A_0 \exp\left(i\left(\omega t - \frac{\omega}{c} x n\right)\right) \tag{2.57}$$

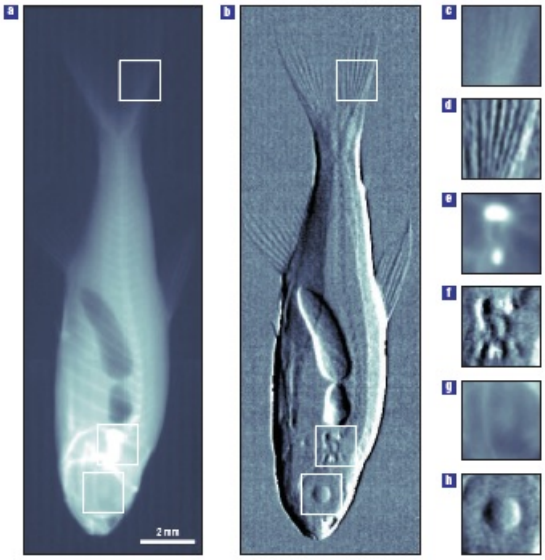

Figure 2.13: Radiograms of a fish, obtained using attenuation-contrast X-ray radiography (a) and phase-contrast X-ray radiography. The small pictures on the right (c-h) show a magnification of the spots marked with a white rectangle. Taken from [75], with permission of Springer Nature.

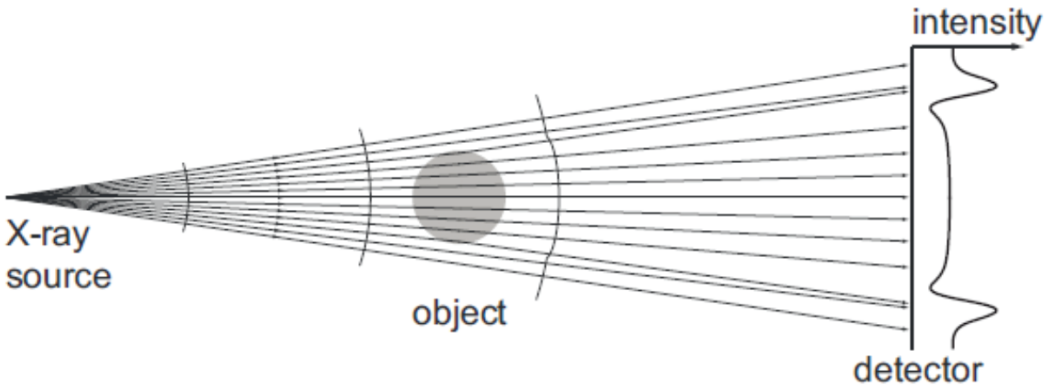

Figure 2.14: Principle of phase-contrast imaging. The incident radiation is refracted at material interfaces. This generates a dip-peak-pair in the intensity at the detector after a certain propagation distance (propagation-based phase-contrast imaging). Reprinted with permission from [80]. Copyright The Optical Society

A_0 is the amplitude of the wave, ω is the wave's angular frequency, c is the speed of light, and t and x denote the time and position, respectively. n is the complex refraction index (eq. 2.56). Now the ratio of the amplitudes before (A_f) and after (A_s) transmission through the sample shall be calculated. The time difference can be neglected. The position is the thickness d of the sample.

$$\frac{A_s}{A_f} = \exp\left(-i\frac{\omega d}{c}(1-\delta-i\beta)\right) = \exp\left(\frac{-\omega d\beta}{c}\right)\exp\left(-i\frac{\omega d}{c}(1-\delta)\right) \tag{2.58}$$

The first part describes the attenuation of the wave, whereas the second part describes the phase shift. The intensity is the square of the amplitudes [65]:

$$I = \frac{A_s}{A_f}\frac{A_s^*}{A_f^*} = \exp\left(\frac{-2\omega d\beta}{c}\right) \tag{2.59}$$

The coefficient $\kappa = \frac{4\pi\beta}{\lambda} = \frac{2\omega\beta}{c}$ is also called the linear absorption coefficient. Eq. 2.59 is also called Lambert-Beer-law [65].
The phase-contrast radiography uses the real part of the refractive index [77]. At interfaces within the specimen, refraction occurs according to Snell's law (eq. 2.33). This causes a deviation of the incident beam and leads to an increased contrast at interfaces if the distance between sample and detector is adequately adjusted (propagation-based phase-contrast imaging) [76, 77, 79]:

2.4.1 Processing of radiography data

Fig. 2.15 shows the correction procedure applied after image acquisition. The flat field correction is done to normalize the images to the incoming beam intensity, whereas the ramp correction corrects for spatial beam inhomogeneities. A Scale-invariant Feature Transform (SIFT) corrects for possible positional errors since the sample is removed from the beam for flat field image acquisition

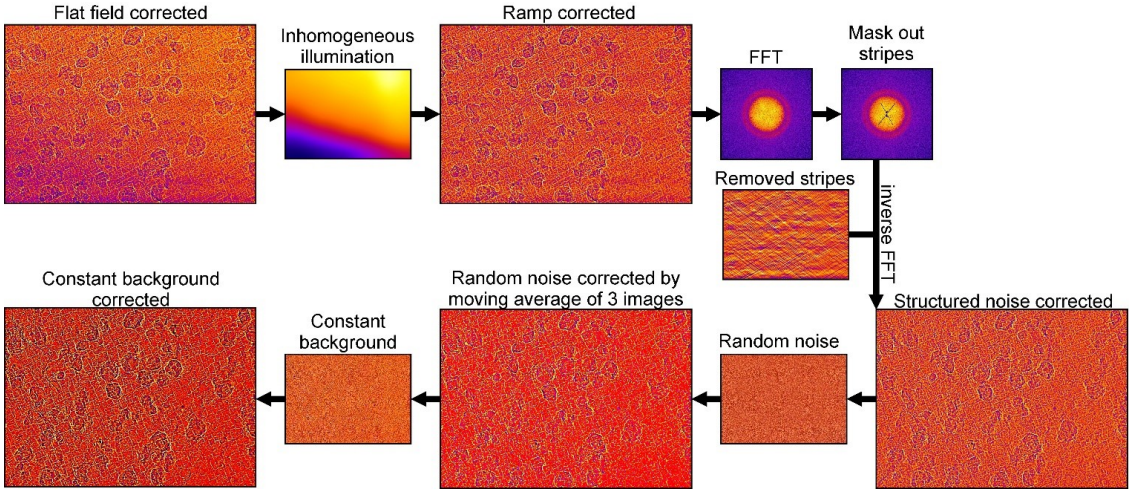

Figure 2.15: Image correction procedure applied after image aquisition. Taken from the supporting information of [54].

and inserted again afterward [81]. Horizontal stripes within the acquired images, arising from the exposure time and the movement of the monochromator mirrors, are removed by a special filter [82]. Afterward, an averaging over time or a binning of pixels can be used to reduce the noise. This procedure was used in chapter 4.

2.4.2 The BAMline-beamline

The BAMline-station is located at the BAMline-beamline at the synchrotron BESSY II and got its name from the German federal institute for materials research, the 'Bundesanstalt für Materialforschung und -prüfung' [83]. It offers different analytical techniques, such as X-ray tomography, X-ray fluorescence analysis, and X-ray diffraction [83]. A superconducting 7 T wavelength shifter generates coherent X-ray radiation from the electron packages within the synchrotron. Two different monochromators can be used depending on the desired energy resolution $\frac{E_{beam}}{\Delta E_{beam}}$, which is up to

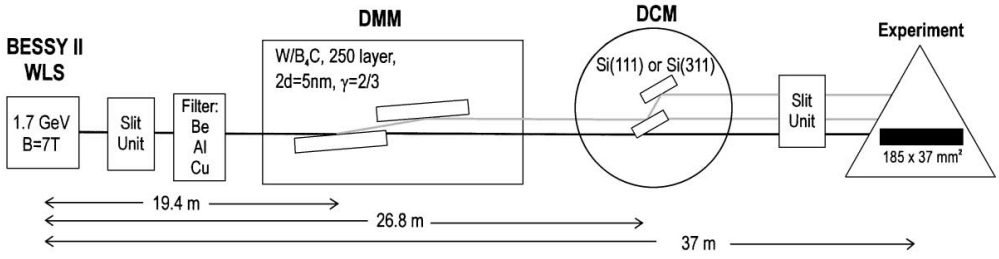

Figure 2.16: Scheme of the optical system at the BAMline station/BESSY II. The X-ray beam is generated by a 7 T wavelength shifter (WLS). Two different monochromators are available, either a double mirror monochromator (DMM) or a double crystal monochromator (DCM). Reprinted from [83] with permission from Elsevier.

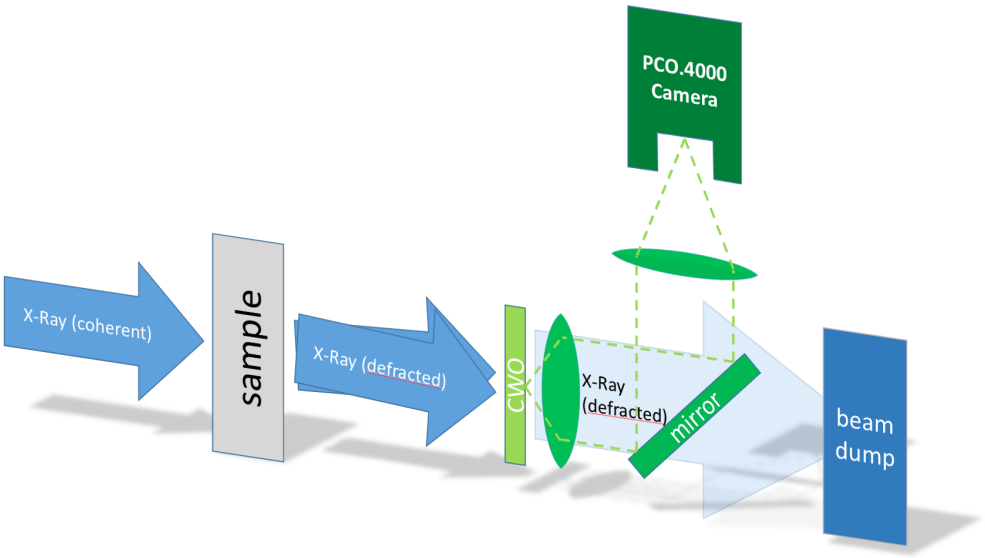

Figure 2.17: Scheme of the detector system at the BAMline station/BESSY II. The X-ray beam interacts with the sample. Afterward, the CWO-scintillator converts the transmitted radiation into visible light, which is detected by a CCD-sensor. In between a magnification system is available. Taken from the supporting information of [54].

20000. Photon energies from 5 keV up to 50 keV can be achieved in the monochromatic mode, a beam size up to 10 mm is available. The maximum flux is around 10^{12} photons per second. As detector, a 60 µm $CdWO_4$ scintillator is used together with a magnification system and a PCO.400 camera. Figure 2.17 shows an illustration of the detector setup, whereas figure 2.16 gives an overview about the optical elements before the sample position. The time needed per measurement varies depending on the specimen, but measurements within 1 minute or faster are possible. Depending on the distance between sample and detector, attenuation-based measurements or phase-contrast measurements are possible.

2.5 The electrochemical cells

An electrochemical cell provides electrical energy based on electrochemical reactions or consumes electrical energy to enable electrochemical reactions. It can be used to study electrochemical processes. An electrochemical cell consists of at least an anode (electron-accepting electrode) and a cathode (electron-donating electrode), which are in contact with each other through an ion-conducting media, the electrolyte. Additional parts, such as a reference electrode or a membrane, may be included.

In electrochemical cells either exothermic (converts chemical energy to electrical energy, *e.g.*, discharge of a battery) or endothermic reactions (converts electrical energy to chemical energy, *e.g.*, electrolysis) may take place. Figure 1.2 illustrates such a cell in a basic configuration. It contains at least two electrodes (cathode and anode) and an electrolyte. At each electrode, a half cell reaction

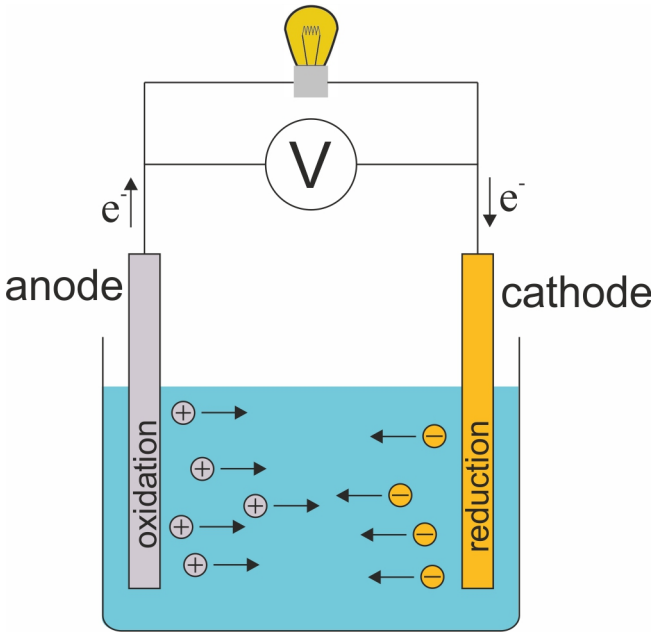

Figure 2.18: Setup of an electrochemical cell. Two electrodes, the anode and the cathode, are immersed in an electrolyte, which enables an ion flow between the electrodes. At the anode, an oxidation reaction takes place, whereas the cathode mediates reduction reactions. The ions move through the electrolyte to the other electrode, depending on their oxidation state. Electrons move through the external connection and generate the charge equilibrium. Different materials can be employed as electrode materials (see also fig. 1.3).

occurs, which sum up to the overall redox reaction. At the anode, the oxidation takes place, whereas the reduction reaction takes place at the cathode. The electrolyte serves as ion-conducting media between the electrodes. For the discharge of a LIB using a graphite electrode as anode and cobalt oxide as cathode this would refer to:

$$\mathrm{LiC_6} \longrightarrow \mathrm{Li^+ + e^- + C_6}\ (\textit{Anode}) \tag{2.60}$$

$$\mathrm{Li^+ + e^- + CoO_2} \longrightarrow \mathrm{LiCoO_2}\ (\textit{Cathode}) \tag{2.61}$$

The charge-balancing occurs through the external electrical connection. The cell voltage under open-circuit conditions (OCV) can be calculated using the Nernst-equation and depends on the standard potentials of the electrodes as well as the ion activity and the number of electrons transferred per ion (see also chapter 2.1.2). An overview of the working potential of several electrode materials vs $\mathrm{Li/Li^+}$ is given in fig. 1.3 and also by Osiak *et al.* and Larcher *et al.* [2, 84]. The amount of electrochemically active material and the storage capacity of the electrodes determine the capacity of the cell.

The same equations can be set up for a Li-Si half cell. During discharge, lithium is stripped from the metallic lithium electrode and forms an alloy with the silicon electrode. The working potential depends on the lithium concentration (fig. 1.5).

$$\mathrm{Li} \longrightarrow \mathrm{Li^+ + e^-}\ (\textit{Anode}) \tag{2.62}$$

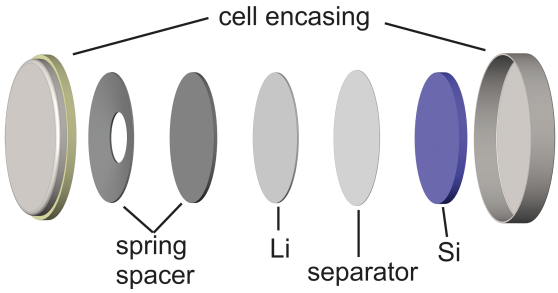

Figure 2.19: Design of the CR2032 coin cell used for laboratory tests. The cell case consists of stainless steel to protect the electrochemical system from the environment. A spring within the case creates contact pressure and ensures the electrical contact between electrodes and cell case. The separator prevents an electrical short-circuit between the two electrodes Li and Si. Approximately 250 μl of electrolyte solution is used in this cell design.

$$x\,\mathrm{Li}^{+} + x\,\mathrm{e}^{-} + \mathrm{Si} \longrightarrow \mathrm{Li}_{\mathrm{x}}\,\mathrm{Si}\ (Cathode) \tag{2.63}$$

Figure 2.19 shows a more advanced design of an electrochemical cell. This cell is similar to CR2032 coin cells commercially available and is sealed to protect the inner part of the electrochemical cell against moisture and oxygen. Furthermore, the stainless steel spring applies a mechanic pressure on the electrodes.

Despite the good electrochemical performance of the coin cell, additional cell-designs are necessary since the coin cell is not eligible for *operando*-studies. Here a 'window' is necessary that allows us to investigate the processes within the cell. Therefore, two additional cells were designed for neutron reflectometry and radiography. Figure 2.20 shows these two cells and table 2.2 summarizes the geometric parameters of the different cells.

The neutron reflectometry cell is located on the left, whereas the radiography cell is located on the right. The neutron cell on the left is the larger cell of these two. The edge length of the base plate is roughly 11 cm. The silicon wafer has a diameter of 6 cm and a height of approx. 1 cm and serves as a 'window' for the incoming neutron radiation. The reason for the size is the limited intensity of a neutron beam. Therefore, the reflecting interface has to be as large as possible. Metallic lithium foil is employed as the second electrode at the bottom with a diameter of 5 cm. A separator is placed on the lithium foil to prevent an electrical short circuit. In a later version of the cell, the separator was kept in place by an additional metal ring screwed into the current collector at the bottom. The current collector and the baseplate consist of stainless steel, similar to the steel cap. Polyether ether ketone (PEEK) is used as cell case material since it is electronically insulating and inert against the electrolyte. Furthermore, it is mechanically stable and rigid. Ethylene propylene diene monomer (EPDM) rubber rings are used as sealing on the top and at the bottom. Boron carbide plates are used as neutron absorbers to reduce the background level. The current collector at the bottom can be adjusted in height to change the cell's total volume. Approximately 5 ml of electrolyte is used to fill the cell.

The design of the radiography cell on the right is closer to the coin cell design. Here, lithium, separator and silicon are pressed together. At the back of each electrode, a stainless steel spacer

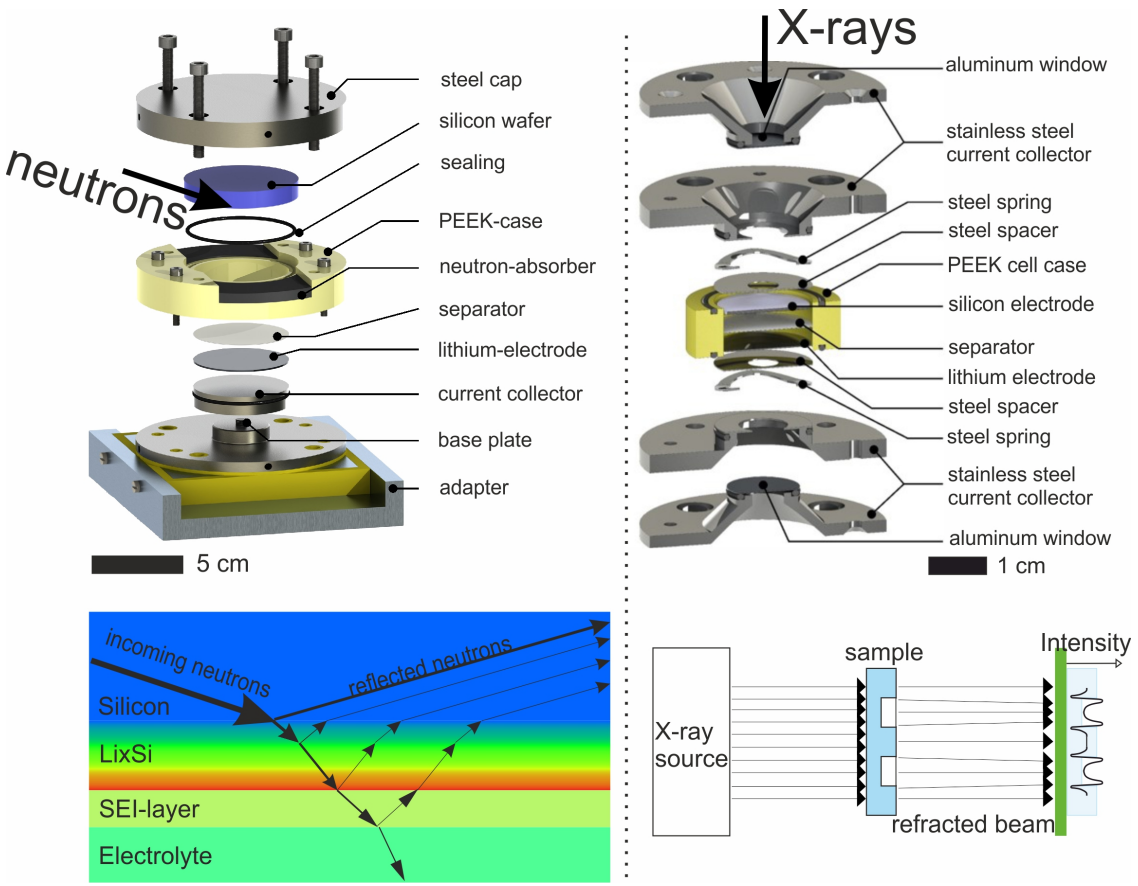

Figure 2.20: *Operando* cells used for neutron reflectometry (on the left) and for radiography (on the right). The NR-cell was used in chapter 3 annd 5, the radiography cell was used in 4. The scale bar at the bottom illustrates the different size. The corresponding beam path within the sample is shown at the bottom part. Left: reflection of the incoming neutrons on the interfaces. The overall reflectance of the cell determines the ratio of reflevted neutrons and transmitted neutrons. Right: Refraction of the X-rays at interfaces within the sample. A monochromatic, collimated beam impinges onto the sample, leading to the deviation of the beam according to Snell's law. Cell images taken with adaptations from [53] and [54].

with a 5 mm hole is placed to avoid any deformation or breaking of the electrodes. The hole decreases the X-ray absorption and improves the signal-to-noise ratio. A spring on each side mediates the mechanical pressure and adjusts the cell volume. The cell case is made of PEEK again, two EPDM-sealings at the top and bottom are employed. The cell is closed with two steel electrodes at

	coin cell	**neutron reflectometry cell**	**radiography cell**
electrolyte volume	250 µl	5 ml	500 µl
geometric surface area of Si	200 mm^2	2290 mm^2	200 mm^2
distance between electrodes	25 µm	2 mm	25 µm

Table 2.2: Summary of the geometric properties of the electrochemical cells

the top and bottom. An aluminum window is clamped between the two electrode parts, together with another sealing. Approximately 0.5 ml of electrolyte is used in the cell. Later versions of this cell also have side inlets in the PEEK-ring for the electrolyte.

2.6 Automatized evaluation of experimental data

In every experiment, data is recorded and needs to be evaluated. The data analysis can be a time-consuming task, especially when using *operando*-measurements due to the huge amount of data. The use of *operando*-techniques also implies a high time resolution of the acquired data compared to the processes within the specimen, so the results should show a continuous trend, *e.g.*, a growth of the lithium-rich layer during lithiation. An automatized data processing could be helpful to combine different measurements and gain additional insights. Fig. 2.21 illustrates the different steps

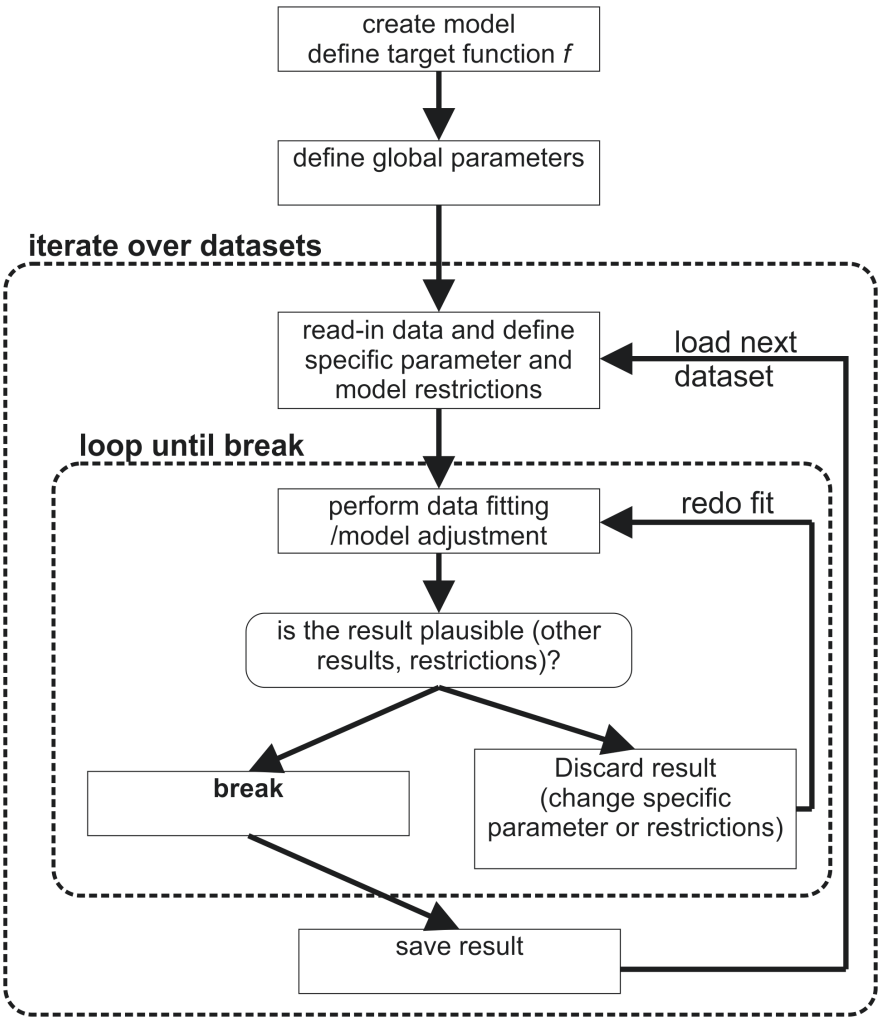

Figure 2.21: The different steps necessary to analyze datasets. The dashed rectangles denote a loop, arrows mark the direction of the workflow.

while analyzing data.
First, the model to analyze the data needs to be created. In the case of reflectivity measurements, this would mean to define the number of layers and their meaningful parameter ranges. For electrochemical impedance spectroscopy, the equivalent circuit needs to be set up. The target function f_n needs to be defined, to calculate the residuum χ of a given set of coefficients. Afterward, global parameters such as the settings for the fit-routine need to be defined. The individual dataset is read in and specific parameters are defined. This could be the state of charge of the electrode, the acquisition date of the dataset, reasonable limits for inidiviual parameters, or many more. Afterward, the fitting of the data is done, meaning the model parameters are adjusted to decrease the residuum according to the target function f_n. After the fitting routine stops, the result is either validated or discarded, starting the fitting process again with either the next dataset or again the same dataset. The target function f_n is of crucial importance since it heavily influences the performance of the whole algorithm. Also, the connection to independent measurements can be done here, *e.g.*, the cell's charging state or pre-characterizations. The whole procedure will be illustrated now for the analysis of EIS-data and neutron reflectometry data.

2.6.1 Evaluation of impedance data

First, the ZHiT-algorithm is applied to remove artifacts from the experimental data (see also chapter 2.2.3). Figure 2.22 shows the basic setup of a Li-Si-cell and their corresponding elements of an equivalent circuit. The first part is an inductor modeling the inductive behavior of the wires used to connect the cell to the potentiostat.
The second part is a resistor representing the ohmic resistances of the electrodes, wires, connections, and the electrolyte, which usually is the largest part of the overall series resistance. Therefore, it is also called solution resistance R_{sol}. The solution resistance depends on the concentration of ions within the electrolyte and also on the cell geometry. At high frequencies, the solution resistance can be extracted directly from the measured impedance values.
The third part is a Warburg element. This element describes the impedance arising from the diffusion of ions within the electrolyte.
The last part is the Faradaic impedance, which models the charge transfer at interfaces. Here at least two interfaces are present, namely the lithium anode/electrolyte and the electrolyte/silicon. The formation of SEI-layers or the growth of a lithiated layer on the surface of the silicon increases the number of layers. A sum of RC-units is used to model the charge transfer reactions, resulting in a distribution of relaxation times.
This equivalent circuit model is taken to fit the data. Depending on the number of spectra, this can be a time-consuming task. Therefore a custom-made software algorithm was used for automatized data analysis [85]. It works as follows:

1. First, the number of relaxations is determined by the number of measured points in the impedance spectra. This means the number of relaxations plus the number of additional parameters (such as the solution resistance or a Warburg impedance) equals the number of

measured points.

2. The relaxation times are distributed equally in the logarithmic space along with the measured frequency or even over an extended range (e.g., extending the lower frequency limit by one order of magnitude).

3. The charge transfer resistance, as well as the additional parameters, are determined by minimizing the difference between the model and the experimental data via a least-squares minimization algorithm. Here the Levenberg-Marquardt algorithm was used.

The charge transfer resistance for different time regimes can be calculated from the distribution of relaxation times by summing up the resistances with time constants within the desired time limits (e.g. $\tau > 1.5$ s). This procedure was used in the chapters 3, 4. The software code can be found in the additional folder and was developed by Dr. Sebastian Risse [85]. A python-based adaptation of this script was used in chapter 5 can be found in the supporting material. The Powell-algorithm is used instead of the Levenberg-Marquardt algorithm to minimize the residuum [86].

2.6.2 Evaluation of reflectometry data

During reflectivity measurements, the intensity $|AA^*|$ of the scattered wave is measured, resulting in the loss of the phase information. This implies, there is no unique transformation from the

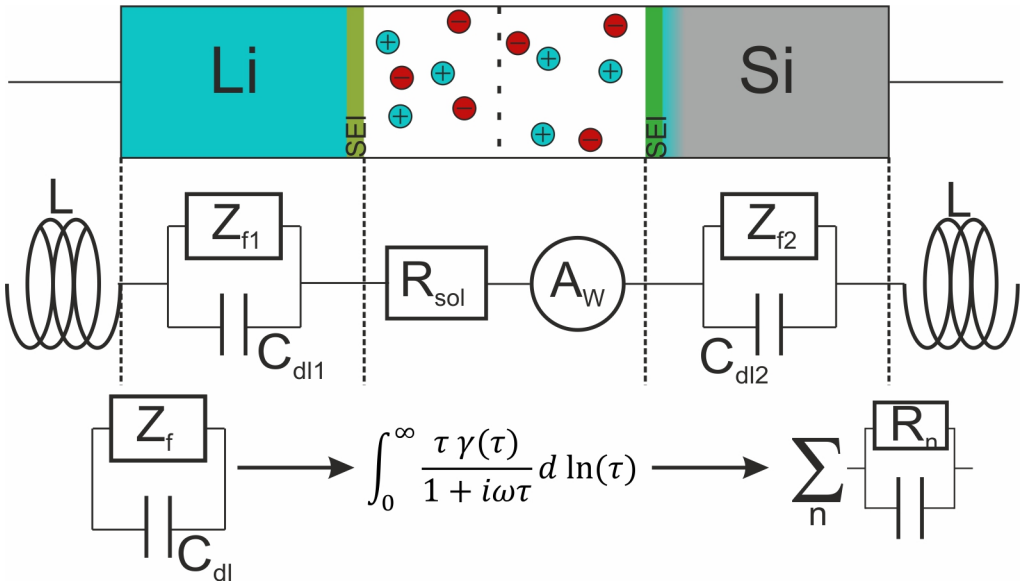

Figure 2.22: Basic setup of a lithium-silicon battery. The wires are modeled with an inductive coil with the inductance L. The resistance of the electrolyte is modeled by an ohmic resistor R_{sol}. A Warburg-element with the coefficient A_W models the ion diffusion. The faradaic impedances Z_f describe the charge transfer processes which occur on interfaces. In parallel to the faradaic impedances, a double layer capacitance can be found. The charge transfer is described by the distribution of relaxation times, which is modeled by a series of R-C-units.

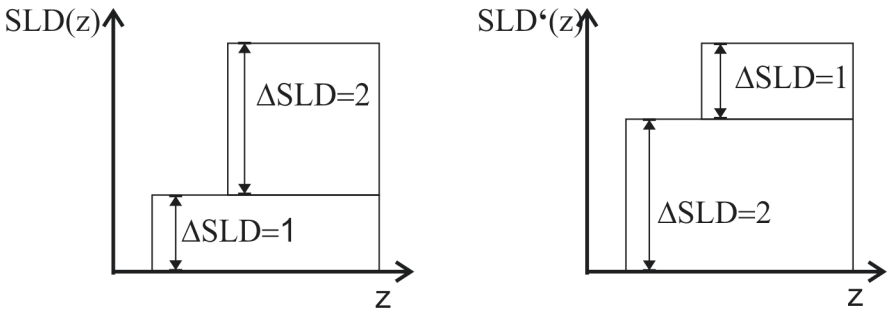

Figure 2.23: Two different scattering length density profiles, which create the same reflectivity signal. Due to the loss of phase information, the two profiles are indistinguishable by their corresponding reflection curve.

reflectivity data to the scattering length density profile [87]. Therefore, the inverse way is taken: A scattering length density profile is generated and the corresponding reflectivity curve is calculated. This calculated curve is compared then to the experimental data.
As a consequence of the phase-loss, different SLD-profiles match the same experimental reflection curve [87]. Figure 2.23 shows an example. Two scattering length density profiles SLD and SLD' create a similar reflectivity signal if they satisfy the condition:

$$\frac{\mathrm{d}SLD(z)}{\mathrm{d}z} = \frac{\mathrm{d}SLD'(z_0 - z)}{\mathrm{d}z} \tag{2.64}$$

Additional data is necessary to discriminate between different scattering length density profiles. In this work, additional knowledge about the sample from independent measurements was taken to validate or reject the resulting profiles. One of the additional information is the charging state of the silicon electrode. During the lithiation process, a binary mixture of lithium and silicon is formed. From the acquired scattering length density, a lithium concentration can be calculated [50]:

$$x = \frac{b_{Si} - SLD \cdot V_{Si}}{SLD \cdot \Delta V_{Si} - b_{Li}} \tag{2.65}$$

Here, x denotes the number of lithium atoms per silicon atom. b is the coherent neutron scattering length of lithium and silicon, which was determined previously [66]. SLD is the SLD-value, V_{Si} denotes the volume per silicon atom (20.04 $\AA^3$ in crystalline silicon). ΔV is the volume expansion per insertion of one lithium into the alloy. Here a value of 14.7$\AA^3$ per lithium atom was given in the literature [34]. Afterward, an integration along the depth direction and multiplication with the electrode area gives a total amount of intercalated lithium, which can be compared to electrochemical results using Faraday's law 2.1. A proper definition of the integration limits is of high importance here.
The importance of additional information shall be illustrated now. An artificial SLD-profile was simulated, and the corresponding reflectivity curve was calculated, adding a small deviation with a gaussian distribution. Furthermore, an measurement error was added, also based on Gaussian

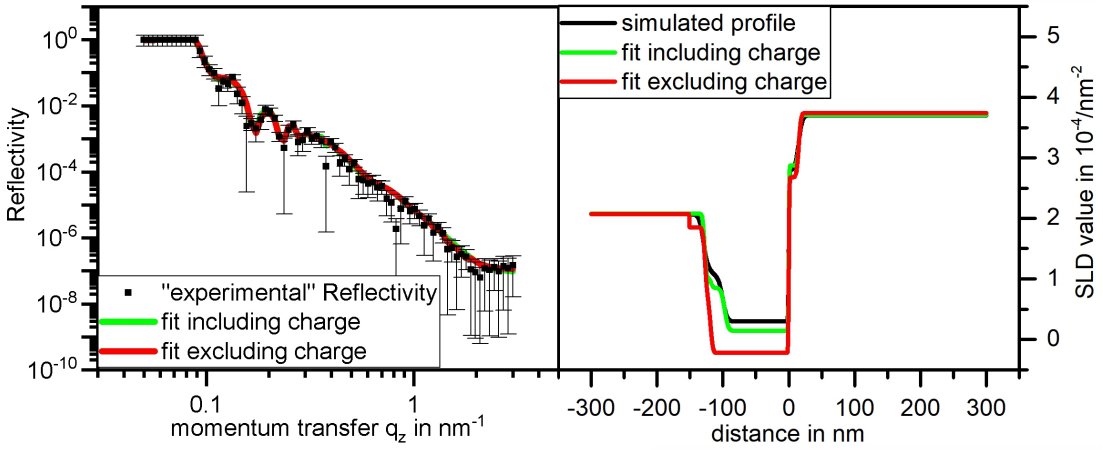

Figure 2.24: Two different results that both match the experimental data. The red line corresponds to a fit taking only the experimental reflectivity data whereas the green line makes use of the charging state as additional information. The green result is the more meaningful profile

random numbers and the momentum transfer. Two fits to the simulated data were done, one including the expected charge to the fit and one without this information. Fig 2.24 shows the results. The two fits differ only slightly. However, their corresponding SLD-profiles show remarkable differences. The simulated profile corresponds to a charge of roughly 1.45 C, the two fits with and without charge information correspond to 1.58 C and 2.08 C, respectively.
The evaluation of reflectivity data can be done by the differential-evolution algorithm [88]. The method generates a set of trial solutions and compares them to the obtained data. Afterward, the different trials are mixed randomly to form the next generation of trial solutions, which are compared again. In this way, a global minimum of the total residua χ_{total} within a specific parameter range calculated by the target function f_n shall be obtained. This algorithm is part of the scipy-package [89]. It was used in a custom-made python script to analyze the obtained reflectivity data. The working principle of the algorithm is shown in fig. 2.25
Figure 2.26 illustrates the work flow of the fit algorithm for chapter 3. Here the global constants are defined first, *e.g.*, an upper and lower limit for the SLD-values or the number of iterations for the fit-routine. The data is read and the differential evolution algorithm is used to minimize the target function f_n, meaning the model is adapted to the data. Afterward the result is verified, meaning the residua is compared to a given number l_2. Also, the fit limits and the resulting parameters are compared. Here less than l_1 parameters should be close to the limits. These parameters are optimized afterward, assuming the global optimum is already close to the result. The whole algorithm repeats for the subsequent dataset. Here, the definition of the target function is of crucial importance. In total, four different parts are added up in the target function, each with an individual weighting factor.

1. The first part χ_{refl} arises from the difference of experimental data and the model's reflectivity.

Here the difference between the logarithm of both reflectivities was taken since the reflectivity data varies by several orders of magnitude. The difference was divided by the error of the measured data.

2. The second part χ_{charge} takes the difference between expected and calculated charge as residual. The calculated charge is determined from the SLD-profile (eq. 2.65), whereas the expected charge is extracted from the cell's electrochemical state. An example would be the final state of the first lithiation. If a charge of 3.0 C was inserted during lithiation and 2.7 C was extracted during subsequent delithiation, the expected charge would be in this range.

3. The third part χ_{change} comes from the definition of an *operando*-measurement. The timescale of the structural changes of the sample is larger than the time resolution of the measurements. Therefore, no substantial differences are expected between the SLD-profiles of successive measurements.

4. The fourth part χ_{bin} is simply an acceptance/rejection criteria. It is set to tremendous values if artifacts are found within the SLD-profile, *e.g.*, by a roughness exceeding the associated

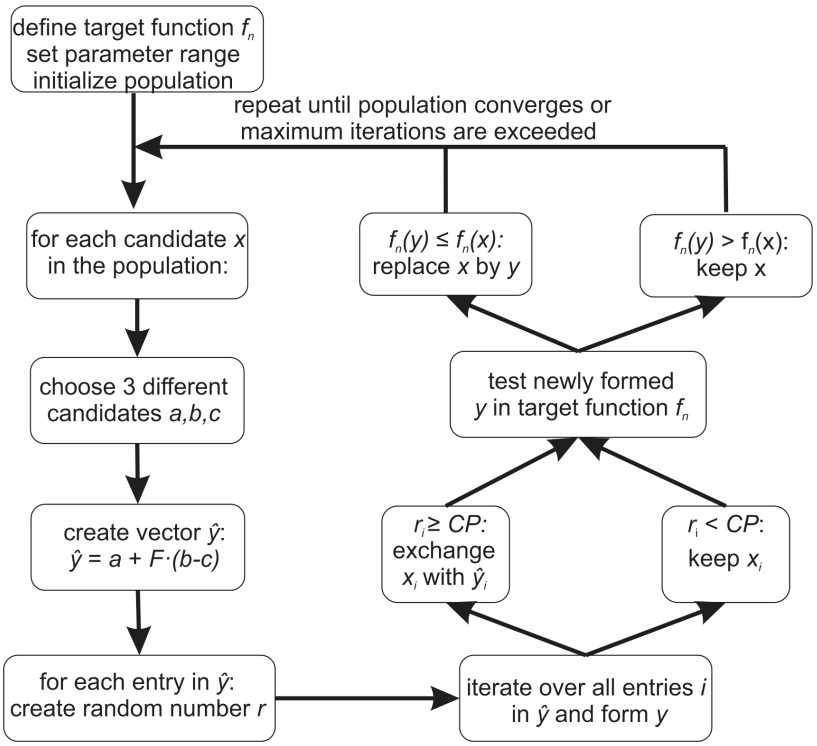

Figure 2.25: The differential evolution algorithm. The target function f_n is used to compare the residual of the different candidates to each other based on their coefficients. The parameter range specifies the upper and lower limits for the individual coefficients in each solution. Different strategies can be used to initialize the population, choosing the candidates a,b,c, and obtaining y from x and $\hat{y}$.

layer thickness. Also, a higher concentration of lithium in the bulk silicon than at the surface seems contradictory and is not in line with previous experiments [50].

The sum of these four parts, each with its individual weighting factor, represents the total residuum value of the fit.

$$\chi_{total} = w_1 \cdot \chi_{refl} + w_2 \cdot \chi_{charge} + w_3 \cdot \chi_{change} + w_4 \cdot \chi_{bin} \tag{2.66}$$

The algorithm was improved further for chapter 5. Part 3 of the target function was changed slightly, comparing now the resulting SLD-profiles instead of the parameters. Up to three parameter sets before and after the currently chosen dataset were used as a comparison. These were weighted according to the time difference to the current dataset using the normal Gaussian distribution. The corresponding SLD-profiles were determined and the difference of the profiles were used to calculate

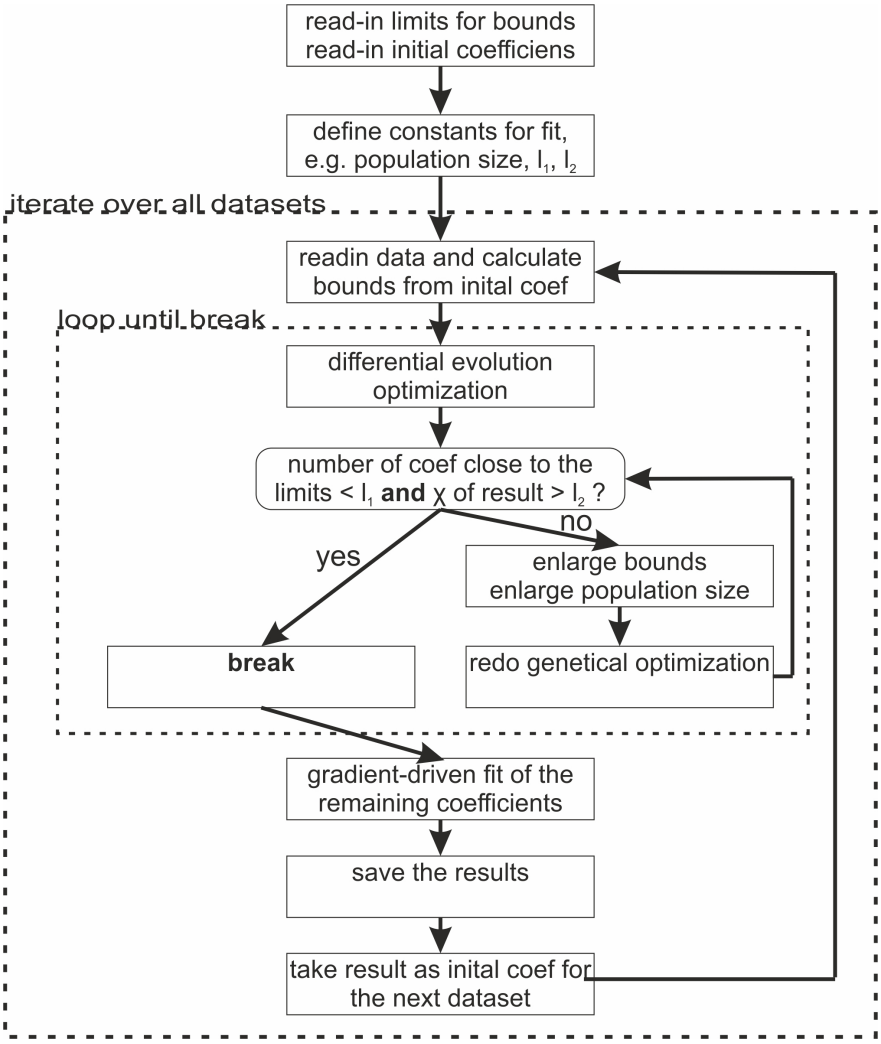

Figure 2.26: The data processing algorithm used in chapter 3 to evaluate the data. The dashed rectangles denote loops, the round-edged rectangle denotes an 'if-condition'. Arrows denote the direction of the workflow.

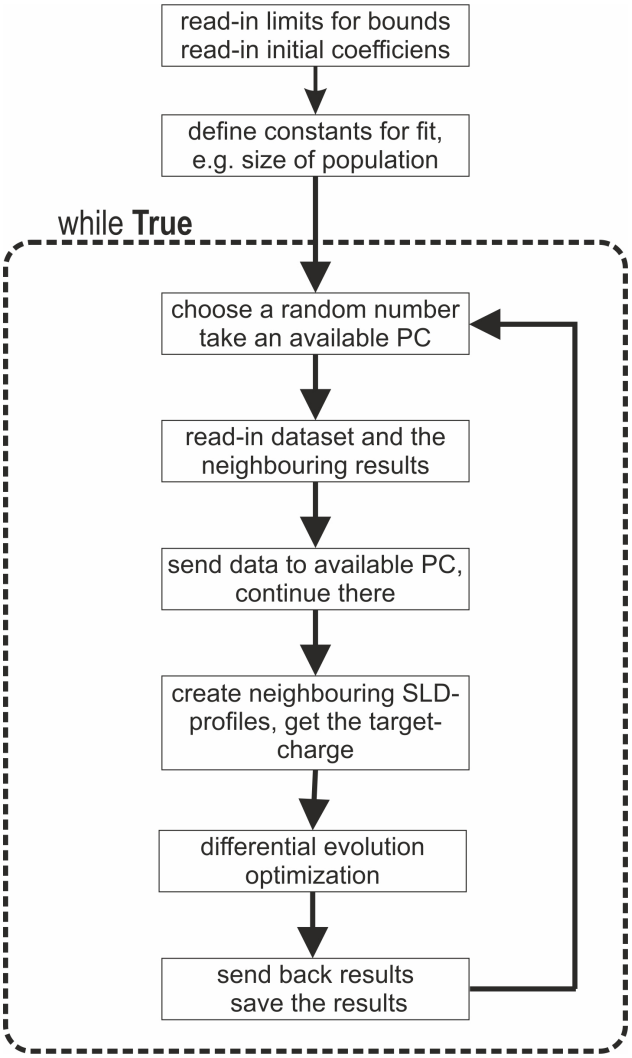

Figure 2.27: The data processing algorithm used in chapter 5 to evaluate the data. The dashed rectangle denotes a loop. Arrows denote the direction of the workflow.

the residuum, instead of a comparison of the coefficients.

The fit algorithm was repeated several times to improve the result stepwise. A dataset was chosen randomly from all available datasets, but an equal processing number per dataset was ensured. In the first round, only part one, part two and part four of the residuum were used to create an initial set of results. These results were refined later in an iterative algorithm, also using part three of the residua. In this way, sudden changes in the SLD-map were removed, since they contradict to the principle of an *operando*-measurement. The individual weighting factors ensured the domination of the first part of the residuum over part two and three. The random choice of a dataset enables the use of several computers connected over a network to decrease the computational time. Up to 16 computers were used in parallel, forming a distributed computational cluster. The working scheme of the algorithm is shown in fig. 2.27, fig. 2.28 illustrates the iterative smoothening of the resulting SLD-profiles. The initial result without any correlation between the profiles is shown on

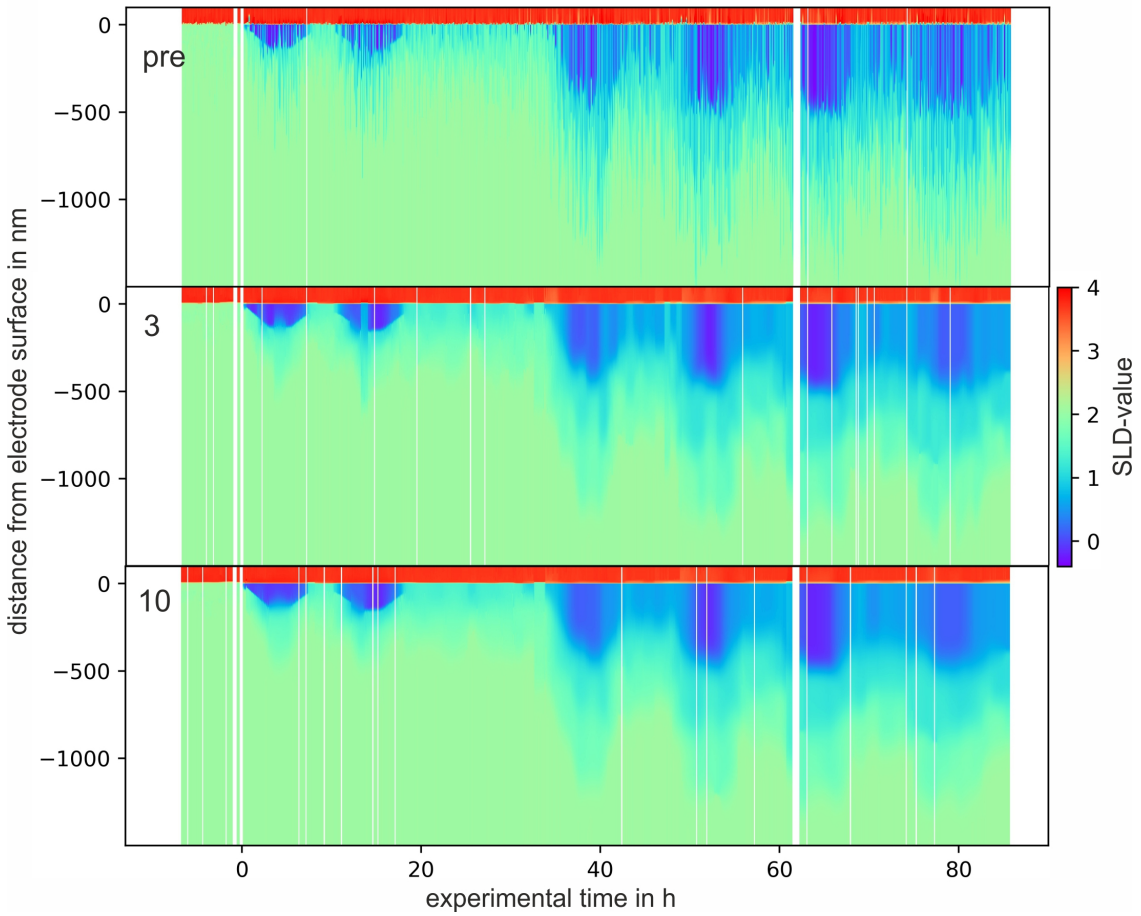

Figure 2.28: Smoothing of the data processing algorithm. The upper part shows the situation before the smoothing process. The middle part shows the result after three iterations, the lower part after ten iterations. Non-meaningful sudden changes in the SLD-profiles are removed. The first two parts of the residuum, calculated from the reflectivity and the charge, do not change significantly.

top, the SLD-map in the middle shows the result after three steps, the lower part shows the result after ten steps. Clearly, the resulting SLD-profiles become smoother towards the experimental time. Unmeaningful sudden changes between neighboring profiles are discarded. This procedure does not increase the first two parts of the residuum significantly.

Chapter 3

Probing the lithiation of crystalline silicon with *operando* neutron reflectometry

Parts of this chapter were also published as peer-reviewed research paper with the title: Surface structure inhibited lithiation of crystalline silicon probed with *operando* neutron reflectivity [53]. DOI: 10.1016/j.ensm.2018.11.032

3.1 Introduction

Silicon electrodes suffer from a strong capacity fading caused by the volume expansion [3], as shown in 1.4 and described previously. This is accompanied by a continuous growth of the SEI-layer since the expansion introduces new silicon surface to the electrolyte where the SEI-layer starts to grow [21]. This process consumes electrolyte and leads to a dry-out of the electrochemical cell. Furthermore, the side reactions drain charges, which decreases the overall Coulombic efficiency.
The origin of these processes is the surface of the silicon electrode, which gets in contact with the electrolyte. Also, the insertion of lithium into silicon starts at the surface. Consequently, the surface is of high importance for a mechanistic understanding of the lithiation process. Reflectometry is therefore an ideal technique to tackle the aforementioned challenges since it is sensitive to surfaces and interfaces as well as thin layers (Chapter 2.3). Especially neutron reflectometry can be utilized to study the lithiation of silicon since the scattering lengths of silicon and lithium show a high contrast [66]).
Neutron reflectometry was applied already to characterize the SEI-layer growth and the lithiation-induced volume expansion of silicon. Jerliu *et al.* investigated the expansion of a thin layer of amorphous silicon [90]. Veith *et al.* found a reaction layer which formed spontaneously after five days of aging [41]. The voltage-dependent occurrence of the SEI-layer was investigated by Veith *et al.*, showing also again the expansion of silicon at various voltages [49]. However, the growth

process of the SEI-layer is hard to follow in these three studies since they were done under in-situ conditions and with amorphous silicon.

Seidlhofer *et al.* investigated the lithiation of crystalline silicon(100) using *operando* neutron reflectometry [50], whereas Cao *et al.* employed operando X-ray reflectivity [91]. Seidlhofer *et al.* found the formation of two distinct lithiated zones, where the zone higher lithium concentration is at the surface of the silicon electrode and much thinner than the second zone with lower lithium content. Furthermore, the growth of an SEI-layer is observed, even without applied current. However, the Coulombic efficiency of the cell is relatively low, indicating the occurrence of parasitic side reactions, which may cause artifacts.

Contrary to the previous work, Cao *et al.* employed X-rays instead of neutrons for their reflectivity measurements [91]. Therefore, the sensitivity for the inorganic part of the SEI-layer is increased, whereas the organic part becomes invisible. They found the formation of an SEI-layer around 0.8V, followed by the lithiation of the silicon. In contrast to Seidlhofer *et al.*, a sharp transition from the lithiated zone towards the bulk silicon was observed. Also, the formation of the highly lithiated equilibrium phase $Li_{15}Si_4$ was reported but not observed by Seidlhofer *et al.*. However, also in this study, the Coulombic efficiency is relatively low (about one-third), which may cause wrong interpretations of the data. Furthermore, the high energy of the X-ray photons may accelerate the decomposition of the electrolyte and, therefore, influence the SEI-layer formation.

This experiment aims at a better understanding of the growth of the SEI-layer. This shall be related to the coulombic efficiency. We were able to visualize side reactions within the system under *operando*-conditions over four cycles. The amount of charge consumed for side reactions was determined as well as the time-resolved change of the lithium profile within the silicon. Additional electrochemical impedance spectroscopy (EIS) links the structural results to the electrochemical properties.

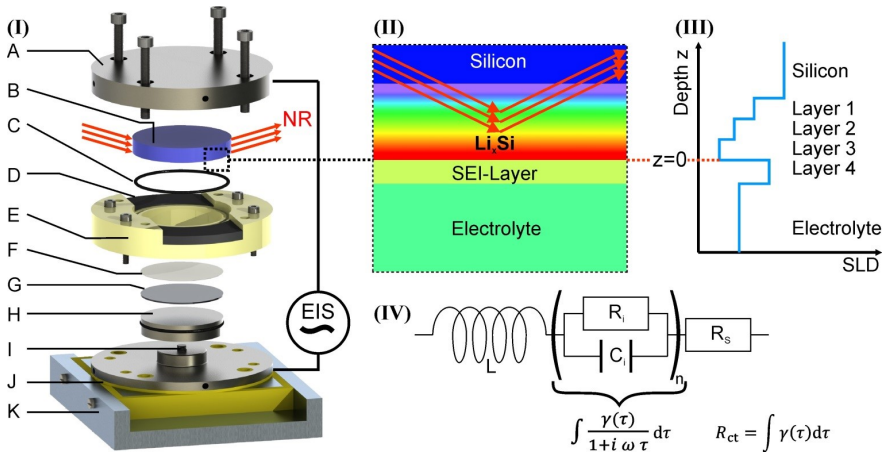

Figure 3.1: Schematic overview of the experiment. On the left, the employed *operando*-cell is shown. The incoming neutrons get reflected on the interfaces within the silicon electrode(middle), which is modeled by a 4-layer system (right part). *In-situ* electrochemical impedance spectroscopy was performed for additional insights. The corresponding equivalent circuit is shown on the lower part of the image. Taken from [53].

First, the electrochemical behavior of a coin cell will be discussed, which serves as a comparison. Afterwards, the employed model for the data analysis will be described (see also chapter 2.6.2). The obtained results from *operando* neutron reflectometry will be linked to the cell's charging state, followed by a discussion of the impedance data. At the end of the chapter, a brief conclusion is given together with the experimental details.

3.2 Electrochemical performance of a Li-Si reference coin cell

Figure 3.2 shows the results obtained from a coin cell that employs a (100)-single crystalline silicon wafer and a metallic lithium sheet as electrodes. Only the first three cycles are shown. During the initial resting period, several impedance spectra were recorded and evaluated using the algorithm described in chapter 2.6.1. The results with a high residua were discarded (sum of relative residua in real and imaginary impedance part $> 5\%$). The voltage curve shows a drop from roughly 2.5 V to 1.8 V during the six hours resting period. Afterward, a drop to the low-voltage plateau occurs, which

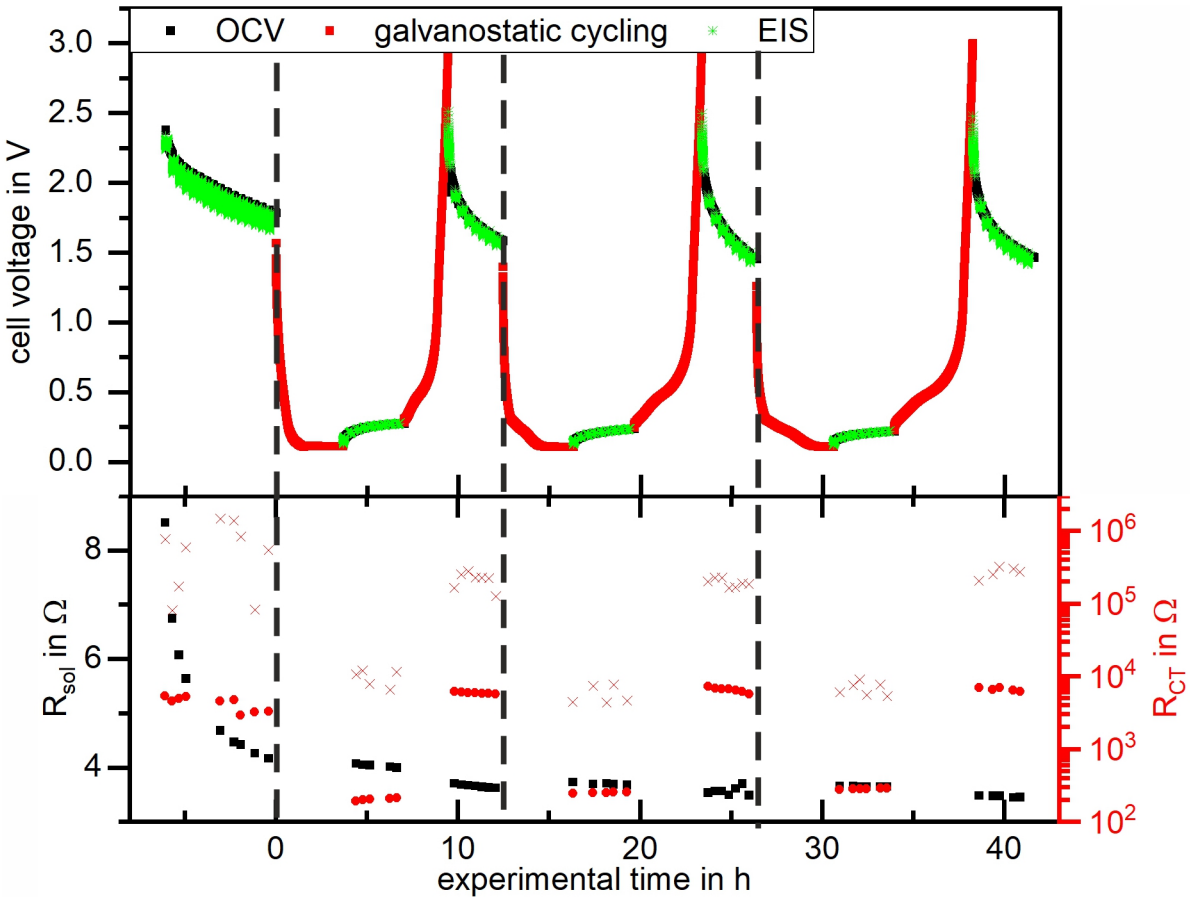

Figure 3.2: Experimental results of a Li-Si coin cell. Top: voltage curve. The OCV-part is drawn in black. The galvanostatic cycling is shown in red. The positions of impedance spectroscopy measurements are denoted in green. Bottom: determined solution resistance (black), together with the charge transfer resistances for fast(τ<1.5 s, solid red circles) and slow (τ > 1.5 s, red crosses) relaxation processes.

is around 110 mV. This voltage indicates the lithiation of crystalline silicon, but not the formation of the highly lithiated silicon equilibrium phase [3, 50]. The voltage drop is not instantaneous but requires approximately one hour. Within this time, side reactions may occur, such as the decomposition of impurities or the reformation of the SEI [3, 92].

Once the cell voltage was lower than 250 mV, the lithiation sequence is continued for another three hours. The subsequent OCV-period shows a voltage relaxation, reaching 0.275 V after 3h. Sethuraman *et al.* observed similar relaxation curves [93]. They also observed the presence of side reactions, which discharge the electrode. Therefore, a determination of the lithium concentration within the silicon electrode based on the OCV-relaxation is not possible. After the OCV-period, the delithiation of the cell starts, showing a voltage increase with time. Once the voltage reaches 0.65 V, the voltage curve slope increases, indicating the depletion of lithium within the silicon electrode. The subsequent step is again a 3-h OCV period, showing a voltage drop to 1.6 V.

The subsequent lithiation shows an additional feature compared to the first cycle. Here the lithiation of amorphous silicon can be observed, which is indicated by a sloping voltage starting around 300 mV [29]. This shows the amorphization of silicon during the lithiation/delithiation process [28, 29]. Surprisingly, the amorphous silicon is lithiated after 1.5 h already, whereas the previous charge took 2.5 h. Therefore, the lithiation of amorphous silicon may continue in parallel to the lithiation of the underlying crystalline silicon, or the lithiation degree is lower than in the previous cycle. The Coulombic efficiencies of the three cycles are 87.2 %, 90.8 %, and 96.8 %.

The solution resistance decreases during the initial resting period from 9 Ω to 4 Ω. This resistance decrease is most probably caused by an ongoing wetting process [94]. During cycling, the solution resistance changes depending on the charging state: in the lithiated state, the solution resistance is higher than in the delithiated state, which might be caused by the charging state-dependent electrical properties of silicon or the SEI-layer [95, 96]. The resistance difference between lithiated and delithiated state is roughly 0.2 Ω.

The distribution of relaxation times is split into fast processes ($\tau < 1.5$ s) and slow processes ($\tau > 1.5$ s). Fig 3.2 shows the results. It reveals information about the charge transfer resistance at specific time domains. A high charge transfer resistance indicates a delayed or hindered charge transfer and vice versa. Both charge transfer resistances are increased in the delithiated states and decreased in the lithiated state. During the initial OCV-period, the slow charge transfer resistance varies over one order of magnitude, most probably due to an initial wetting process and the growth of an SEI-layer [41]. The charge transfer resistance of the slow relaxation processes is approx. 1.5 - 2 orders of magnitude higher than the fast relaxation processes. The results indicate a delayed charge transfer in the delithiated state compared to the lithiated state. This may originate from the growth of layers on the electrodes or a morphology change of the surface layers, which decreases the ionic conductivity drastically. At least two processes are involved since both charge transfer resistances change.

From these results, several open questions remain: The origin of the increased charge transfer resistance in the delithiated state is unclear. Also, the kinetics of the lithiation and the origin of the charge loss cannot be studied due to missing structural information. Furthermore, lithiation of the

amorphous silicon does not match the capacity expected from the previous cycle. *Operando*-neutron reflectometry was used to tackle these issues.

3.3 Results of morphological data analysis

Roughly 490 reflectivity datasets were acquired during operando-measurements. Therefore, an automated fitting script was implemented in Python to analyze the operando-measurements, as described in chapter 2.6.2. The scans during OCV-periods were analyzed using Motofit [97] and serve as reference-points. As discussed already in Chapter 2.3, several SLD-profiles match the same reflectivity dataset equally well. Additional information from the electrochemical measurements has been used for the data analysis in order to find the SLD-profile, which fits to the investigated

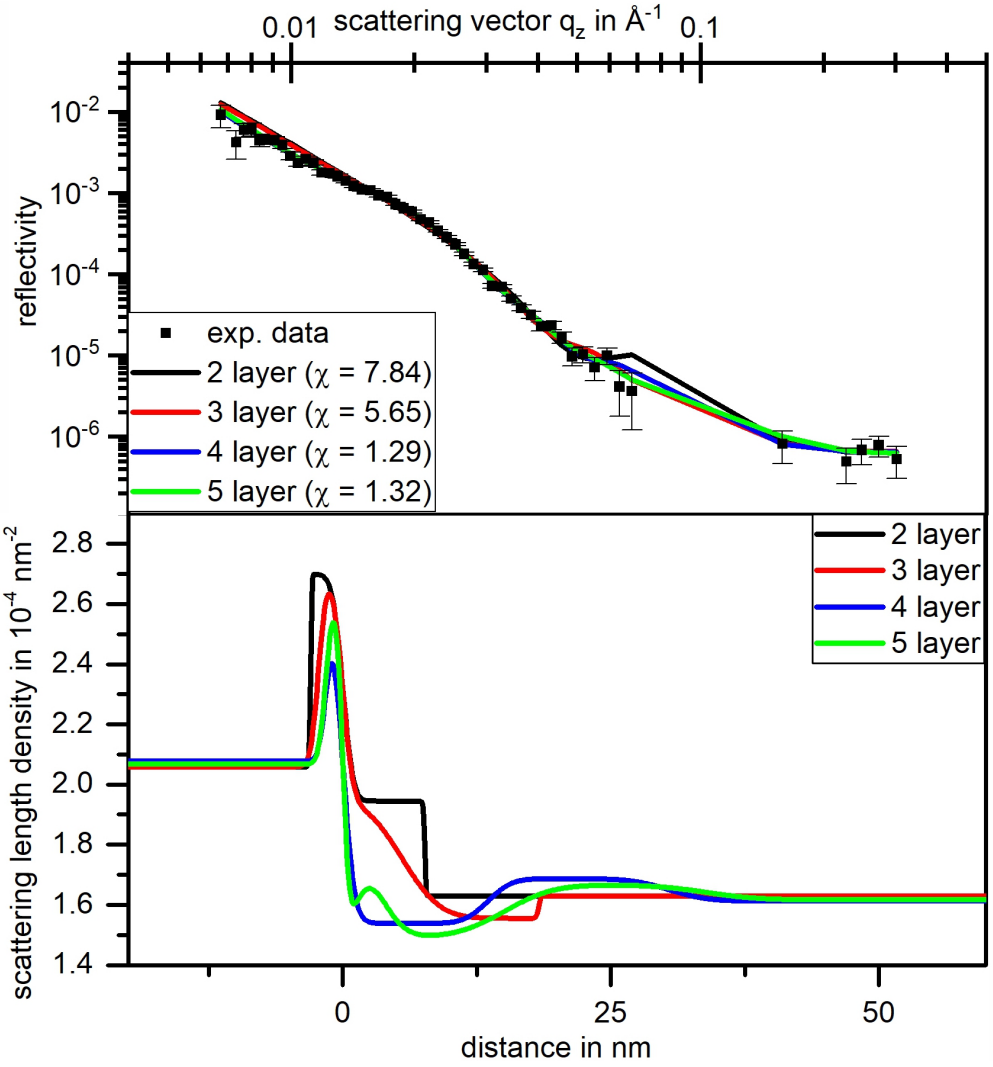

Figure 3.3: Reflectivity data of the virgin state together with a two-layer-, three-layer- and 4-layer-fit. The corresponding χ^2 values are shown in the legend. The fit using 3 SEI-layers and the native oxide layer is the best fit of these three. The corresponding SLD-profiles can be found on the right part.

system. The lithium concentration within the silicon is calculated using equation 2.65 [50] and compared to the expected value. The calculated charge is compared to the value expected from electrochemistry and increases the residuum of the fit if the deviation is too large. Furthermore, the result is compared to the preceding result to avoid sudden changes. Profiles containing artifacts from high roughnesses and not appropriate lithium concentration are also discarded. A more detailed description can be found in chapter 2.6.2. The differential evolution algorithm [88] was used for optimization together with a gradient-driven optimization (Powell-algorithm [86]) to speed up the convergence close to the result.

The SLD-model consists of a 4-layers containing 3 lithiated layers with increasing lithium content and one SEI-layer, similar to profiles reported in the literature [50]. The charge was calculated from the three lithiated layers. In the pristine state, the first layer represents the native silicon oxide layer, whereas the three remaining layers were used to form the SEI-layer. The use of fewer layers resulted in a poor fit, as shown in fig. 3.3. Using more layers does not improve the residua. The reflectivity measurements acquired during OCV-periods were evaluated using Motofit and served as an anchor point. The measurements taken during cell cycling were evaluated with the python algorithm mentionned above and described in chapter 2.6.2.

The results were aligned with the experimental time (Fig. 3.4). In total, three independent measurements were taken: Neutron reflectometry (A), electrochemical cycling (B, C), and impedance spectroscopy (D). The dotted vertical lines indicate the beginning of a new cycle, starting with a lithiation/discharge process. The figure is split into five time regimes ((I) to (V)), which will be discussed separately now.

The first part (I) shows the pristine state of the sample. An OCV of 2.78 V was observed, together with a cell resistance of 1.11 Ω. A native oxide layer with a thickness of 1.7 nm is present on the silicon surface. The scattering length density of $2.6 \cdot 10^{-4}/\mathrm{nm}^2$ is lower than the theoretical value of $3.47 \cdot 10^{-4}/\mathrm{nm}^2$. Therefore the oxide layer is not SiO_2 but a sub-oxide, which was already reported by Al-Bayati *et al.* [98]. A SEI-layer on top of the native oxide layer can be found. The formation of a layered structure before cycling is frequently described in the literature [41, 49–51, 91, 99–101]. It consists of an inner part with a lower SLD and an outer part with a higher SLD. Such a bilayer structure was already reported by Veith *et al.* [49] and Tokranov *et al.* [102, 103], who identified the inner part as mainly inorganic SEI-layer and the outer part as mainly organic SEI-layer. According to Veith *et al.*, the inner part consists of 80% LiF and 20% organic species, which corresponds to an SLD-value of $1.47 \cdot 10^{-4}/\mathrm{nm}^2$. This is close to the value found in this study equals ($1.52 \cdot 10^{-4}/\mathrm{nm}^2$). The observed SEI-layer introduces a charge transfer resistance in the low-frequency regime of roughly 78 kΩ ($\tau < 1.5$ s).

Part II shows the first discharge. A current of 250 µA was applied, the voltage drops to 2.3 V. Here, the voltage was nearly constant for roughly seven hours. Within this voltage plateau, a layer forms on the silicon electrode. The thickness of the layer is approx. 120 nm, the scattering length density is slightly lower than the surrounding electrolyte. Most probably, this layer originates from the decomposition of the electrolyte and the formation of an SEI-layer. The decreased SLD-value indicates the incorporation of lithium into the layer. Comparable observations were made by Seidlhofer

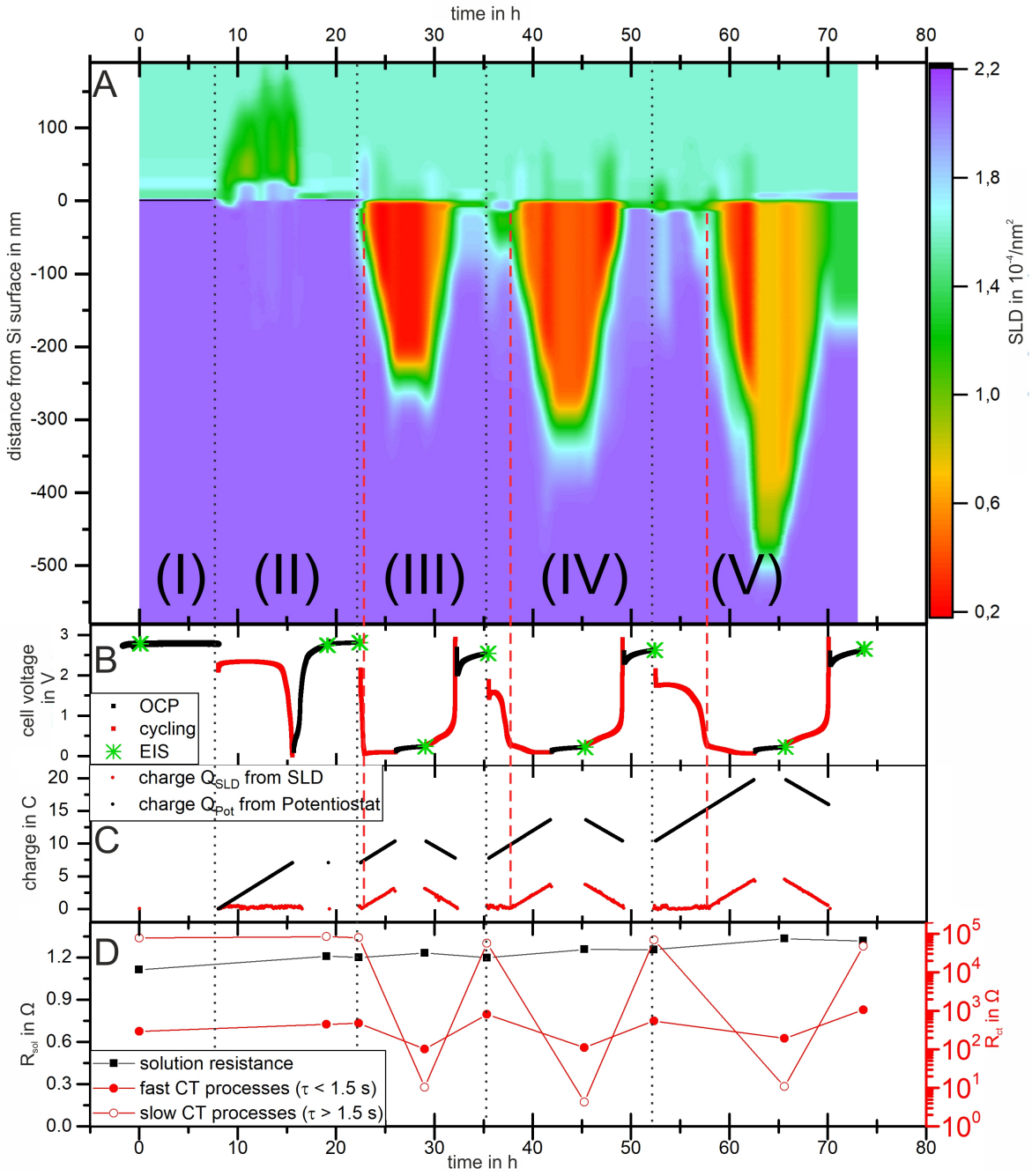

Figure 3.4: Results obtained during the *operando*-experiment. The parts (I) to (V) indicate the virgin state (I) and the four cycles (II - V) and are separated by dashed lines. Part A: obtained SLD-colormap. Low SLD-values indicate a high amount of lithium. Part B: measured cell voltage. The red line indicates an applied current, the black line an OCV-measurement. At the positions marked with a green star, impedance spectroscopies were performed. Part C: calculated (black) and determined charge(red). The calculated charge is the integration of the current provided by the potentiostat. The determined charge was calculated based on the SLD-profile (see also eq. 2.65 in chapter 2.6.2). Part D: Solution resistance R_{sol} and charge transfer resistances R_{ct} obtained from the impedance spectroscopy measurements. Taken from [53].

et al., who found an enrichment layer prior to lithiation of silicon [50]. At the end of the plateau, the voltage decreases to 10 mV, accompanied by the dissolution of the SEI-layer [49, 91, 92]. Here the lower voltage limit stops the discharge to avoid lithium plating [104]. Afterward, the voltage relaxes to 2.9 V, which is comparable to the initial OCV. Therefore, no lithiation took place, which is supported by the neutron reflectometry results. Also, the impedance spectra is equivalent to the pristine state. In conclusion, the charge provided in this cycle is lost in side reactions and does not participate in the lithium storage.

Part III of the graph shows the second cycle. Once the discharge started, the voltage dropped down to approx. 1.5 V. After 15 minutes, another voltage drop occurred, reaching a voltage plateau around 90 mV. Here the lithiation of crystalline silicon starts [3]. In the first 15 minutes of the lithiation process, only small changes in the reflectivity were observed. Again, a surface layer is formed with a thickness of 60 nm and a SLD-value of $2 \cdot 10^{-4}/\mathrm{nm}^2$. Contrary to the first cycle, the lithiation starts afterwards since the SEI-layer thickness is sufficiently small. The native silicon oxide layer is removed during the first steps of the lithiation. Tardif et.al suggest the conversion into $LiSi_xO_y$ [105]. Subsequently, the lithium enters the silicon. The lithiated layer consists of an inner low-lithiated phase and an outer phase with a higher lithiation degree. The thickness of the low-lithiated phase is nearly constant over the whole cycle. Seidlhofer *et al.* also observed two distinct lithiated phases [50], but the thickness of the highly lithiated layer is one order of magnitude higher in this experiment. This thickness increase can be associated with the current increase, which is also one order of magnitude. The lithiated phase propagates into the silicon with a velocity of 19 pm/s. At the end of the lithiation process, a thickness of 238 nm was determined. The amount of incorporated lithium corresponds to a charge of 3.1 C. This was calculated assuming a binary mixture and an expansion of the silicon as described in eq. 2.65 and also elsewhere [50]. This matches the amount of charge provided by the potentiostat during this period. Only 1.9 % of the charge is lost in side reactions.

After three hours, an OCV-value of 230 mV was measured, which is in good agreement with values reported in the literature [3, 93]. From the SLD-value, a lithium concentration of $\approx Li_{1.3}Si$ can be determined. The SEI-bilayer-structure cannot be found anymore and also no silicon oxide layer is observed. The impedance spectroscopy reveals decreased charge transfer resistances, indicating the absence of surface layers, which could impede a further charge transfer.

During the subsequent delithiation process, a moving phase boundary between the silicon and the lithiated phase was observed, which is slightly faster than the previous lithiation (23 pm $\cdot$/s). Again, the SLD-profile change can be transformed into a release current of lithium (0.889 C/h). This value is close to the current set by the potentiostat (0.868 C/h), only a difference of 2.4 % can be determined, indicating some irreversible side reactions. An SEI-layer was formed when the voltage reaches 2.9 V. The layer exhibits a thickness of 7 nm and an SLD-value of $1.5 \cdot 10^{-4}/\mathrm{nm}^2$. 0.28 C of lithium was trapped within the silicon on a surface layer. During the subsequent OCV-period the voltage drops to 2.54 V, and a binary SEI-layer has formed again. No silicon oxide layer is detected anymore, which was shown already elsewhere [50].

The third cycle (part IV) is comparable to the previous cycle. An initial voltage shoulder at 1.5

V can be found, which lasts for ≈ 80 minutes. Again, a bilayer-structure grows and dissolves during this voltage shoulder. The thickness of the layer is ≈ 50 nm. The bilayer collapses when the lithiation starts. First, the amorphous silicon is lithiated, indicated by a slowly decreasing voltage starting at 250 mV. The beginning of the voltage plateau at 90 mV indicates the lithiation of the underlying crystalline silicon. Here the thickness of the lithiated phase is ≈ 210 nm, which is close to the lithiation depth of the previous cycle. The lithiated zones interface moves with 17 pm/s, which is comparable to the prior cycle. No difference in the lithiation speed for the amorphous and crystalline phase was found. At the end of the lithiation, the lithiated zone reaches a depth of 310 nm, corresponding to an incorporated charge of 4.3 C. The subsequent OCV-period shows a voltage relaxation to 210 mV. The concentration of lithium ions within the highly lithiated phase is roughly $Li_{1.3}Si$, similar to the previous cycle.

During delithiation, the thickness of the lithiated layer shrinks by 20 pm/s. The concentration of lithium within the lithiated layer stays nearly constant until the end of the delithiation. In the second half of the delithiation, a surface layer is formed again. This layer has an SLD-value of $1.3 \cdot 10^{-4}/nm^2$ and a thickness of approximately 65 nm. Due to the decreased SLD compared to the surrounding electrolyte, an enrichment of lithium can be assumed. In the subsequent OCV-period, only a single SEI-layer can be found instead of a bilayer structure. High charge transfer resistances (550 Ω and 69.6 kΩ for the slow and fast relaxations, respectively) were found. Roughly 0.38 C of lithium remains within the silicon.

The fourth cycle starts again with a voltage shoulder around 1.7 V, but for five hours now. The voltage plateau is accompanied by the formation of a surface layer with a thickness of 30 nm and a SLD-value of $1.7 \cdot 10^{-4}/nm^2$. Afterward, the voltage drops down to 247 mV and the lithiation starts. At a lithiation depth of 250 nm, the voltage reaches the lower plateau around 63 mV, indicating the lithiation of crystalline silicon again. A depth of 300 nm would be expected here since this was the lithiation depth of the previous cycle. Therefore, a parallel lithiation of crystalline silicon and the adjacent amorphous phase may occur. A final thickness of 311 nm was observed with an SLD-value of $0.25 \cdot 10^{-4}/nm^2$, corresponding to a lithium concentration of $Li_{1.6}Si$. A charge of 4.5 C was stored within the silicon.

In the successive OCV-step, an expansion of the lithiated layer was observed, while the total charge stays constant. This cannot be explained by cracking or spalling of active material since it would end up in a different lithium content within the silicon. Therefore, the relaxation of internal stress is assumed, as observed already by Sethuraman *et al.* [106]. The OCV-measurement yields 216 mV in the final state, which is comparable to the previous cycles. A surface layer is formed with a thickness of 11 nm and an SLD-value of $1.8 \cdot 10^{-4}/nm^2$.

The following delithiation is similar to the previous cycles. 3.9 % of the current was lost in faradaic side reactions, which is the difference between the current determined from the change of the lithiated phase and the current supplied by the potentiostat. Again, a surface layer is formed at the end of the delithiation, growing further in the successive OCV-period. This layer exhibits a final thickness of 12 nm and an SLD-value of $1.94 \cdot 10^{-4}/nm^2$. A charge of 0.9 C remains within the silicon electrode.

These observations can be summarized as follows: In the first cycle, the lithiation was prevented by a massive surface layer, which may originate from the assembly five days before the experiment [41]. Once this layer was dissolved, the voltage dropped down to the lower voltage limit, possibly due to an overpotential. In the successive cycles, lithium was inserted into the silicon once an initial surface layer was dissolved. The lithiation effiency afterwards was in the range of 0.946 and 0.981, which was determined from the change of the SLD-profiles and the potentiostat's current. During delithiation, no inhibiting layer was found, although surface layers were formed. A small amount of lithium remained in the silicon after delithiation. This was also observed previously [107, 108]. The lithiation degree within the highly lithiated phase reached $Li_{1.6}Si$. The velocity of the lithiation front was slightly faster for the delithiation process, but no difference for the crystalline or amorphous phase was found. Therefore, the lithium transport within the silicon was not the rate-limiting step. Otherwise, the amorphous phase should show a higher lithiation speed due to the higher diffusion coefficient compared to the crystalline phase [109, 110].
The EIS-measurement reveals an alternating behavior of the obtained charge transfer resistances, as also shown in part D of fig. 3.4. The corresponding Bode-plots of the impedance are shown in

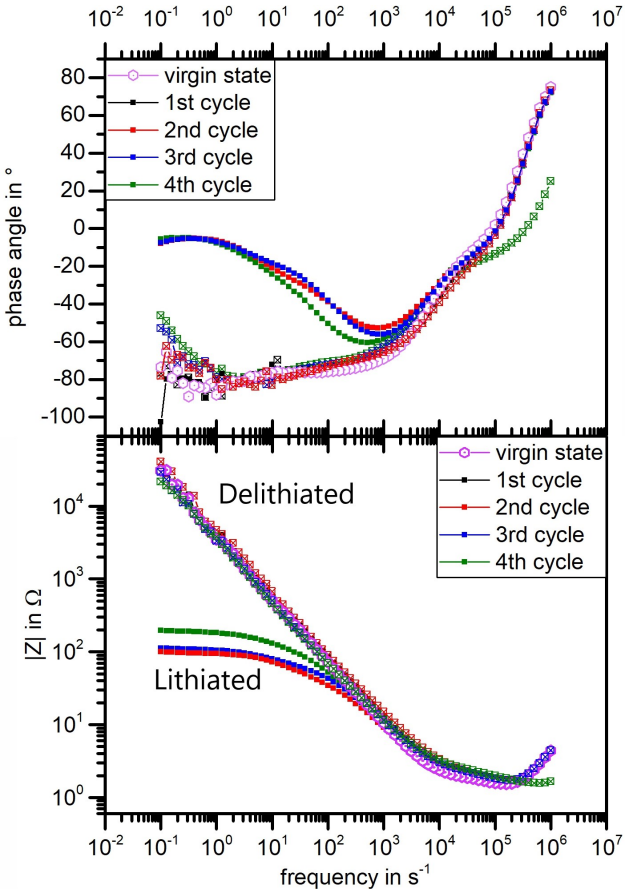

Figure 3.5: Bode-plot of the obtained impedance data. The phase angle is shown on the top, whereas the modulus of the impedance is shown at the bottom. Clear differences between lithiated and delithiated states can be found at low frequencies.

fig. 3.5. Both charge transfer resistances are considerably higher in the delithiated state than in the lithiated state, indicating the inhibition of charge transfer processes. Also, the complete first cycle shows a high charge transfer resistance. This leads to large differences between the lithiated states and the delithiated state at low frequencies, indicating the growth of an additional layer. The solution resistance R_{sol} of the cell stayed nearly constant during the experiment. Only a slight increase from 1.11 Ω to 1.3 Ω was observed. A shallow increase of R_{sol} in the lithiated state occurs, as already observed in the coin cell experiment.

3.4 Conclusion

With *operando* neutron reflectometry the lithiation of crystalline silicon was tracked. The growth and shrinkage of the lithiated phase were observed. Before the lithiation starts, a surface layer is formed and also dissolved. These surface layers show thicknesses in the range of 30 to 60 nm. Once the surface layers are removed, lithium insertion into the silicon starts. The lithium incorporation matches the current provided by the potentiostat. Therefore, no parasitic side reactions were found once the surface layers are dissolved. Surface layers did not hinder the delithiation. The charge transfer inhibiting nature of the surface layers was also proven by *in-situ* impedance spectroscopy, showing high charge transfer resistances at the delithiated state.

3.5 Experimental details

A description of the cell was given in Chapter 2.5 and is shown in Fig. 3.1. A lithium metal ribbon bought from SigmaAldrich (99.9 % Trace Metals basis) was used as the counter-electrode, a single-crystalline silicon wafer (6 cm in diameter, 1 cm thickness, bought from Siltronix) was used as the working electrode. The (100)-crystallographic axis was pointing towards the electrolyte and polished to a roughness smaller than 1 nm. A one molar solution of lithium hexafluorophosphate ($LiPF_6$) in ethylene carbonate / dimethyl carbonate (equal volume fraction) was obtained from SigmaAldrich (Battery grade) and used as electrolyte. A porous polypropylene foil (Celgard 2700, thickness of 25 µm) was used as the separator and bought from Reak Wisdom Ltd. Hong Kong. The cell was assembled five days before the experiment in an Argon-filled glovebox (H_20, $O_2 < 5$ ppm). An initial cell resistance of 1.1 Ω was determined just before the start of the experiment.
The experiment was done at the reflectometer D17 at the Institute Laue-Langevin, Grenoble, France. A polychromatic beam was used for the measurements (0.2 nm $\leq \lambda \leq$ 2.5 nm). The cell was charged and discharged galvanostatically with 250 μA corresponding to 10.9 µA/cm^2 followed by three hours of OCV-measurement. At the end of the OCV-period, an impedance-spectra was taken (1 MHz to 0.1 mHz, 10 points per decade, 5 mV rms excitation signal). A single incident angle of 0.8° was chosen for the reflectometry measurements during galvanostatic cell operation (operando-scans). Therefore, the corresponding scattering vector q_z ranges from 0.07 to 0.8 nm^{-1} with a time resolution of 5 minutes. During OCV-periods, a second angle of 3.6° was used to enlarge the range of the probed scattering vector q_z up to 3.8 nm^{-1}. The lithiation was stopped if a voltage of 0.1 V

was reached or the obtained operando-scans became stationary. The delithiation was stopped at a cutoff-voltage of 2.9 V.

The impedance data were modeled using an inductive coil and a solution resistance in series with a distribution of relaxation times. The equivalent circuit is shown in figure 3.1. The inductive part was determined by a linear fit on the high frequency end of the impedance data. Afterward, the ZHiT-algorithm [62] was used to remove artifacts from the spectra caused by a drift of the system during the data acquisition. A custom-made script was used to fit the solution resistance and the distribution of relaxation times to the data. The script is published [85]. A description can be found in chapter 2.6.1. The resulting distribution of relaxation times was separated into fast and slow relaxation processes (relaxation time τ smaller and bigger than 1.5 s, respectively).

Chapter 4

Morphological changes of crystalline silicon electrodes: visualizing macroscopic changes with *operando* phase-contrast radiography

Parts of this chapter were also published as peer-reviewed research paper: Morphological evolution of a single crystal silicon battery electrode during lithiation and delithiation: An operando phase-contrast imaging study, DOI:10.1016/j.ensm.2020.06.007 [54].

4.1 Introduction

Silicon electrodes have a tenfold higher specific capacity than graphite electrodes, but suffer from a strong capacity fading. One reason for the capacity fading was studied in the previous chapter, which elucidated the lithiation mechanism on the nanoscale. Special emphasis was put on the formation of different layers and the influence of the solid-electrolyte-interphase layer, which is one aging-phenomenon. The macroscale will be studied now to get insights into another aging-related phenomenon: the fracturization of silicon electrodes during the lithiation process.
The fracturization is caused by the silicon's brittle nature and the volume expansion of up to 350 % during cycling [3, 18, 22]. McDowell *et al.* and Liu *et al.* employed in-situ transmission electron microscopy to study the lithiation-induced expansion of silicon particles [31, 111]. They observed the fracturization of individual particles, but only for particles larger than 150 nm. A theoretical work by Ma *et al.* confirmed these findings for spheres and gave other numbers for nanowires and thin films [32]. Other morphologies were studied as well with electron microscopy, such as nanowires or porous structures [36, 112, 113]. Similar observations were also made on micron-sized particles using radiography and tomography [114–120]. Here the volume expansion of the individual particles was determined. Combined X-ray and neutron radiography showed an inhomogeneous lithium

distribution within the composite electrode [119]. Electrode degradation was observed, caused by delamination [115, 118, 120] and the formation of porosity within the electrode [120]. A mechanistic understanding of the lithiation process is hard to achieve due to the complex interplay between binder, conductive agent, and silicon particles.

In contrast to particle-based electrodes, single crystalline silicon is well-defined can be used without further additives and therefore serves as a model electrode. However, single crystal silicon electrodes experienced much less research attention than particle-based electrodes. Chon *et al.* measured the voltage-stress relationship, whereas Jana *et al.* determined the residual stress within the silicon crystal after several cycles [121, 122]. The fracturization of single-crystal electrodes was studied by Shi *et al.* using *ex-situ* electron microscopy [48]. A rectangular crack pattern was found after several cycles. However, the dependency of the fractures on the lithiation degree and their evolution over several cycles is still hardly understood. Here *operando*-studies are necessary to elucidate the evolution of these fractures.

Such an *operando*-study is presented here. *Operando* phase-contrast X-ray imaging (PCI) was performed to understand the cracking process more in detail (fig. 4.1). Due to its high sensitivity to material interfaces, PCI is well-suited to visualize cracks within the silicon electrode. Furthermore, the *operando*-mode allows us to track the growth and shrinkage of the cracks within the same cell over several cycles. A voltage-controlled cell operation promotes the formation of different lithium silicon equilibrium phases, which only occur at voltages smaller than 70 mV [27, 28]. Additional information was obtained from a multidimensional characterization of the sample. *Ex-situ* focussed ion beam scanning electron microscopy (FIB/SEM) was used to assign the observed morphology changes to the specific electrode since the obtained radiograms contain the superposition of both

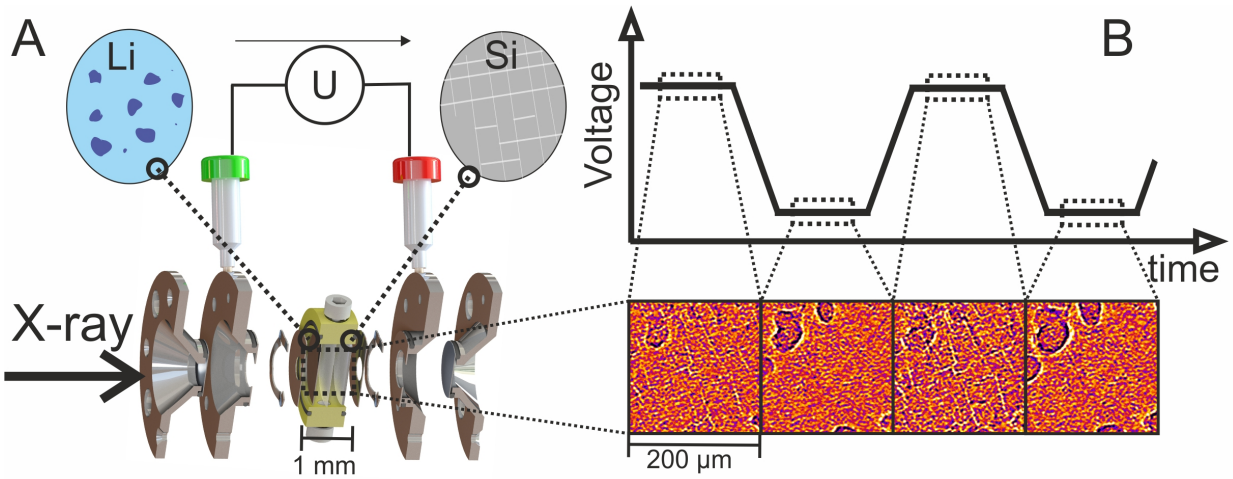

Figure 4.1: Schematic overview of the experiment. The employed cell is shown in the left part of the picture (A). Lithium and silicon serve as electrodes. The lithium experiences a pitting process during lithiation, whereas a rectangular fracture pattern is formed on the silicon wafer during delithiation. The resulting radiograms can be seen in the right part of the image (B), their corresponding voltage is indicated in the upper part. Taken from [54]

electrodes. *In-situ* electrochemical impedance spectroscopy (EIS) was used to obtain information about the cell's electrochemical properties. *Ex-situ* Laue-diffraction determined the direction of the crystallographic axis of the silicon relative to the cracks.
The cell's electrochemical behavior will be discussed in the beginning and compared to previous results to prove the absence of cell-related artifacts. Afterward, the *operando*-phase contrast radiography results will be handled in two steps: First, a single cycle will be discussed, followed by the evolution over all cycles. The last part contains the discussion of the *ex-situ* measurements. Therefore, mechanistic insights into the fracturing of silicon (100) electrode are provided.

4.2 Analysis of electrochemical measurements

The electrochemical data are summarized in figure 4.2. Part A shows the time dependency of the voltage (dotted black line) and the current (solid red line), whereas part B shows the voltage-current relationship. The bar-plot in part C illustrates the cycle-dependency of the capacity during lithiation and delithiation. The difference is written within the plot and denotes the amount of charge lost in parasitic side reactions and irreversible lithium trapping.

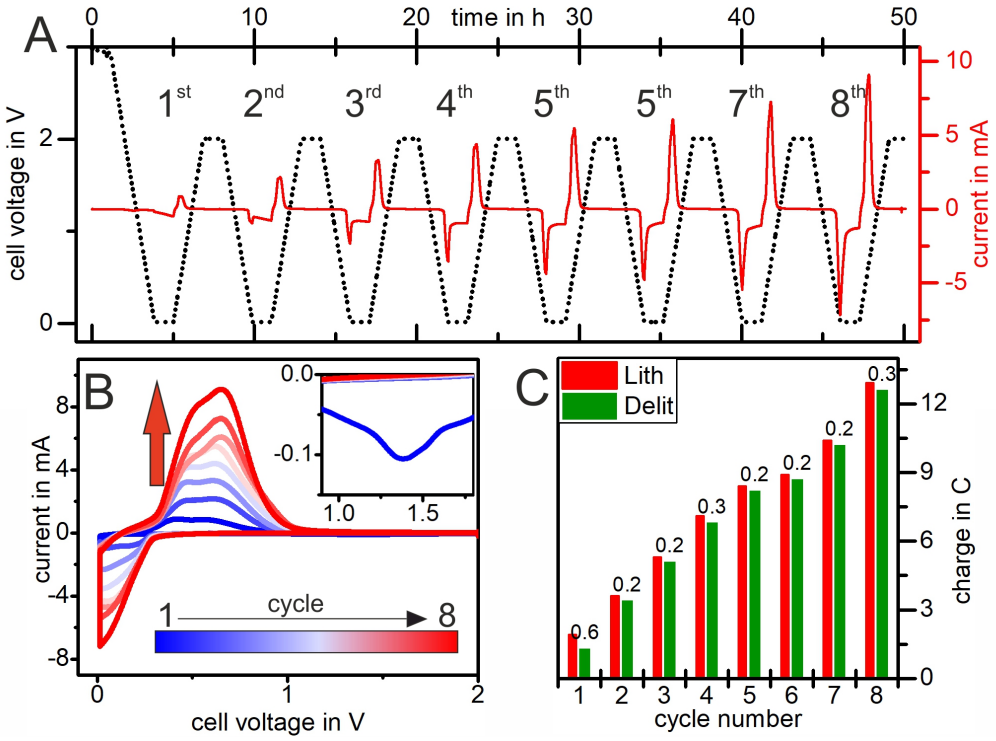

Figure 4.2: Electrochemical results of the *operando* imaging experiment. Part A: the voltage (dashed black line) and the current (solid red line) are shown over the experimental time. Clearly, an increase in the current can be found. Part B: Measured current over the cell voltage. The inset is a magnification of the curve between 1.0 and 1.5 V. Part C: Charge flown during lithiation (red) and delithiation (green). The difference between both quantities is denoted on top of the bars. Reproduced from [54]

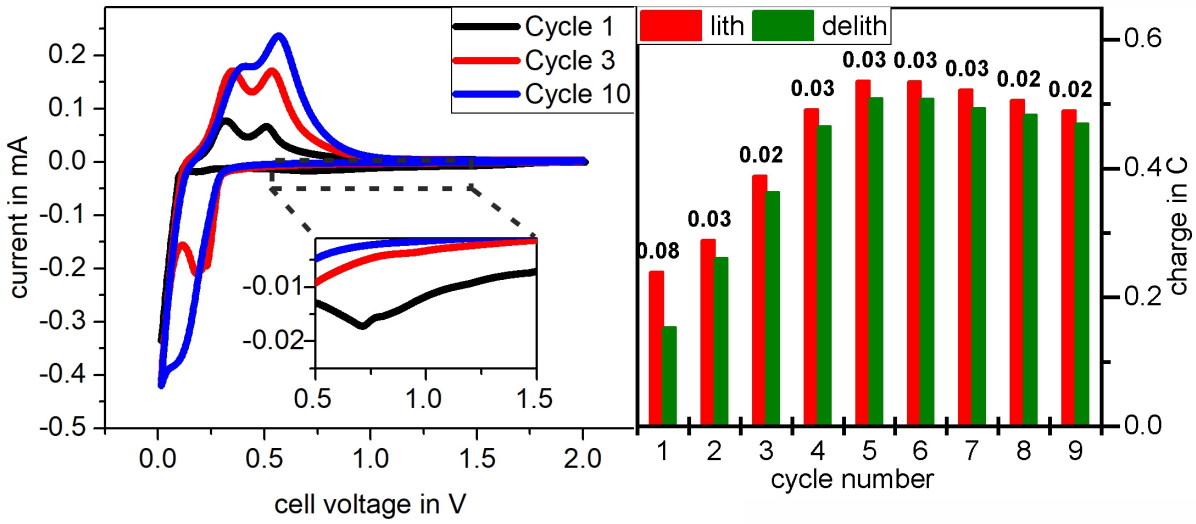

Figure 4.3: Left: Cyclic voltammetry of a coin cell. Similar electrodes, the same electrolyte and separator as in fig. 4.2 are employed. The cyclic voltammetry of the first, third and tenth cycle is shown. The inset is a magnification of the small peak around 0.7 V. Right: Charge flow during lithiation (red) and delithiation(green). The difference of both is the charge loss and is written on top of the bars.

A cyclic increase of the current is observed, caused by the successive increase of the electrochemically active silicon [3, 48]. During lithiation, crystalline silicon forms an amorphous alloy with silicon. After delithiation, the silicon stays in the amorphous phase [28], which gets lithiated already at higher voltages ($\approx$ 300 mV) [28, 29]. Afterward, the underlying crystalline silicon takes part in the lithiation process, causing the stepwise increase of active material. Only the first cycle exhibits a cathodic peak around 1.4 V. Therefore, this feature is associated with the lithiation of the native silicon oxide layer and the removal of an initial SEI-layer [49, 53, 123]. The decomposition of impurities also creates side peaks, as shown by Kawaguchi *et al.* and Freiberg *et al.* [124, 125]. This peaks shift towards lower voltages in the coin cell (fig. 4.3, inset).
Two anodic peaks can be found around 0.4 and 0.6V, which indicate the dissolution of the different lithiated silicon phases [3, 48, 126]. A slight shift of the peaks to higher voltages with increasing cycle number is observed. Both peaks are comparable in height up to the third cycle. Afterward, the second peak around 0.6 V becomes larger than the first peak. A similar behavior was found by Shi *et al.* [48]. Also offline-cycling of a coin cell reveals comparable results (figure 4.3). Different processes may be involved here. A voltage-shift of the peaks caused by an overpotential could lead to a larger overlap of both peaks. Also, a higher fraction of charge in the lowly-lithiated phase could be caused by an incomplete formation of the highly-lithiated phase during lithiation. Therefore, the lowly-lithiated phase still exists at the end of the lithiation, increasing the relative amount of charge stored within this lithium-silicon species. This may originate from a diffusion-limited charge transport, which was described already in the literature [48, 109]. No offset-current and no additional side peaks can be found except the small peak at 1.4 V in the first cycle. An irreversible

charge loss of 0.2 C from the second cycle on can be observed in the *operando*-cell, which originates from the reformation of the SEI-layer [49, 51, 92] and lithium trapping [107, 108]. This was found already in chapter 3.
The coin cell also shows an increased charge loss in the first cycle, whereas the subsequent cycles show a constant charge loss. The total value is approximately one order of magnitude smaller, but also the charge flow is by a factor of 20 lower. Therefore, the Coulombic efficiency of the *operando*-cell is even higher than the coin cell's efficiency. All important electrochemical data of the lithiation/delithiation process are present, no significant side reactions can be observed [3]. The results of the *operando* PCI can be related directly to the electrochemical processes.

4.3 Analysis of the morphology changes

Now the results of the *operando*-imaging will be discussed and related to the electrochemical performance. The acquired radiograms are a superposition of both electrodes and also the separator. The cell was disassembled after the experiment and analyzed using FIB/SEM to assign the morphology changes to the specific electrode. The observed crack pattern (bright lines within the radiograms) is located on the silicon electrode, whereas circular structures originate from the lithium electrode and show a lithium pitting process [127]. No morphological changes were observed on the separator. Shi *et al.* reported similar observations [48]. First, a single cycle will be discussed to elucidate the morphological changes within a cycle. Afterward, the evolution over the whole experimental time will be analyzed. The last cycle is taken as an example since the morphological changes are most pronounced here. A video file showing all obtained radiograms is also available.
The left part of figure 4.4 shows the obtained crack intensity together with the electrochemical results. The dashed lines indicate the beginning of the morphology change. Four different positions

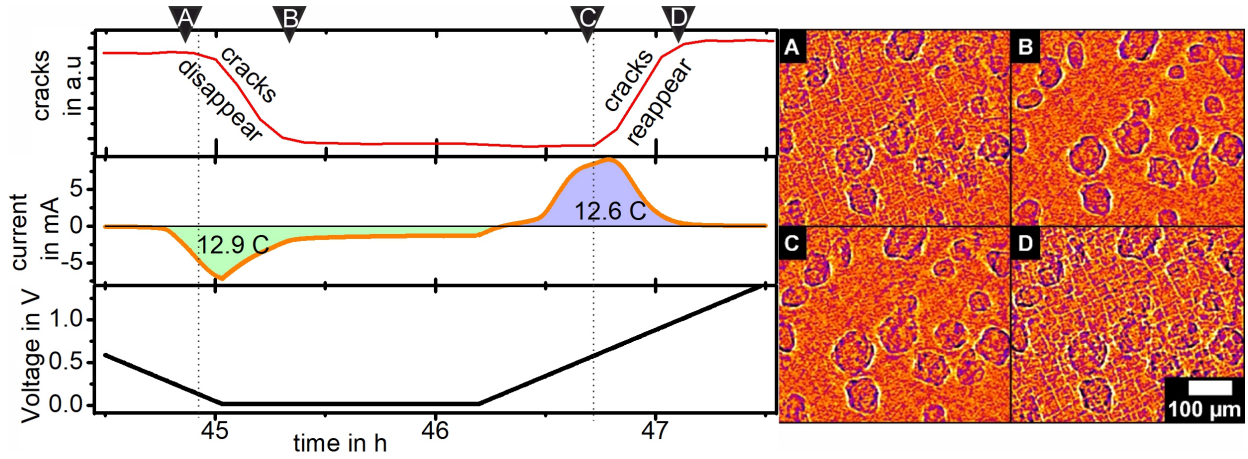

Figure 4.4: Morphology change in the last cycle, together with the electrochemical data. The crack intensity is drawn on the top in the left part, followed by the current (middle) and the voltage (bottom). Four positions are marked with letters A to D. The corresponding radiograms are shown on the right. Reproduced from [54]

are marked with A - D. The corresponding radiograms can be found on the right part. In total, a charge of 12.9 C was stored within the silicon. Picture A shows the initial status of the electrodes. Clearly, a rectangular crack pattern can be found. Note that lithiation started already, and a small fraction of lithium is already introduced into the silicon since the voltage reached ≈ 250 mV. The cracks start to vanish once the voltage is decreased to 15 mV and the potentiostatic step starts. This promotes the formation of the highly lithiated species [3, 28, 128]. Figure B shows the electrodes after crack closure (roughly 30 min after A). The volume expansion associated with the lithiation of silicon closes the cracks [20, 34, 35, 90]. All cracks seem to vanish simultaneously, indicating an isotropic expansion within the surface plane due to the silicon electrode's limited space. This is contrary to observations published elsewhere [36, 37]. The voltage of approx. 15 mV indicates the formation of the highly lithiated silicon phase during crack closing. However, no peak in the current was observed here, which could act as a fingerprint for the formation of this equilibrium phase.
Picture C shows the morphology before the cracks start to reappear. Note that picture C was acquired within the delithiation in the middle of the two anodic peaks at ≈ 520 and ≈ 660 mV. Approximately 5.3 C were removed already from the silicon. In between, circular structures grow within the observation area. This feature originates from lithium pitting [127]. Picture D is taken after the cracks reappear. The time difference between pictures C and D is roughly 25 min. The cracks observed already in picture A can be found again in picture D, but more pronounced. Also, additional cracks can be found. The crack pattern seems to expand over the whole electrode. The fractures direction is in line with the crystallographic axis of the underlying silicon crystal, which was shown by Laue diffraction (see also fig. 4.9). Capacity-limited cycling may suppress the electrode fracturization, which was suggested already by Obrovac *et al.* [29].
Now the cycle-dependent morphology change will be discussed. which figure 4.5 shows. Part A and B show the voltage and current of the system, respectively. Part C shows the crack intensity, which was obtained from the radiograms. Part D shows the results of the impedance analysis, which was performed at the end of the potentiostatic steps. All parts share the experimental time as the x-axis.
As mentioned already, a cyclic increase in the peak current is observed, which was related to the increase of electrochemically active material. The crack intensity also shows a cyclewise increase, starting in the third cycle. The shallow increase at the end of the first cycle arises from a surface restructuring. The charge state dependent growth and shrinkage of the fractures is observed from the fourth cycle on. The fractures increase the electrode's surface area and decrease the path length from the bulk silicon to the electrolyte. Therefore, the diffusion of lithium into the electrolyte is enhanced, which could explain the relative growth of the high voltage anodic peak from the fourth cycle on (see also fig. 4.2). The change in the crack intensity is quite steep, indicating a fast morphology change. A typical time scale is approx. 30 minutes. The amplitude of the change increases with cyclenumber, indicating the contrast increase of the crack intensity and the expansion of the crack pattern over the silicon electrode again. The intensity increase can be caused either by a widening or by a deepening of the cracks. Unfortunately, both effects cannot be distinguished due to the limited experimental resolution. No inactive spots on the electrodes were observed during

the *operando* imaging experiment, even though the expansion of the fractures may cause mechanical aging of the electrode. The irreversible charge loss of roughly 0.2 C per cycle, which is shown in fig.

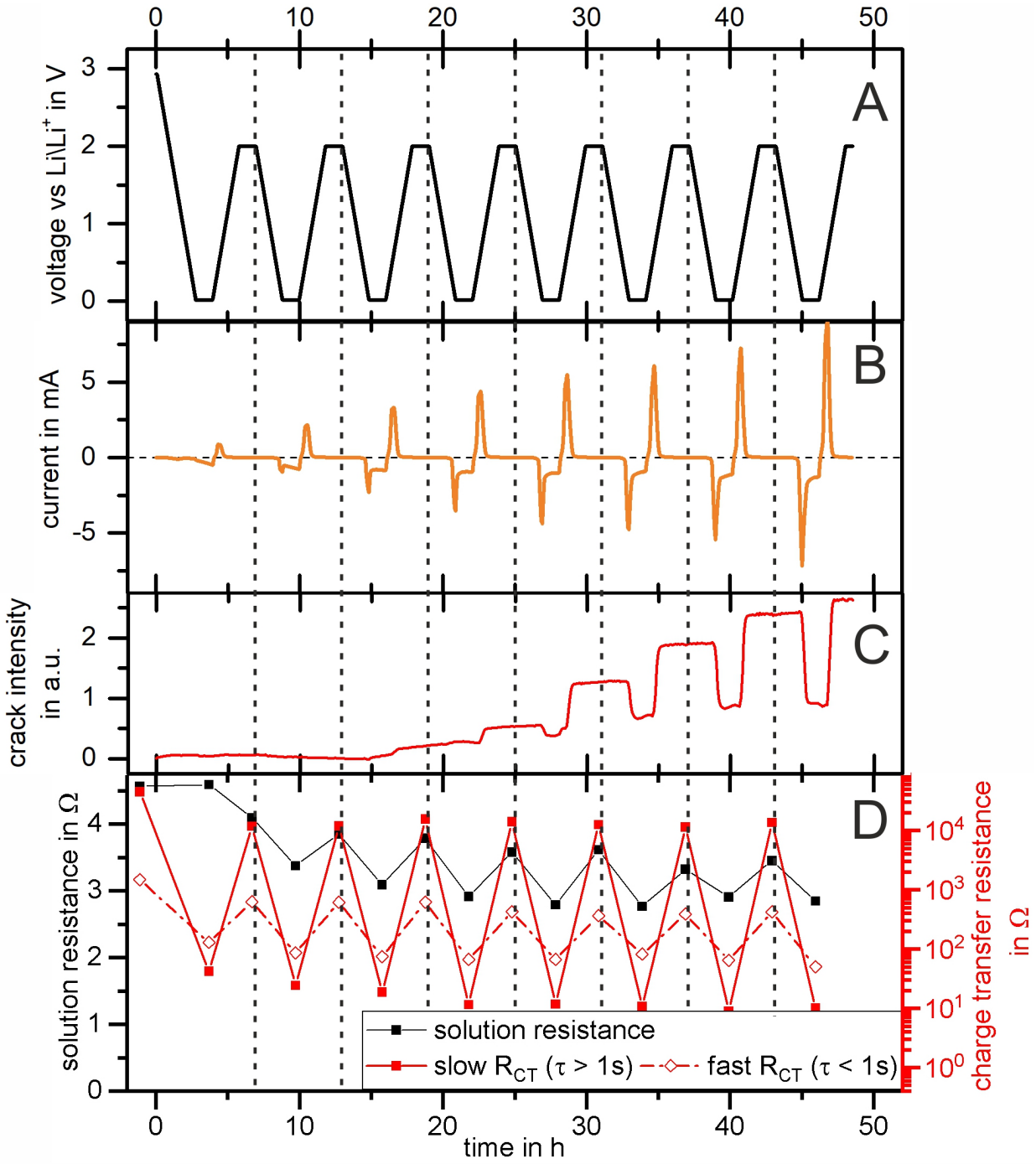

Figure 4.5: Overview of the obtained results from radiography and electrochemistry. Part A: cell voltage. Part B: current of the cell. Part C: Crack intensity calculated from the obtained radiograms. The increase of the crack intensity indicates the growth of fractures within the field of view. Part D: obtained results from the EIS. Taken from [54]

4.2, is therefore caused by side reactions associated with the SEI-layer [49, 51, 92].
The results of the impedance spectroscopy are shown in part D. The Nyquist plots can be found in fig. 4.6. First, the spectra were corrected for artifacts that arise from a drift of the system during measurement time [62], then a linear fit at high frequencies determined the inductive part of the impedance caused by wires (see also chapter 2.6.1). Afterward, an equivalent circuit consisting of a resistor and a distribution of relaxation times (DRT) in series was used to model the electrochemical behavior, as already done in chapter 3. The DRT-element consists of several capacitors and resistances in parallel and models charge transfer processes. The complete algorithm is described elsewhere [85].
The distribution of relaxation times was split into fast relaxations ($\tau < 1$ s) and slow relaxation processes ($\tau > 1$ s). In similar systems, the fast relaxation processes were assigned to the metallic

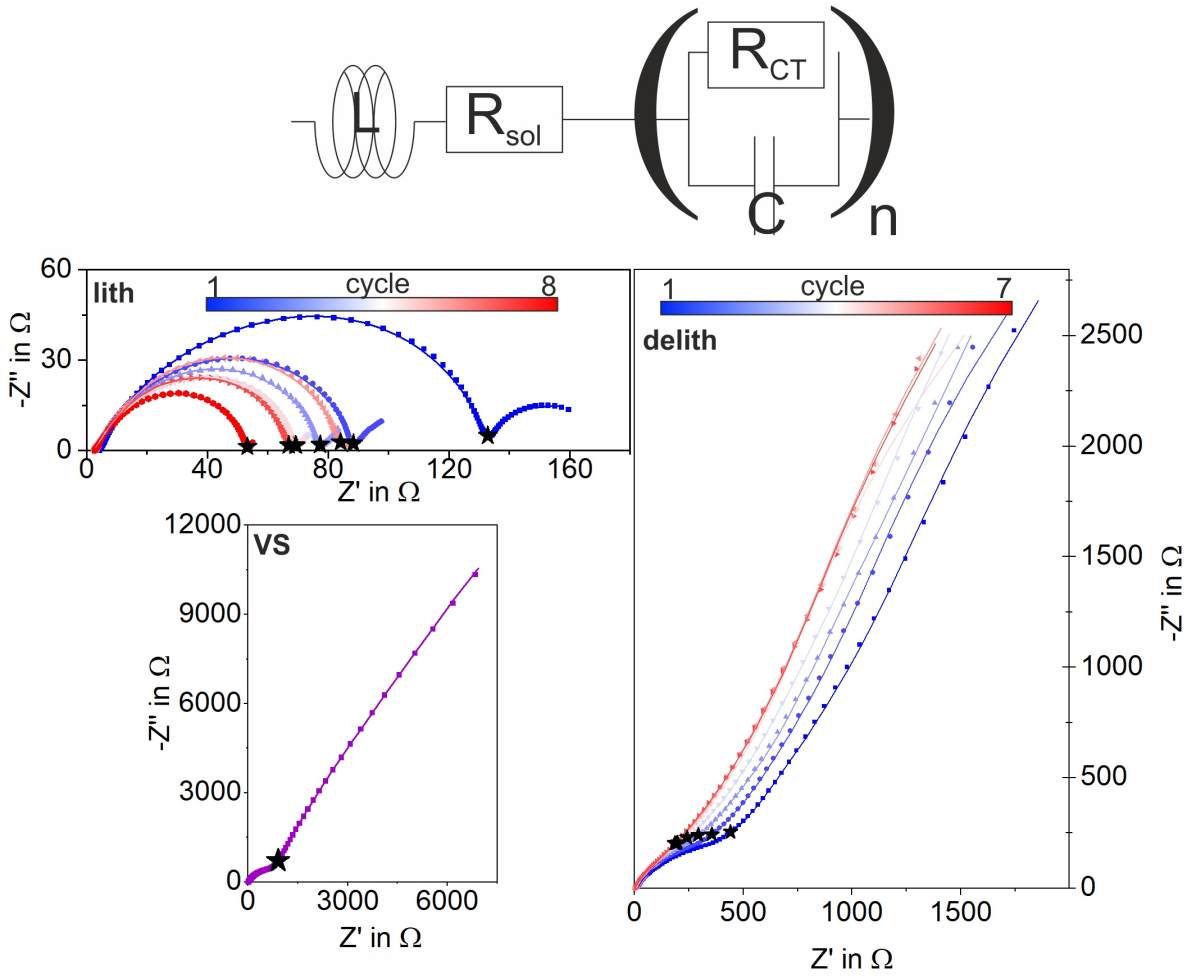

Figure 4.6: Nyquist plots of the experiment. The employed equivalent circle is shown on top of the Nyquist plots. Due to the large difference in the impedance values, the results are split into the virgin state (bottom left), the delithiated state (on the right), and the lithiated state (top left). The star indicates a frequency of 1 Hz. Reproduced from the supporting information of [54]

lithium electrode [85, 129, 130]. The delithiated state exhibits an increased charge transfer resistance for both time scales. The lithiated states show a facilitated charge transfer, although the surface area is larger in the delithiated state. Therefore, a charge transfer inhibiting layer counteracts the increased surface area, which was shown in the previous chapter. The amplitude of the charge transfer resistances is larger for the slow processes. Also, the solution resistance R_{sol} shows an alternating behavior. Here two processes are involved, the charge-state dependent conductivity of silicon and the morphology change of the SEI-layer on the electrodes, as shown in the previous

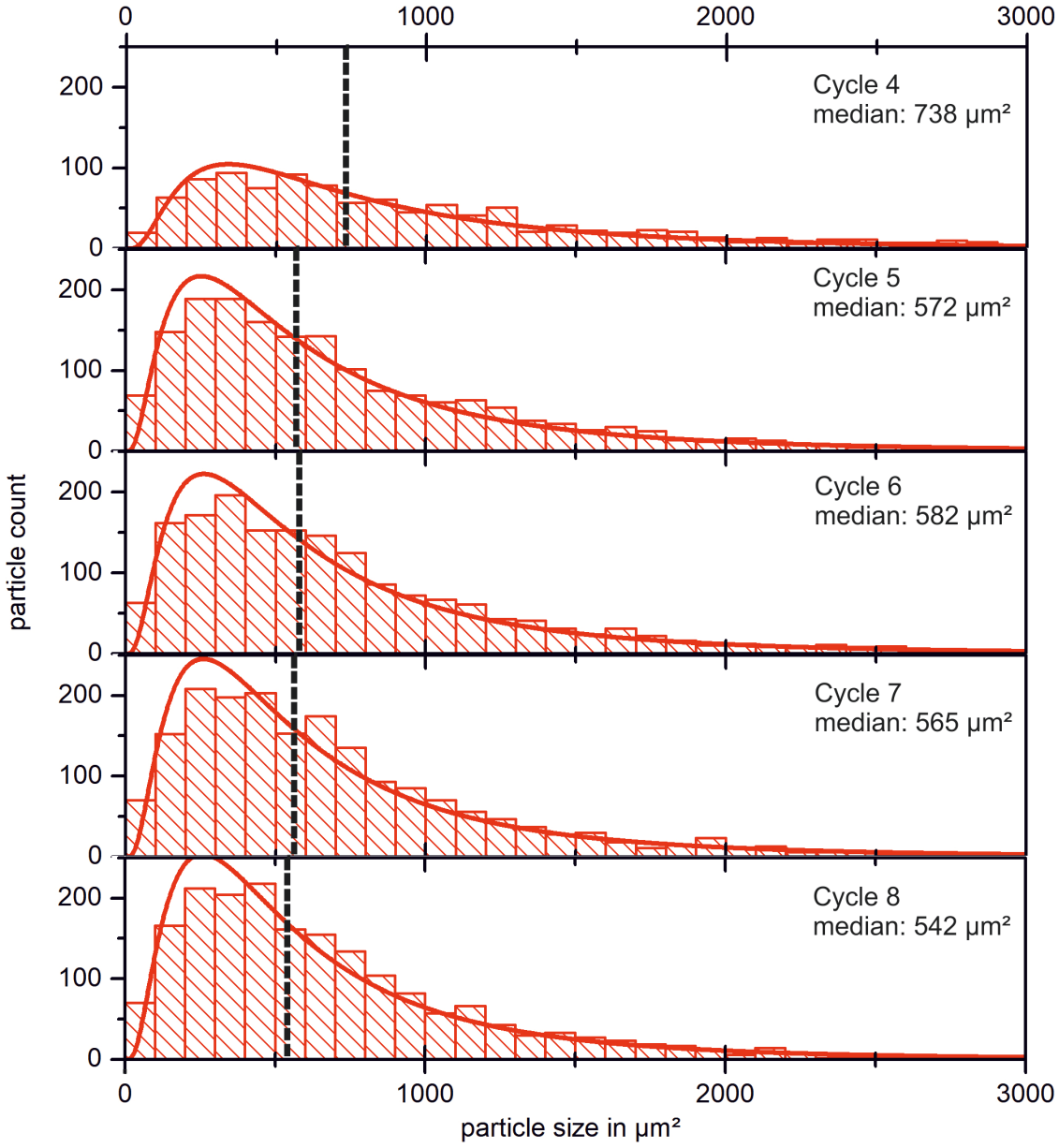

Figure 4.7: Size analysis of the crack patches for the last five cycles. Patches larger than 3000 µm² were handled as uncracked and therefore removed. The dashed line indicates the median patch size of each individual distribution. Reproduced from [54]

chapter [53, 95]. The lower values are obtained in the lithiated state. In previous results, lower values of the solution resistance R_{sol} were obtained in the delithiated state. Therefore, the much thicker lithiated zone has a larger impact on the resistance than the additional SEI-layer, which forms in the delithiated state. A cell dry-out or an electrolyte decomposition process would cause a continuous increase instead. A charge state dependent conductivity of silicon was also reported elsewhere [95].

Fig. 4.7 shows the area distribution of the crack patches (the area between the fractures) for the 4^{th} to the 8^{th} delithiated state. The analyzed electrode area was $0.9 \cdot 1.3$ mm^2. Areas larger than 3000 µm^2 are handled as uncracked and therefore removed. The total amount of crack patches increases from ≈ 1050 to ≈ 1880 from the 4^{th} to the 8^{th} cycle. The median patch size stays nearly constant from the 5^{th} cycle on, as indicated by the dashed line. The same behavior is found for the first quartile of the distribution (309 µm^2 and 310 µm^2 for the 5^{th} and 8^{th} cycle, respectively). This indicates that the crack pattern does not penetrate the silicon patches. No continuous cracking to smaller patches occurs.

The last cycle was analyzed further to investigate the shape of the patches more in detail. Here, a median length and width of 28.2 and 19.5 µm^2 were found, indicating a rectangular shape of the patches. The ratio between shorter and longer edge is ≈ 1.45. Less than 5 % of the patches are smaller than 11.4 and 7.6 µm^2 in length and width, respectively. The silicon patches' particular morphology may lead to a lithiation-behavior comparable to nanopillars instead of a plane. Also, an anisotropic lithium distribution within the patches may decrease the mechanical pressure within the silicon electrode. With a limited lithiation degree structures larger than 150 nm can be stable upon lithiation [32]. However, *ex-situ* FIB/SEM measurements were used to analyze the sample more in detail since Liu *et al.*, Shi *et al.*, and Dong *et al.* also reported irregular and very narrow cracks [48, 111, 114]. PCI cannot detect these fractures.

4.4 *Ex-situ* microscopy analysis

After 15 cycles, the cell was disassembled in the delithiated state. One half of the silicon wafer was placed within a FIB/SEM for further analysis. The second half was used to perform Laue diffraction measurements. The results of the Laue diffraction prove that the cracks within the silicon are aligned with the crystallographic axis of the silicon wafer. The obtained Laue diffractogram is shown in fig. 4.9. As already discussed, the silicon is transformed into the amorphous phase during the initial stage of lithiation [3, 28]. Therefore, the cracking process starts already before the amorphization since otherwise, no preferred direction exists. This is in line with the findings of Rhodes *et al.*, who found the silicon cracking initiation during the beginning of the lithiation [131]. The results of the FIB/SEM are shown in fig. 4.8. Picture A shows the rectangular crack pattern again from the top. C and D show a cross-section with two different detector settings. Additional, disordered cracks within the silicon patches can be found, which are thinner than the regular crack pattern. These may originate from the deflection of cracks on the interface between amorphous and crystalline silicon, as shown by Shi *et al.* [48].

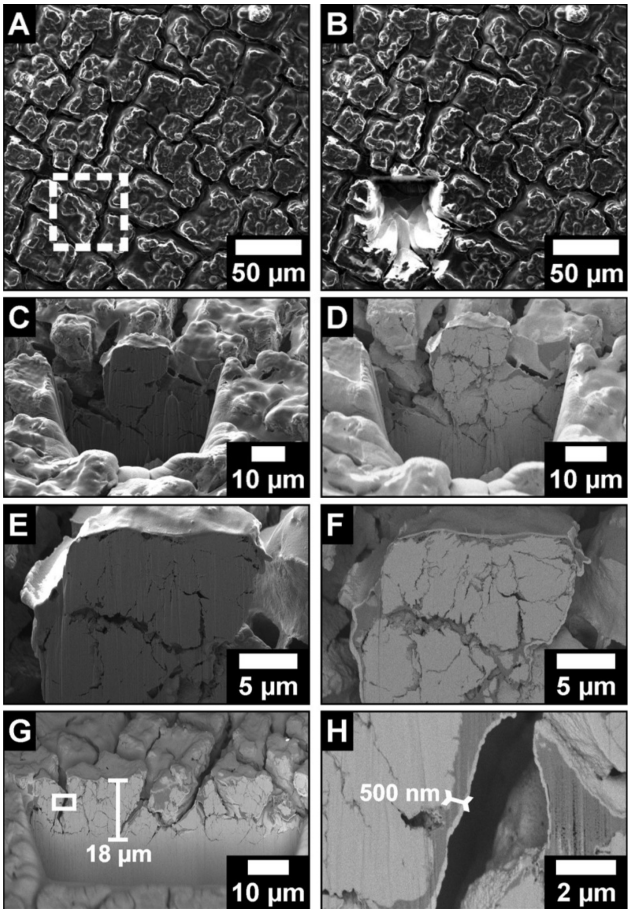

Figure 4.8: *Ex-situ* FIB/SEM images of the silicon electrode after 15 cycles. Part C and D, as well as E and F, show the same spot on the electrode but with a different detector. Reproduced from [54]

The rectangular cracks do not follow the crystallographic axis in the depth direction, which would lead to straight cuts perpendicular to the surface. They also show deviations to the left and right, which might cause electrical disconnection of silicon and loss of active material at higher cycle numbers, causing mechanical aging. Shi *et al.* made comparable observations [48]. The depth of the cracks is approximately 18 µm, which is only a rough estimation for the depth of the lithiated zone. An average lithiation degree of 1.1 lithium atoms per silicon atom can be calculated if an isotropic lithiation is assumed and the thickness of the lithiated zone matches the depth of the cracks. This calculation just serves as a reference and is roughly by a factor of two lower than the values found elsewhere [49–51, 53, 126]. Most probably, an inhomogeneous lithiation of the patches occurs since the obtained electrochemical results showed the formation of the highly lithiated silicon interphases ($Li_{15}Si_4$ and $Li_{22}Si_5$).

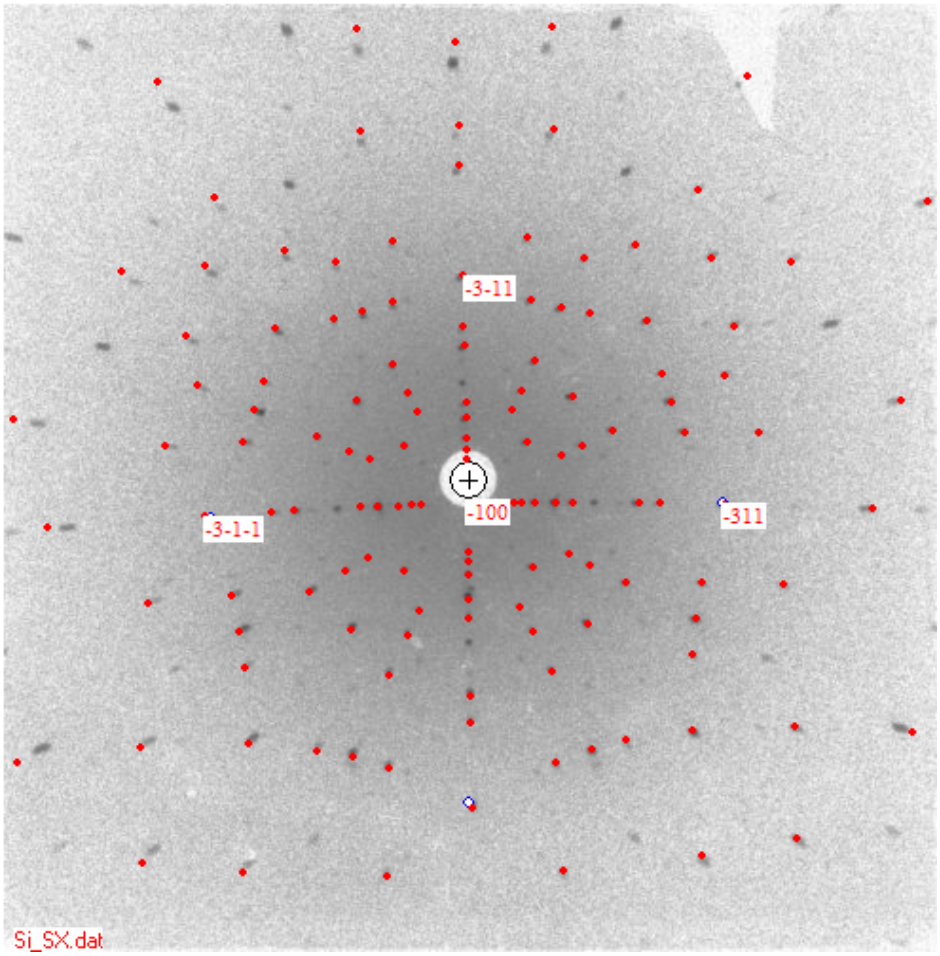

Figure 4.9: *Ex-situ* Laue diffraction image. The black dots are the obtained diffraction peaks, whereas the red dots correspond to the theoretical values of the Si crystal. Reproduced from the supporting material of [54]

4.5 Conclusion

Phase-contrast imaging was employed to visualize the lithium silicon cell's morphological changes over several cycles under operando conditions. A voltage-dependent crack pattern was observed and assigned to the silicon electrode. This pattern is aligned with the crystallographic axes of the crystalline silicon (100) wafer and forms within the delithiation after depletion of the highly lithiated phase. During lithiation, the observed fractures vanish when the highly lithiated phase is formed again, most likely due to the volume expansion of silicon. The fracturization pattern is fixed in its position, meaning, once a specific area is fractured, cracks can be found in precisely the same position again. This indicates, the cracks close during lithiation, but no connection is reestablished. Besides, adjacent or new areas on the silicon get fractured and the pattern expands over the whole observation area but does not penetrate the individual crack patches.
The size distribution of the crack patches stays nearly constant. Although the number of identified

patches increases, the median area stays constant and is around 560 µm^2. Further analysis reveals a rectangular shape of the patches. Less than 5% of the patches are smaller than 6 and 9 µm in width and length, respectively. The individual silicon patches do not decompose to smaller particles. Nevertheless, even if no electrode failure or inactive areas were observed, the fractures' continuous growth may decrease the electrode performance at higher cycle numbers.

4.6 Experimental details

Imaging measurements were done at the BAMline station at BESSY II [83]. The phase-contrast mode was enabled by the use of monochromatic, coherent, and parallel incoming X-rays. The sample-detector-distance was set to 40 cm, which allows the phase-contrast to develop [79]. A beam energy of 25 KeV was chosen. A scintillator converts the X-rays and consists of a $CdWO_4$ layer with a thickness of 60 µm, an optical peter lens system with magnification of 20 together with a PCO.4000 camera (PCO AG) records the signal. This setup results in a field of view of 1.75 x 1.17 mm^2 and a pixel size of 0.437 µm. Every frame was exposed to the incoming radiation for 60 s, followed by a flat field measurement for 60 s. This results in a time resolution of approx. 140 s since the sample is moved out of the beam for flatfield measurements. The total imaging time was about 48 h.

Technical difficulties led to a break in the image acquisition after approx. 20 h for one hour. The cell was not stopped during this time. The missing 25 images were added via interpolation. In total 1220, radiographic images were acquired, consisting of a superposition of all cell parts, especially the two electrodes, lithium and silicon. Fig. 4.10 shows a sketch of the setup. The occurrence of phase boundaries creates an intensity pattern on the detector through the refraction of the X-rays. The operando cell is sketched in fig. 4.1. It consists of stainless steel electrodes, a PEEK-body, and aluminum windows. A detailed description can be found in chapter 2.5. A single-crystalline silicon disc(100, n-doped, 500 µm thickness, 16mm diameter, specific resistivity 10^{-3} to 40 Ω cm, purchased from Sigma Aldrich) and a metallic lithium sheet were used as electrodes. 1 M $LiPF_6$ dissolved in ethylene carbonate/dimethyl carbonate (1:1 by volume) was used as the electrolyte (Sigma Aldrich, battery-grade purity). Celgard 2700 (porous polymer foil, 25 µm thickness) was used as a separator. All cell parts and the silicon electrode were cleaned in 2-propanol (99.8%, H_2O < 0.1 %, Sigma Aldrich) before use. The cell was assembled in an Ar-filled glovebox. An initial cell resistance of 4.5 Ω was determined. The transmittance of the cell for 25 keV X-rays was roughly 50 %.

The image processing was done using the software Fiji/ImageJ [132] and is also described in chapter 2.4.1. The sample movement for flat field acquisition results in a small positional error, which was corrected by the Scale-Invariant-Feature-Transform method [81]. Horizontal stripes within the images arise from the monochromator movement and were removed by a wavelet-based stripe filter [82]. Figure 2.15 summarizes the correction procedure. All electrochemical measurements were done using a GAMRY Interface 1000 potentiostat. Initial EIS was carried out under OCV-

conditions (2.98 V vs. Li/Li^+). A frequency range of 1 MHz to 100 mHz was probed with 15 points per decade. A voltage amplitude of 5 mV (rms) was used. After the initial EIS, an 1 h OCV-measurement was performed. Here the wetting process of the electrode took place and the X-ray instrument was calibrated. A linear voltage sweep (0.3 mV/s, down to 15 mV) was performed afterward, followed by a potentiostatic hold at 15 mV for 1h and an EIS at this voltage. Afterward, a voltage sweep to 2.0 V was performed, followed by a potentiostatic hold and an EIS at 2.0 V. This procedure was repeated to cycle the cell. The impedance data were analyzed using the model shown in fig. 4.6. The evaluation of the impedance data is described in detail in chapter 2.6.1 and is based on a custom-made Mathematica script [85]. Prior to analysis, the ZHiT-algorithm was applied, which was described in chapter 2.6.1 [62].

The images were corrected and analyzed to get a quantitative view of the observed phenomena (see chapter 2.4.1 for further details). All images were divided by the median of the first 10 images. This results in an increased contrast within the other images. A subseries of images with a highly pronounced crack pattern was chosen (at 23 h, 29 h, 35 h, 41 h, and 47 h). Here it was possible to identify the crack positions via threshold discrimination on the mean of the subseries. The result serves as a mask to identify the crack regions. This mask was applied to all images. The intensity within the masked area was summarized and represents the crack intensity. For the final states of the 4^{th} to 8^{th} delithiation, the size distribution of the was determined using a random forest classifier [133]. The mask used already used to calculate the crack intensity was employed to generate the ground truth manually. 0.3% of the whole dataset was used to train the classifier. In total, 200 decision trees were trained, and a ten-fold cross-validation was used. The classifier

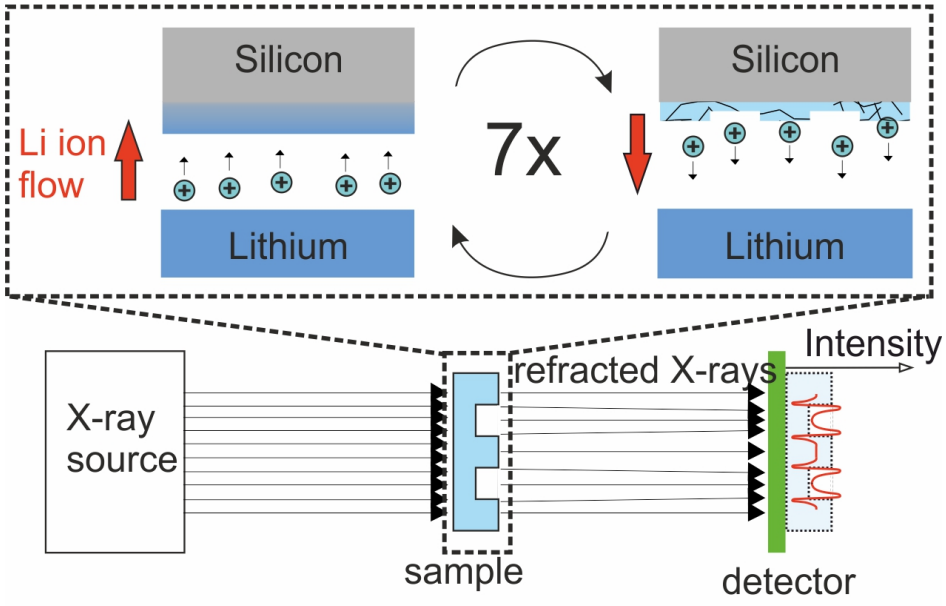

Figure 4.10: Scheme of the experiment. Coherent and parallel X-rays are radiated on the sample. Interfaces within the morphology refract the X-rays, leading to the creation of peak-dip pairs in the intensity. The morphology changes arise from the lithiation process, which causes fractures within the silicon.

returned a probability map of the crack distribution on the images. A watershed was applied on the probability map to generate the cycle-dependent crack pattern and the size distribution.
For further *ex-situ* analysis, the sample was disassembled in an Argon-filled glovebox (H_2O, O_2 $<$ 1 ppm) and dried under vacuum at elevated temperatures. No solvent rinsing was applied not to destroy the sample surface morphology. During this procedure, the silicon wafer broke due to the brittle nature of silicon. The sample was sealed in a specialized, airtight sample shipper to minimize the air exposure during the transfer to the microscope. A short exposure was unavoidable while placing the sample into the sample chamber (roughly 15 s). A ZEISS crossbeam 340 equipped with a Gemini I electron gun and a Gallium ion source was used. The electron gun and Gallium source are located at an angle 54°. A two-step procedure was used to cut the sample surface: First, the Gallium ions were used with a current of 15 nA and 30 kV to remove material from the silicon. Afterward, the electron beam was used for fine polishing at a current of 300 pA and 30 kV. The SE2-Detector and the InLens BSE detector with a low electron acceleration voltage of 1 kV have been used to scan the milled sample surfaces. Isotropic spatial dimensions were achieved by a scanning angle of 36°. *Ex-Situ* Laue diffraction was done with an in-house build Laue camera, which employs a tungsten X-ray tube operating at 25 kV. During sample preparation, the silicon electrode broke. The angle between the breaking edge and the original orientation was determined. The sample was glued on a sample holder with the breaking edge in a horizontal orientation. The data was recorded on an image plate (12 x 12 cm^2) and scanned afterward with a pixel size of 100 µm. 'OrientExpress' was used as analysis software for the Laue-image.

Chapter 5

Influence of an artificial coating on crystalline silicon on the lithiation studied by *operando* neutron reflectometry

5.1 Introduction

Silicon electrodes suffer from a pronounced capacity fading associated with the large volume expansion during lithium uptake [3, 18, 21]. Two different aging phenomena of silicon electrodes were studied in the previous chapters using different *operando*-techniques. This allows us to reveal the processes within the cell during operation.
The formation of an inhibiting SEI-layer on a crystalline silicon electrode was studied in chapter 3 and the associated publication [53]. This SEI-layer causes a voltage plateau at voltages > 1 V, indicating side reactions [3, 92]. The layer needs to be dissolved before the lithiation takes place. Comparable observations were made by Seidlhofer *et al.* [50]. Chapter 4 deals with the fracturization of silicon. Similar to the results of Shi et al. [48], an orthogonal crack pattern was found. Our *operando* study allows us to observe the formation of the fractures, which vanishes during lithiation and reappears during the second half of the delithiation [54]. Both effects are detrimental to the cell capacity and shall be avoided [3, 18, 21]. Different strategies were developed to suppress the aging in silicon electrodes, such as the use of additives to the electrolyte [5, 11] or advanced morphologies [18, 22, 23]. However, also additives used in the electrolyte get consumed [46], and advanced morphologies can suppress electrode fracturization, but the increased surface area may increase the SEI-layer formation[40]. Furthermore, advanced morphologies may exhibit a lower mass loading density [22].
Another strategy to suppress aging effects is using an artificial SEI [9, 44]. Here a thin layer is deposited on the electrode's surface, which prevents direct contact between the electrolyte and the

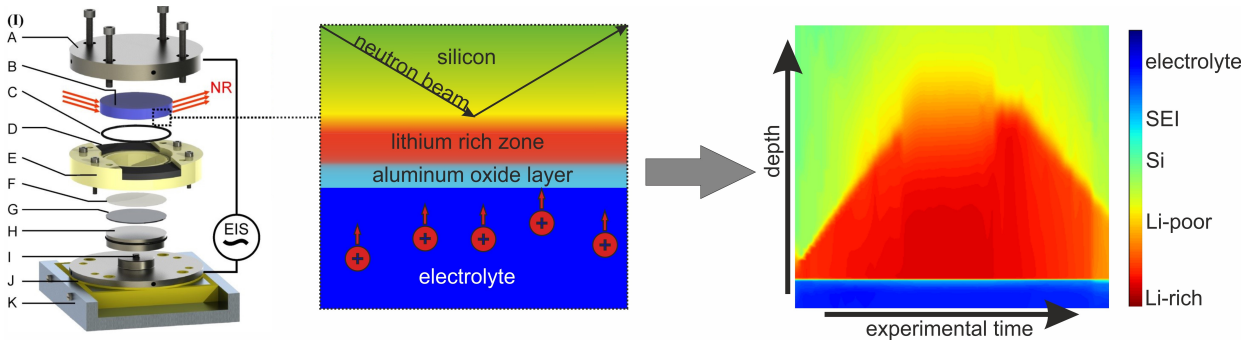

Figure 5.1: On the left: Scheme of the *operando*-cell used for the neutron measurements done in this chapter. The cell is described more in detail in chapter 2.5. In the middle: Scheme of the investigated region. Lithium is electrochemically introduced and extracted from silicon. A neutron beam impinges from the top through the silicon substrate. Interfaces within the electrode reflect the neutron beam. A protective layer (aluminum oxide) was deposited on top of the silicon electrode to investigate its influence on the electrochemical performance. On the right: resulting SLD profile of the first cycle. The growth of the lithiated layer during lithiation can be observed.

silicon. Furthermore, the artificial SEI-layer's mechanical stability can mediate the stress evolution and therefore hinder the fracturization [11]. A variety of different materials was used to form artificial SEI-layers on electrodes, such as aluminum oxide [43, 134, 135], titanium oxide[42, 136], LIPON[44, 137], and many more [9, 11, 138]. However, introducing an additional layer may influence the lithiation process and create an additional bottleneck for the ion conduction. A detailed understanding of the related processes necessary for further improving silicon electrodes. *Operando*-studies are therefore necessary to extend our knowledge.

A single crystalline silicon wafer is used as a model system for the lithiation process. Aluminum oxide is used as artificial SEI-layer and is a commonly used protective coating[43, 45, 134, 135, 139]. The lithiation process was investigated using neutron reflectometry since this technique can probe buried interfaces and lithium and aluminum oxide exhibit a high scattering length density contrast [66].

First, the aluminum oxide coating morphology will be analyzed using X-ray reflectivity and neutron reflectivity. Afterward, its electrochemical influence will be compared to the uncoated electrode in a coin cell. Here electrochemical cycling and EIS are used. The discussion of the *operando*-neutron reflectometry results will provide insights into the morphology change during lithium insertion. A conclusion is given at the end of the chapter, together with the experimental details.

5.2 Analyis of the deposited layer

The layer was formed by depositing aluminum on the clean silicon wafer under vacuum. The native silicon oxide was not removed. 3 nm of aluminum was deposited on the silicon wafer and oxidized in air, forming aluminum oxide AlO_x. The pre-characterization of the coated silicon wafer using X-ray reflectivity as well ass the virgin state of the neutron reflectometry can be found in fig. 5.2. Two

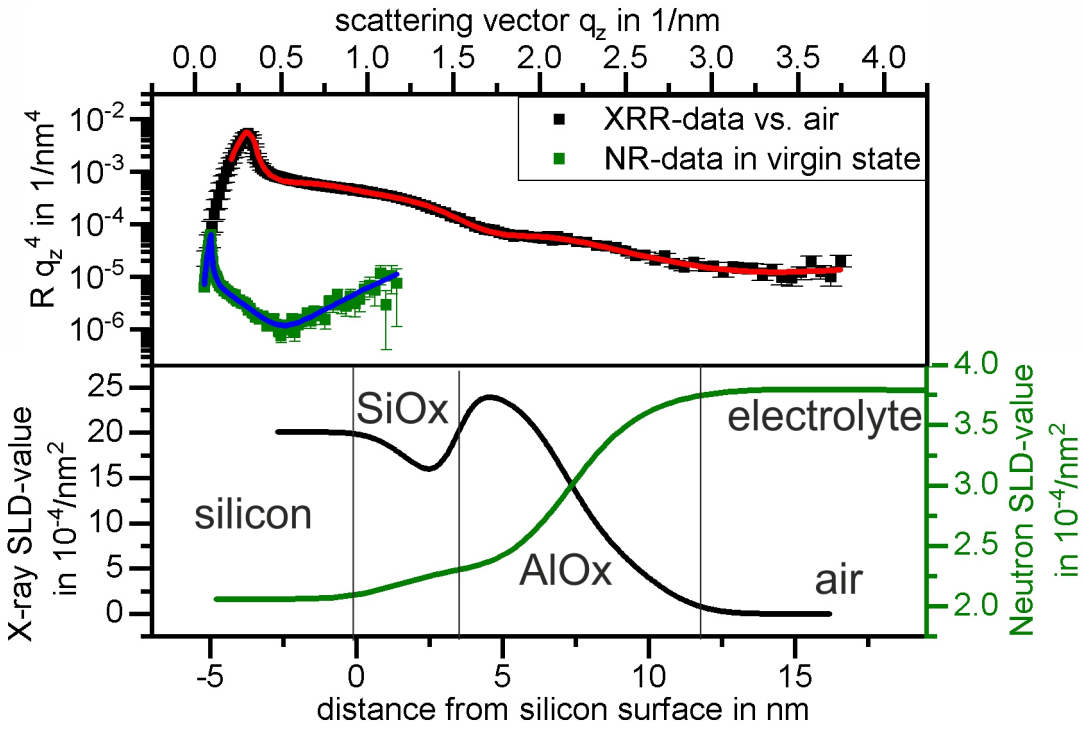

Figure 5.2: Characterization of the silicon wafer after coating using X-ray reflectivity. The reflectance data (black) and the obtained fit (red) are shown on the top. The corresponding SLD-profile is shown on the bottom. The aluminum oxide layer can be seen on the silicon, with a high roughness towards the air. An interlayer can also be found.

layers can be found in the X-ray SLD-profile, which are the aluminum oxide layer and the silicon oxide below the aluminum oxide with a thickness of 6.5 nm and 1.8 nm, respectively. The thickness of the oxide layer is comparable to results published elsewhere [50, 134]. The aluminum oxide possesses a higher roughness than coatings investigated elsewhere [43, 45, 134], probably caused by the sample preparation process which may introduce mass density changes within the layer. Therefore, the resulting SLD-value corresponds to a mixture of aluminum oxide and air, as described by eq. 2.32. The amount of air can be calculated by assuming a composition of Al_2O_3 of the aluminum oxide, resulting in a 3.3 nm thick layer of dense Al_2O_3. Compared to the 3 nm of deposited aluminum metal, this seems reasonable, although a slightly higher thickness of the oxidized film would be expected. However, no metallic aluminum phase seems to be present, which is supported by the neutron results. Only the native oxide layer can be detected here, together with the aluminum oxide layer on top. The high roughness of the artificial coating decreases the otherwise prominent SLD-contrast to the electrolyte.

5.3 Comparison of charge/discharge cycles

First, the lithiation behavior of an aluminum oxide coated silicon wafer compared to the uncoated cell will be discussed. Here the results from chapter 3 serve as a comparison. Both cells were cycled with a similar electrochemical sequence, which was a galvanostatic lithiation/delithiation followed by a 3-h period of open-circuit-voltage measurement (OCV) with impedance spectroscopy measurements in between. The lithiation continues for three hours once a voltage of 250 mV is reached since the silicon wafer can be regarded as infinite reservoir of silicon. Figure 5.3 shows the total charge flow during lithiation/delithiation.

A higher amount of charge is incorporated into the uncoated silicon. Also, the Coulombic efficiency is higher in the uncoated cell. The average Coulombic efficiency for the virgin silicon wafer is 0.977, whereas the sample with aluminum oxide coating exhibits a Coulombic efficiency of 0.899. This is in contrast to observations from Ai *et al.*, who reported an increase of the Coulombic efficiency for the samples coated with a $LiAlO_2$-layer [140]. The first, fifth, and tenth cycle of both samples are shown in figure 5.4. No significant differences can be found between the charging curves of both cells, except a longer charging time for the uncoated silicon. This is in line with the higher charge inserted and extracted during cycling. During discharging/lithiation, the initial voltage stays similar for the uncoated sample, whereas the aluminum oxide coated silicon shows a stepwise decreasing behavior. The cell voltage reaches faster the threshold value of 0.25 V for the coated sample. This may indicate the absence of an inhibiting SEI-layer on the silicon, although no distinct voltage

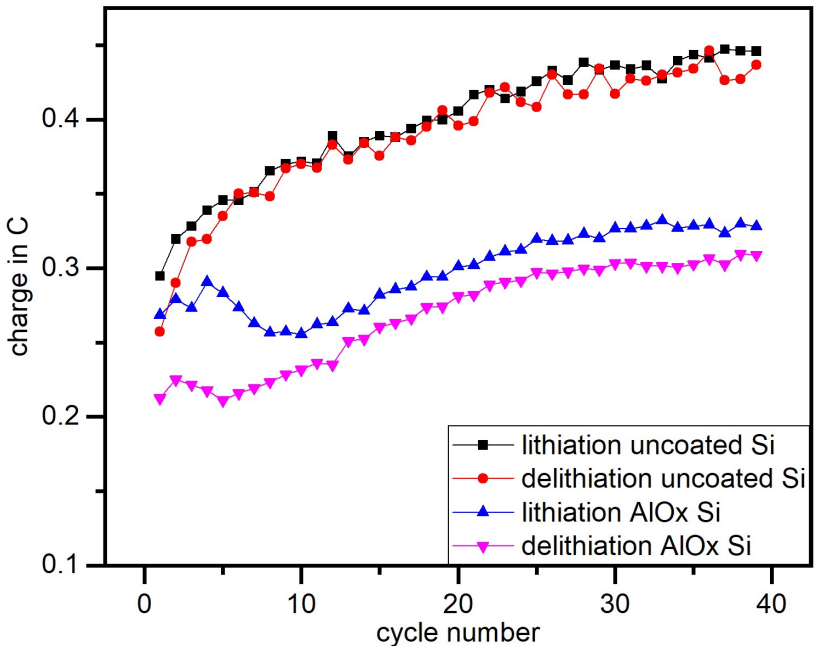

Figure 5.3: Charge flow during lithiation and delithiation of a lithium-silicon cell with and without aluminum oxide coating. Both cells were cycled with the same electrochemical sequence and similar materials were used. The coin cell data of chapter 3 was used for the uncoated silicon.

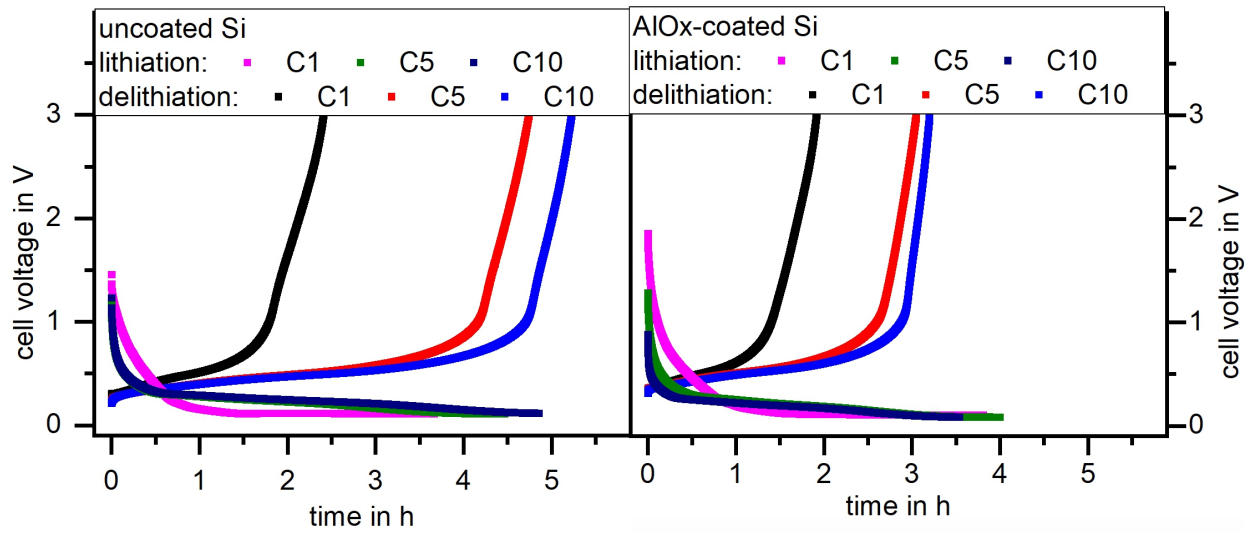

Figure 5.4: Lithiation/Delithiation curves of a lithium-silicon cell without (left) and with (right) aluminum oxide coating. The first, fifth, and tenth cycle are shown.

plateaus can be found. However, the aluminum oxide coating may also delay the ion transfer in the delithiated state, which would be in line with results from Jung *et al.* [141]. Except in the first cycle, both cells show the lithiation of amorphous silicon, followed by the lithiation of the underlying crystalline phase [3].

For further insights also electrochemical impedance spectroscopy was performed. An inductive loop and a solution resistance together with a distribution of relaxation times in series were used to model the electrical behavior of the samples. The equivalent circuit is shown in figure 5.13. The impedance spectroscopy was measured in the frequency range from 1 MHz to 0.1 Hz, with 15 Points per decade during the resting period and 10 points per decade afterward. Relaxations were evenly distributed on the logarithmic scale from 100 kHz to 1 mHz, whereas the total number of elements is equal to the number of measured points. Fig. 5.5 shows the obtained solution resistance in the upper part and the charge transfer resistances in the lower part. An inductance in the order of 10^{-7} H was determined. The solution resistance decreases during the initial resting period, most likely caused by the ongoing wetting process [94]. After six hours, this process is finished. The sample coated with aluminum oxide exhibits higher values for the solution resistance at the end of the resting period (5.3 Ω vs. 4.3 Ω for the aluminum oxide coated and uncoated sample, respectively), whereas the values are comparable during the first scans (roughly 8.5 Ω determined in the first impedance spectroscopy).

Both solution resistances drop down once the cycling starts. The uncoated sample shows a stable solution resistance from the 8^{th} cycle on with a small oscillation depending on the charging state. The lithiated state shows a slightly higher solution resistance (approx. 0.1 Ω). This difference decreases with increasing cycle number. The aluminum oxide coated sample also shows an oscillating solution resistance, but with an amplitude of 0.5 Ω. The solution resistance also shows an increasing trend at higher cycle numbers. The increased oscillation in the solution resistance originates from the

aluminum oxide layer since the lithium-ion diffusity strongly depends on the lithium concentration [141]. Therefore, the solution resistance is increased in the delithiated state. Pollak *et al.* reported a charge-state dependent conductivity of the silicon electrodes [95]. These findings coincide with observations made by DeCaluwe *et al.*, who also found charge-state dependent resistances [43]. The distribution of relaxation times is split into a fast and a slow part, representing relaxation processes with a time constant τ less or greater than 1.5 s, respectively (see also chapter 2.6.1). Solid squares represent the fast processes, whereas the hollow circles denote the slow processes. In comparable systems, relaxations associated with the lithium electrode were found within the fast relaxation

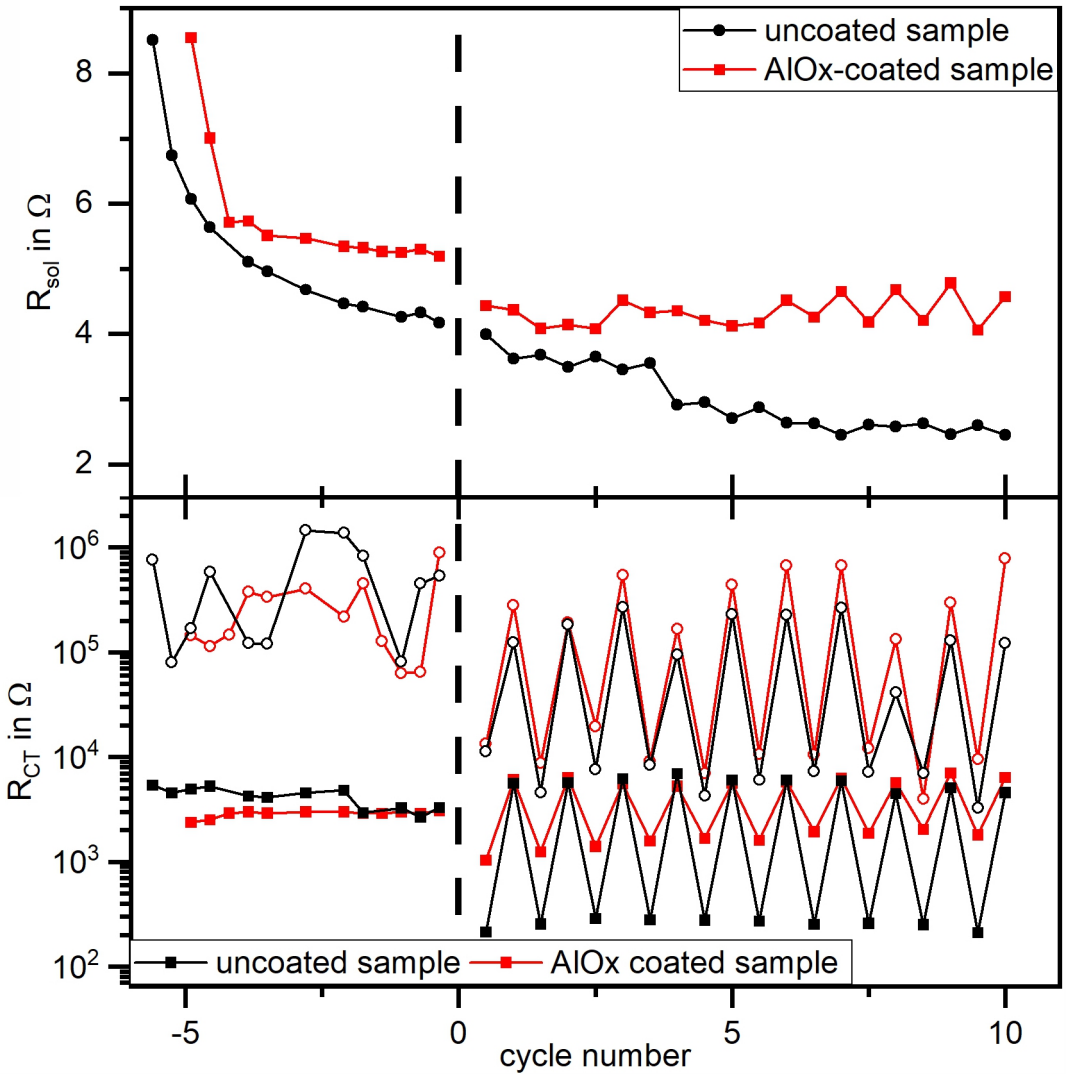

Figure 5.5: on top: Determined solution resistance of the uncoated silicon wafer (black) and the AlOx-coated wafer (red). At the bottom: Charge transfer resistances determined from the distribution of relaxation times. The hollow symbols denote the resistance of the slow processes ($\tau > 1.5$ s), whereas the solid symbols represent the resistance of the fast processes. The vertical line indicates the beginning of the galvanostatic cycling. The data of the uncoated silicon coin cell were reused from chapter 3

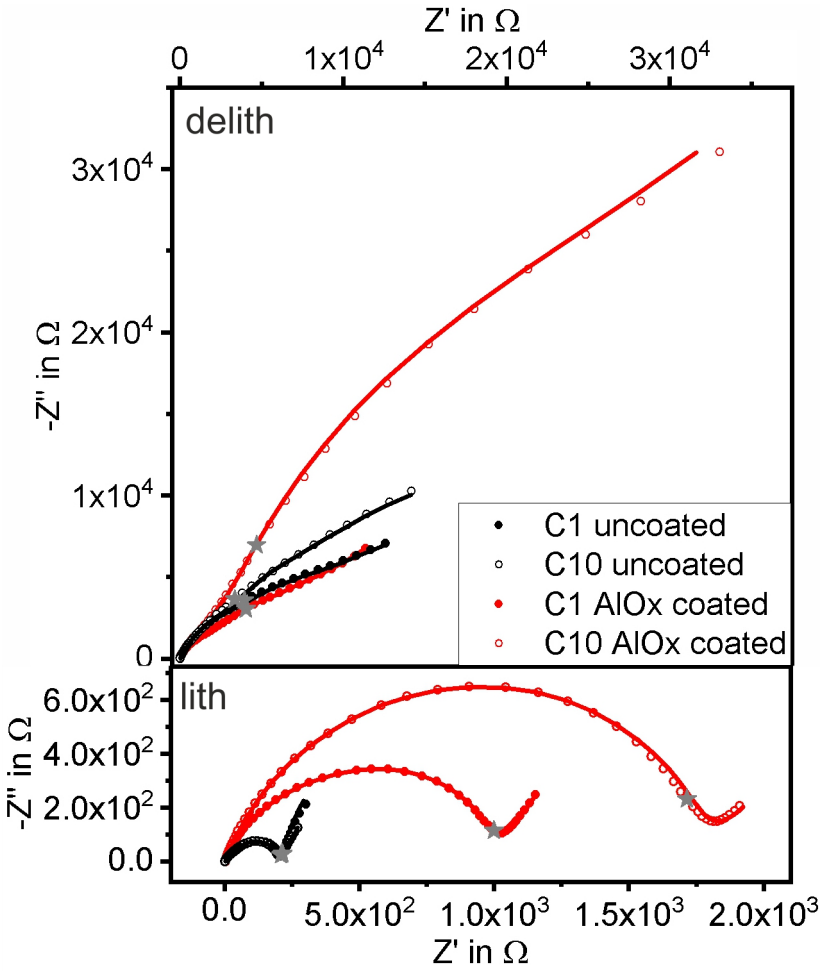

Figure 5.6: Nyquist-plot of the EIS-data. In the top the first (solid symbols) and tenth (hollow symbols) delithated states are shown for both samples, whereas the lithiated states are shown at the bottom. The solid line denotes the resulting fit. Black stars indicate the frequency of 1.5 Hz on the data. The data of the uncoated silicon coin cell were reused from chapter 3

regime [85, 129, 130]. The charge transfer resistance associated with the slow processes (which will be denoted as 'slow R_{CT}') is roughly 1.5 orders of magnitude higher than the fast R_{CT} (the charge transfer resistance associated with the fast processes). During the initial wetting period, the trend of the R_{CT} for both samples is comparable: The fast R_{CT} changes only slighly, whereas the slow R_{CT} varies by one order of magnitude. A local minimum can be found for both samples just before the cycling starts, followed by a steep increase. This is probably caused by processes occurring on the silicon electrode, where a spontaneous formation of an SEI-layer was reported by Veith *et al.* [41].

During cycling, both R_{CT} for both samples increase during delithiation and decrease during lithiation. For the slow R_{CT} the values of both samples are comparable. The fast R_{CT} is also comparable in the delithiated state for both samples, whereas the aluminum oxide coated sample's lithiated state exhibits higher values of the fast R_{CT} (roughly by a factor of 5). Fig. 5.6 illustrates this phenomenon

with a set of Nyquist-plots of the impedance data, showing clearly an increased impedance for the coated sample. This originates from the aluminum coating since this is the only difference between both samples. The lithium transport through the artificial coating introduces an additional charge transfer resistance which seems to affect only the lithiated state and impedes the charge transfer through the layer. This is in contrast to Jung *et al.*, who found an increased lithium diffusity in the lithiated state [141].
An alternating behavior of the charge transfer resistances was observed already in chapter 3. The growth of a layer was found in the delithiated state. This layer serves as an additional barrier for the charge transfer and increases the charge transfer resistance. The results discussed here indicate, the aluminum oxide layer does not suppress the formation of this surface layer, contrary to the findings of DeCaluwe *et al.* [43] and Becker *et al.* [135]. For further insights, structural information about the electrode surface is needed. Neutron reflectivity is a suitable analysis tool, since layers form within and on top the electrode ind it has proven its applicability already (see also chapters 2.3 and 3).

5.4 *Operando* structure analysis and electrochemical results

The electrochemical cell presented in chapter 3 was used for the *operando*-measurements. A detailed discussion of the cell is given in chapter 2.5. The electrochemical results are shown in fig. 5.7. The upper part shows the voltage profile. Here OCV-measurements are drawn in black. Impedance spectroscopy measurements are drawn in green. The cycling of the cell is shown in red. The lower part shows the results of the electrochemical impedance spectroscopy, where the solution resistance is denoted with black symbols and the charge transfer resistance (R_{CT}) is drawn with red symbols (solid symbols for processes with a time constant $\tau < 1.5$ s, hollow symbols for processes with $\tau > 1.5$ s). The lines just serve as 'guide to the eye'. The structural results obtained by *operando* neutron reflectometry are shown in figure 5.9. Here the surface of the silicon is located at a depth of zero. An overview of the most important quantities is given in tables 5.1 and 5.2.
A six-layer system was used to fit the SLD-profile to the experimental data. The first three layer are used as lithiated layers with increasing lithium content. The fourth layer models the native silicon oxide, the fifth layer models the aluminum oxide. The last layer represents the SEI-layer. However, these definitions are not fixed and also allow the occurrence of several SEI-layers. More layers do not improve the residuum χ, a four-layer and a five-layer system has a higher residuum. The corresponding results are shown in fig. 5.8. A detailed description of the calculation of the residuum is given in the experimentals-section. Also the usage of additional information, e.g. the charge within the silicon, is described there.
In the beginning, the cell was left in **OCV**-mode for 13 h (part 0). The initial resistances R_{sol}, $R_{CT,\,slow}$, and $R_{CT,\,fast}$ are higher than their counterparts in chapter 3. This was already observed in the coin cell data. The initial OCV-value is 2.85 V. The SEI-layer exhibits a thickness of roughly 8 nm, as already discussed in figure 5.2 and shown in part 0 of figure 5.9). However, after approx. three hours the SEI-layer increases in thickness. This indicates the growth of an additional SEI-

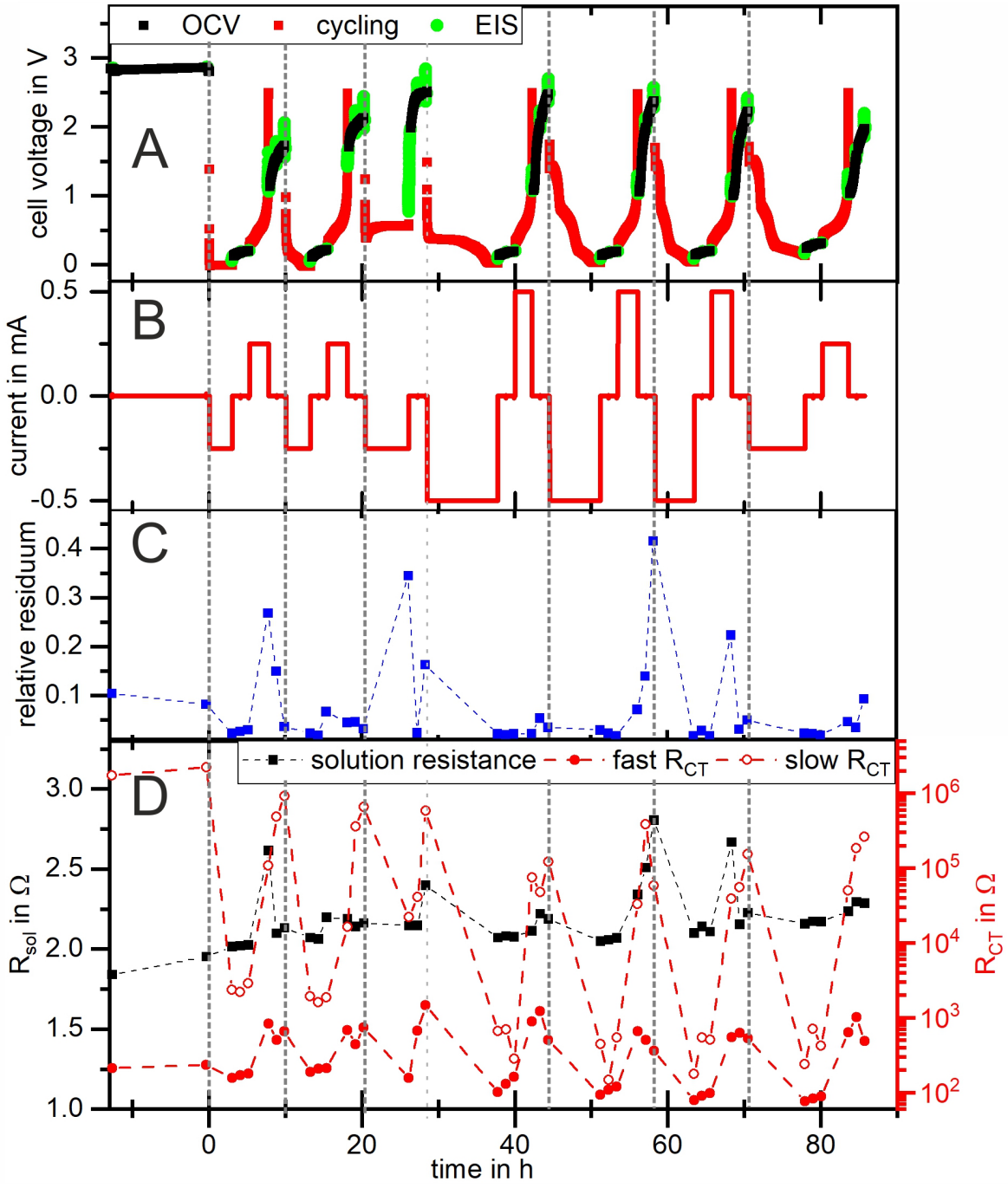

Figure 5.7: Electrochemical results of the neutron reflectivity cell. A: voltage profile of the cell. OCV-periods are drawn in black. Red represents the galvanostatic (de-)lithiation. Green denotes the measurement of EIS. B: Current profile of the cell operation. Within the third cycle, the current was increased and decreased again after the fifth cycle. C: The modulus of the residua of the EIS-data fitting. The residuum is a complex number containing the relative deviation between model and impedance data of the real and imaginary part. The modulus of this number is shown. D: Solution resistance R_{sol} (black) and charge transfer resistances (red) determined from the distribution of relaxation times. The hollow symbols denote the resistance of the slow processes ($\tau > 1.5$ s), whereas the solid symbols represent the resistance of the fast processes($\tau < 1.5$ s). The dashed lines indicate the beginning of a new cycle.

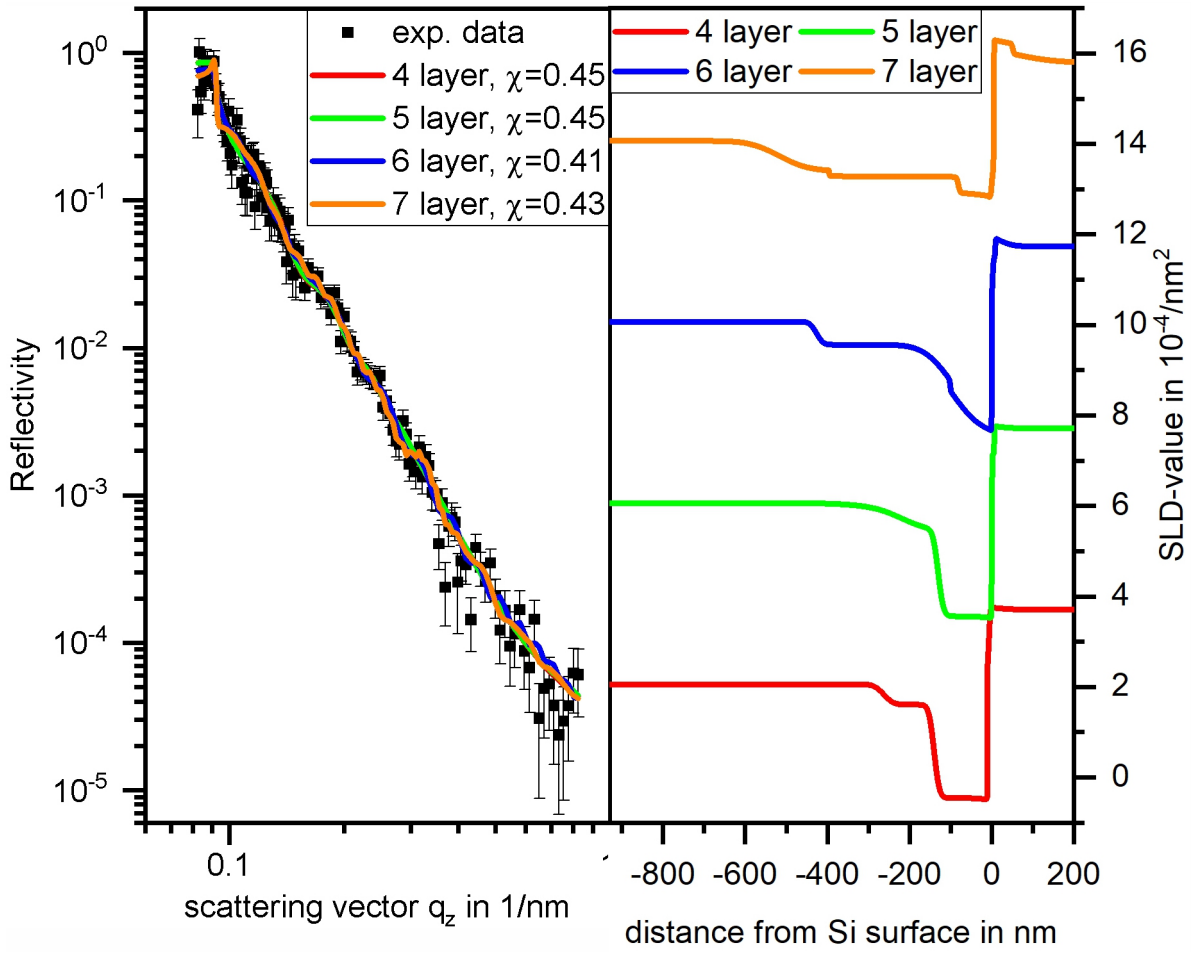

Figure 5.8: Reflectivity data of the first lithiated state (black dots on the left) together with a 4-layer, 5-layer, 6-layer, and 7-layer fit. The SLD-profiles are shown on the right. The profiles are shifted vertically to improve readability. The 6-layer fit exhibits the best residuum.

layer, as also reported by Veith *et al.* for amorphous silicon after five days of aging [41]. Seidlhofer *et al.* also observed such a layer at the beginning of their experiment using uncoated crystalline silicon [50]. Compared to the results from chapter 3, the additional layer is thinner, but the cell in chapter 3 was aged for five days, whereas this cell was aged for roughly 12 h. A slight increase of the cell resistance R_{sol} by 0.1 Ω can be found, also the R_{CT}-values increase slightly. These numbers are in line with the observed growth on an initial reaction layer.

In the **first cycle** (part 1), the lithiation of crystalline silicon started nearly immediately. During the initial part of the lithiation, the total SEI-layer thickness shrinks to 3 nm after 1 h of lithiation. The measured cell voltage was slightly negative (-4 mV), which can be explained by the increased impedance arising from the aluminum oxide layer. Jung *et al.* found only low diffusion coefficients for lithium within pure aluminum oxide compared to the lithiated state [141]. The plating of lithium was not observed, but the formation of a lithium-rich layer within the silicon. The Li-concentration is higher than the results reported in chapter 3 and comparable to Seidlhofer *et al.* [50]. In parallel

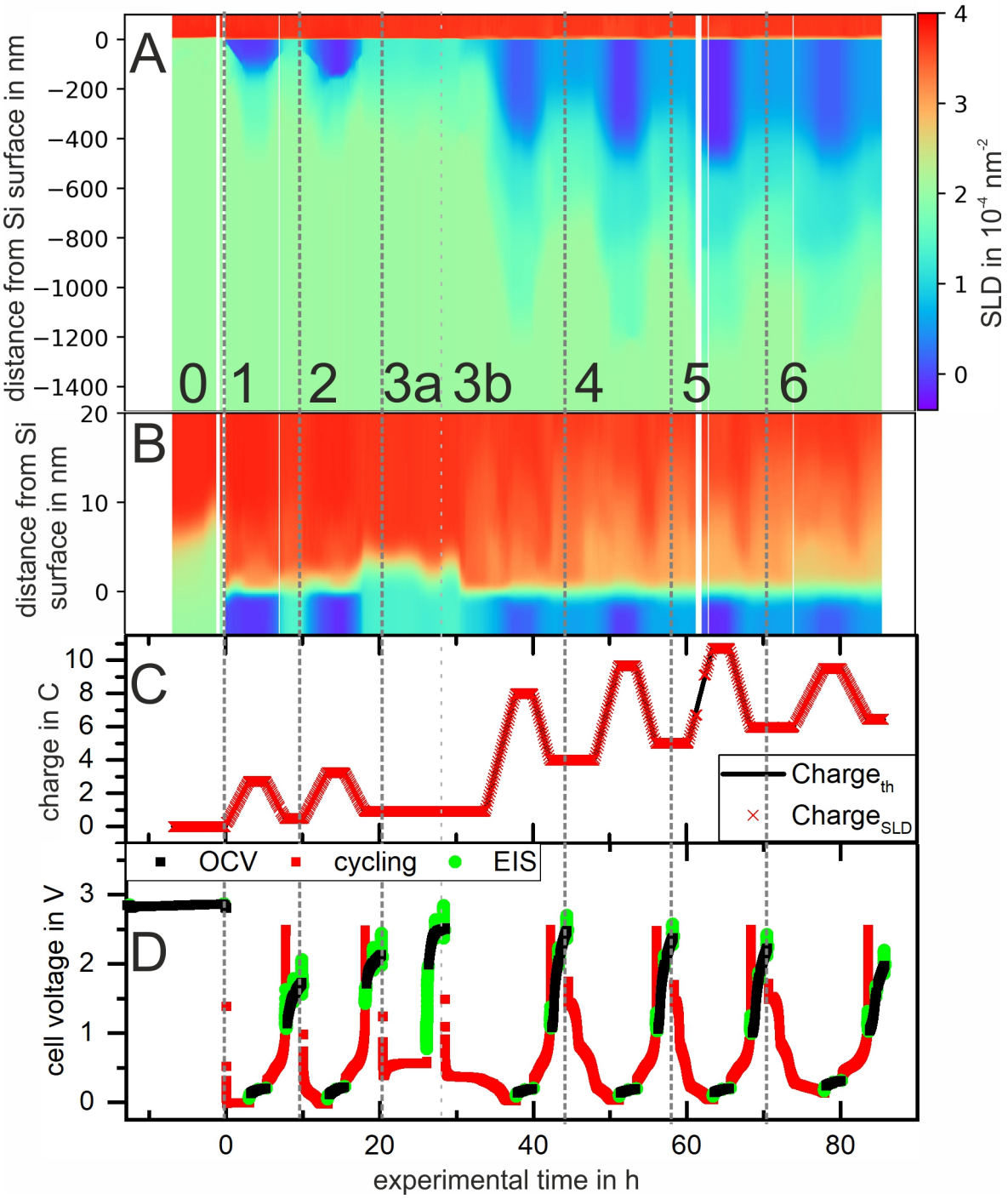

Figure 5.9: SLD-profiles of the cell during cycling. A: SLD-map over the whole depth to illustrate the growth of the lithiated zone. B: Zoom-in of A around the surface to highlight the SEI-layer on the silicon. The same color code as A is used. C: Charge as expected from the voltage/current data (black) and calculated based on the SLD-profile(red). D: Voltage-profile of the cell. Periods of OCV-measurements are drawn in black. Galvanostatic cycling is drawn in red. Electrochemical impedance spectroscopy is drawn in green. The vertical dashed lines mark the beginning of a lithiation (indicated by Arabic numbers in part A). 0 stands for the initial wetting process. Cycle 3 is split into parts a and b since the cell operation was stopped to increase the current. The white areas indicate the absence of data due to a beam loss.

to the growth of the highly lithiated zone, its lithium concentration also increases slightly. The outer part of the SEI-layer grows during the OCV-period in the lithiated state. Such an expansion of the SEI-layer in the lithiation was not observed in chapter 3 and also not reported for the uncoated silicon [49, 50].

During delithiation, lithium is extracted from the lithiated zone, which starts to shrink. The highly lithiated silicon collapses at the end of the delithiation. The lithiated region is not entirely dissolved. Such trapping of lithium was already observed elsewhere [50, 107, 108]. In total, 0.5 C or 19% of the charge remains within the silicon. At the end of the delithiated state, the growth of an SEI-layer can be observed, similar to the uncoated sample (chapter 3). Decreased charge transfer resistances are found in the lithiated state, compared to the delithiated state before and after. Similar observations were made in chapter 3, where the decreased charge transfer resistance

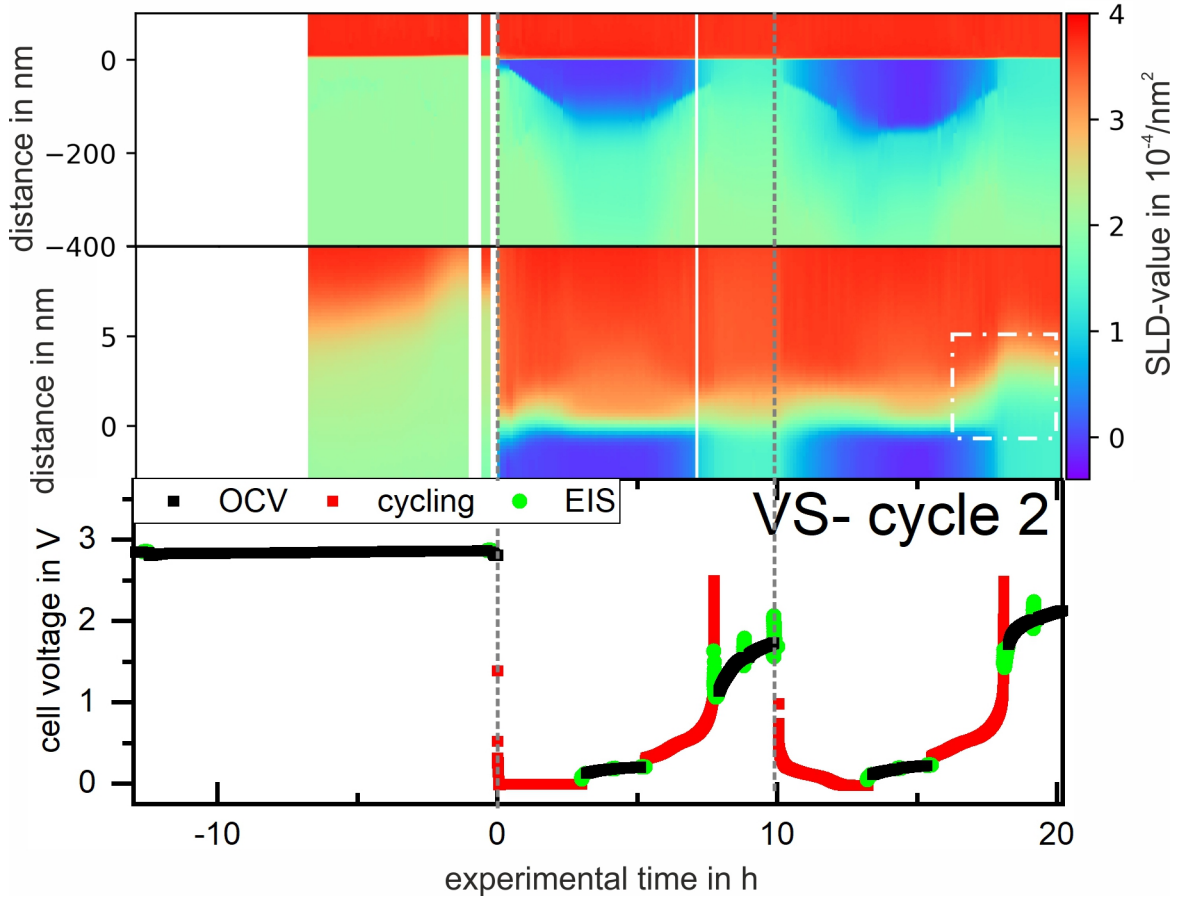

Figure 5.10: SLD-profiles of the initial wetting and the first and second cycle. Part A: SLD-map over the whole depth to illustrate the growth of the lithiated zone. Part B: Zoom-in of A around the surface to highlight the SEI-layer on the silicon. Part C: Voltage-profile of the cell. Periods of OCV-measurements are drawn in black. Galvanostatic cycling is drawn in red. Impedance spectroscopy is drawn in green. The beginning of the cycles is indicated by a dashed line. The white dash-dotted rectangle at the right part shows the growth of an additional layer on the silicon electrode, indicating the decomposition of the protective coating. The white areas indicate the absence of data due to a beam loss.

was accompanied by the dissolution of the SEI-layer [53].

The **second cycle** (Part 2) also shows no side reactions, in contrast to the uncoated sample (chapter 3). The SEI-layer starts to dissolve once a current is applied. This process continues in parallel to the lithiation. Again the two distinct lithiated zones (high and low Li-content) can be found, with a slightly thicker highly-lithiated zone than in the previous cycle. The lithiation of the amorphous phase is finished after two hours, corresponding to approx. 1.8 C. This is remarkable since the prior delithiation released 2.2 C of charge, and the delithiated silicon remains in the amorphous phase [3, 27, 28]. This phenomenon was also observed with the uncoated sample. The final voltage is again slightly negative (-20 mV). The transition towards the lowly lithiated zone seems to be broader than in the previous cycle.

The delithiation is similar to the first cycle. Again roughly 15 % of the inserted charge is trapped in the silicon, which sums up to 0.9 C with the trapped charge from the previous cycle. In the final part of the delithiation, an additional layer on top of the silicon electrode grows (white rectangle in fig. 5.10). The charge transfer resistance in the delithiated state is increased compared to the lithiated state. The surface of the silicon electrode seems to roughen and the SEI-layer expands. This may indicate a degradation of the protective coating.

The **first and second cycle** observations can be concluded as follows: The aluminum oxide layer suppresses side reactions, although the SEI-layer growth is not completely hindered. A fraction of 15 % of the lithium remains in the silicon after delithiation, leading to an increased amount of trapped lithium with cycling. The charge transfer resistances show the same tendency as for the uncoated sample (chapter 3), but the aluminum oxide layer is an additional bottleneck for the lithium transport, leading to higher impedances [45].

The **third cycle** (part 3a) starts with a voltage drop to 390 mV after 500 s, followed by a voltage plateau around 500 mV. No morphological change can be found (fig. 5.11). After approx. 5.7 h the lithiation was stopped, and the cell was left in OCV-mode for two hours. Although no change was observed by NR-measurements, a drop of the slow R_{CT} can be found, indicating a partial decomposition of a charge-transfer inhibiting layer (see fig. 5.7).

After the current was doubled (part 3b), the voltage drops down again to 500 mV and slowly decreases, also the SEI-layer shrinks (see grey rectangle). A similar irreversible high-voltage capacity was observed by Beattie *et al.* on tin electrodes [142] and may originate from decomposition reactions within the electrolyte, arising from traces of impurities [143]. The plateau for the lithiation of crystalline silicon is reached around 30 mV and the SEI-layer grows slightly. No distinct interface between the highly and lowly lithiated zone can be observed but a rough transition from one to the other. The lithium concentration maximum is $Li_{1.74}Si$, which is approx. one lithium per silicon atom less than in the prior cycle. A charge of 14 C was involved in the side reactions. During delithiation, roughly 4 C of charge was removed from the silicon, leaving another 4 C within the silicon. This high fraction of remaining lithium indicates an inhibition of the delithiation process, although no additional SEI-layer is found at the end of the delithiation but during the subsequent OCV-period. EIS reveals again an alternating behavior of the charge transfer resistances, where the smaller values can be found in the lithiated state. The charge transfer resistance of the slow

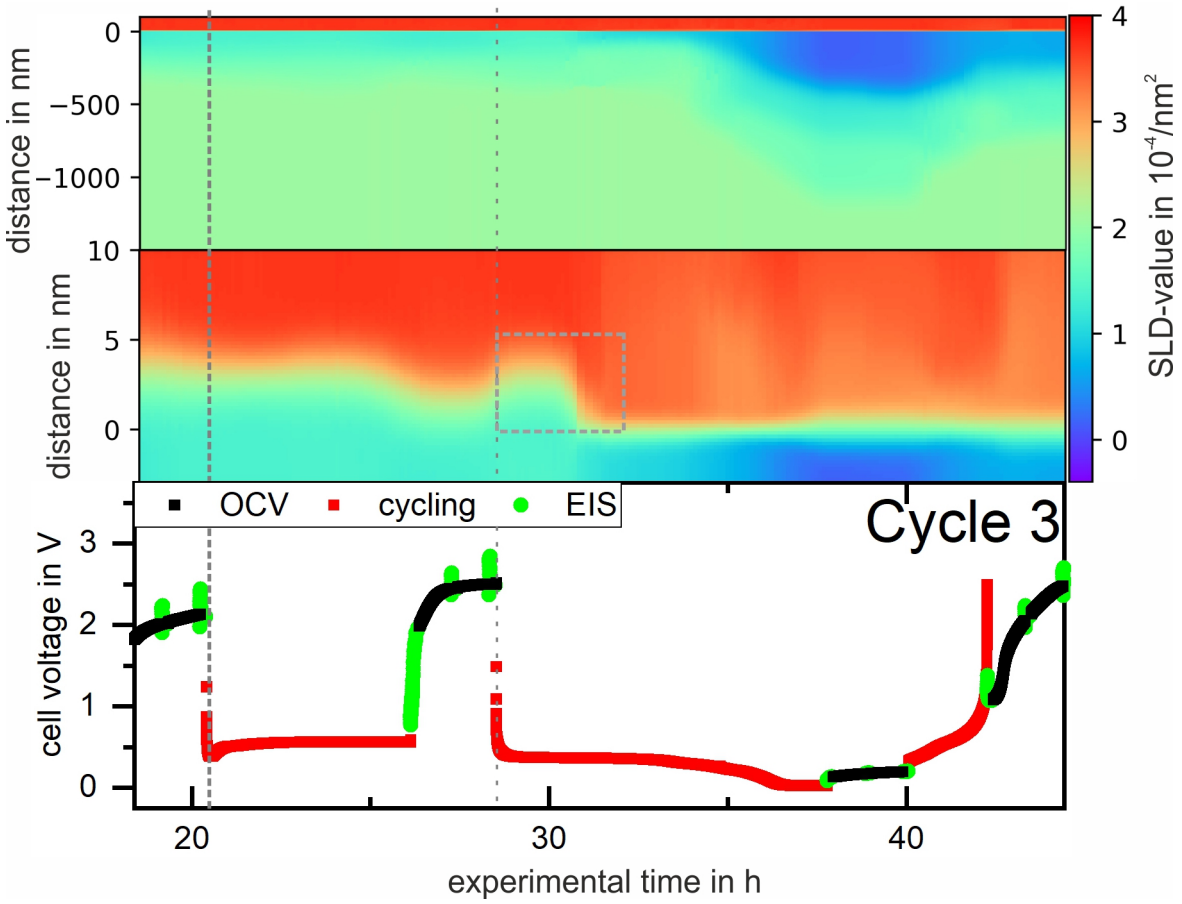

Figure 5.11: SLD-profiles of the third cycle. Part A: SLD-map over the whole depth to illustrate the growth of the lithiated zone. Part B: Zoom-in of A around the surface to highlight the SEI-layer on the silicon. Part C: Voltage-profile of the cell. Periods of OCV-measurements are drawn in black. Galvanostatic cycling is drawn in red. Impedance spectroscopy is drawn in green. A dashed line indicates the beginning of a cycle, the current increase is marked by a dotted line. The grey dashed rectangle highlights the dissolution of the SEI-layer on top of the electrode.

processes $R_{CT,slow}$ decreases approximately by a factor of five compared to the first two cycles.
The **fourth cycle** (part 4) shows three different plateaus on the voltage (around 1.4 V, around 0.75V, and around 40 mV). While the last one corresponds to the lithiation of crystalline silicon, no morphology change for the first plateau can be observed (fig. 5.12). The second plateau corresponds to a SLD-decrease of the SEI-layer. The lithiated zone starts to grow again once the voltage is lower than 300 mV, accompanied by a slight shrinkage of the SEI-layer. The lithium concentration increases to approx. $Li_{2.3}Si$. During the delithiation, the SEI-layer shrinks to 7.5 nm. The EIS-measurements reveal the previously observed behavior of decreased R_{CT}s in the lithiated state, whereas they increase during delithiation. The SEI-layer expands during the OCV-period in the delithiated state.
The **fifth cycle** is comparable to the fourth cycle. Again the two additional voltage plateaus can be found around 1.4 V and 0.75 V as well as the lower plateau around 45 mV. The SEI-layer shrinks

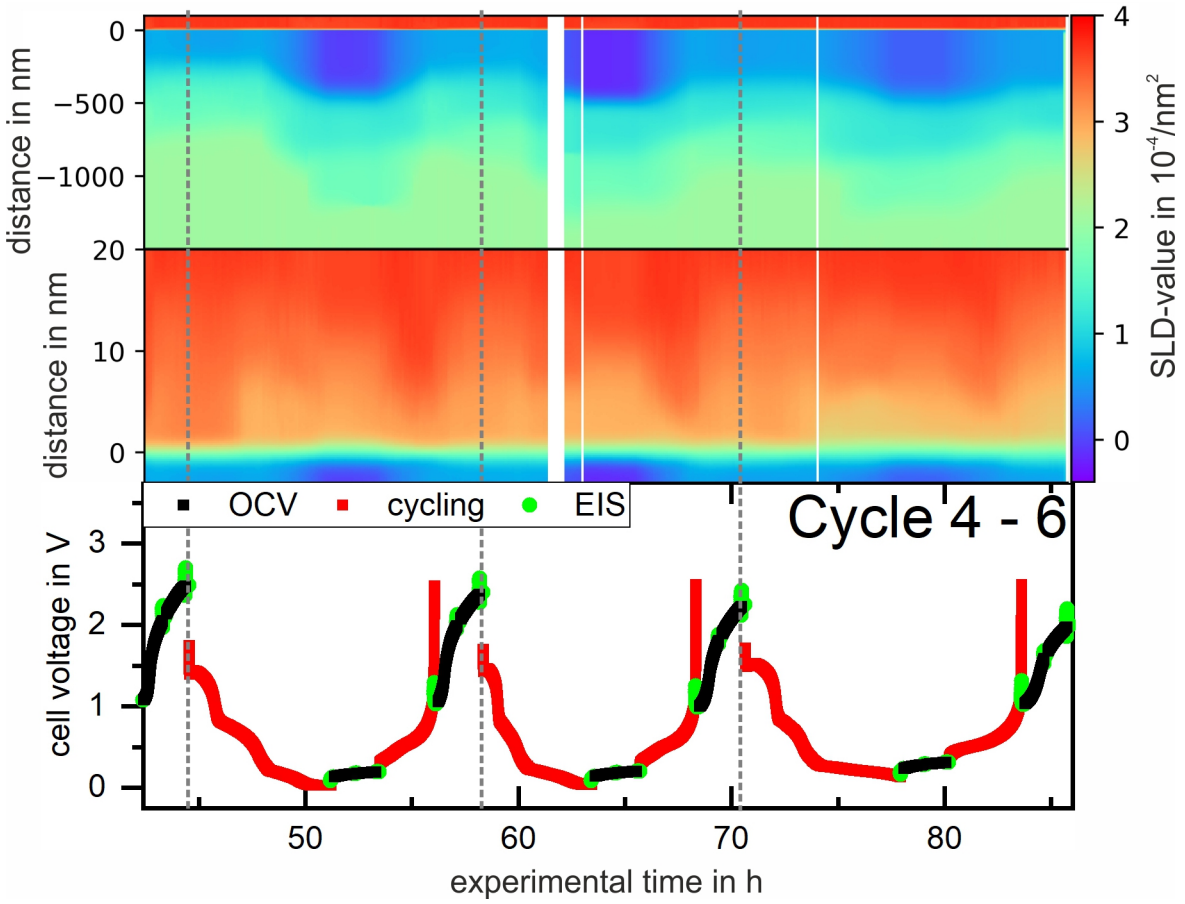

Figure 5.12: SLD-profiles of the fourth to the sixth cycle. Part A: SLD-map over the whole depth to illustrate the growth of the lithiated zone. Part B: Zoom-in of A around the surface to highlight the SEI-layer on the silicon. Part C: Voltage-profile of the cell. Periods of OCV-measurements are drawn in black. Galvanostatic cycling is drawn in red. Impedance spectroscopy is drawn in green. The start of a cycle is indicated by a dashed line. The white areas indicate the absence of data due to a beam loss.

again when the lithiation starts. Also, the EIS-measurements show the same trend as in the previous cycles. After the delithiation is finished, the SEI-layer grows again to a thickness of roughly 16 nm. The **sixth cycle** was done again with a decreased current of 250 µA. The two additional voltage plateaus at 1.5 V and 0.75 V can be found again, but with an increased length. The maximum lithium concentration is $Li_{1.8}Si$, which is lower than in the previous cycle. The amount of trapped lithium decreases again to 0.5 C. The SEI-layer shrinks during delithiation but grows again once the highly lithiated layer is depleted. A maximum thickness of the SEI-layer of 20 nm was observed at the OCV-period in the delithiated state. The charge transfer resistances show the same behavior as in the previous cycles. An overall cell resistance of 2.3 Ω is determined after the sixth cycle.
The behavior of the **cycles 3 to 6** can be summarized as follows: Side reactions are observed at various voltage plateaus, which impede the lithiation reaction, similar to the results of chapter 3. This indicates the decomposition of the protective layer. The interface of the highly and lowly lithiated zone widens compared to the first two cycles. The maximum of the lithium concentration

lithiation number	nr.1	nr.2	nr.3	nr.4	nr.5	nr.6
thickness highly lith. zone	120 nm	150 nm	360 nm	430 nm	490 nm	450 nm
maximum Li per Si	2.4	2.6	1.7	2.3	2.7	1.8
total thickness lith. zone	470 nm	470 nm	1200 nm	1250 nm	1260 nm	1300 nm
stored charge	2.7 C	3.2 C	8.0 C	9.7 C	10.7 C	9.5 C
thickness SEI-layer	5 nm	5 nm	10 nm	13 nm	12 nm	13 nm
fast R_{CT}	170 Ω	200 Ω	160 Ω	120 Ω	100 Ω	90 Ω
slow R_{CT}	2.4 kΩ	1.8 kΩ	0.28 kΩ	0.55 kΩ	0.51 kΩ	0.42 kΩ
R_{sol}	2.0 Ω	2.0 Ω	2.1 Ω	2.1 Ω	2.1 Ω	2.2 Ω

Table 5.1: Obtained structural and electrochemical parameter values for the lithiated states. The first two cycles are marked in blue.

decreases in the third cycle but increases afterwards again. The lithiation depth reaches 1300 nm, which is higher than reported in other reflectometry studies [50, 51, 53]. Fractures can be expected at such length scales of the lithiated layer [31, 32, 111, 144]. However, this was not observed and would lead to differences between the expected and SLD-charge, which was also not observed. An SEI-layer can be found on top of the silicon electrode. The SEI-layer seems to follow a cyclic morphology-change:

1. The SLD of the SEI-layer decreases slightly during lithiation; also the thickness decreases slightly.
2. During the followed OCV-period, the SLD increases again.
3. In the subsequent delithiation, the layer thickness decreases.
4. The SEI-layer grows again during the OCV-period in the delithiated state, reaching a higher thickness than in the previous cycle.

The tables 5.1 and 5.2 summarize the obtained parameter values for the lithiated and delithiated states, respectively. Especially the slow R_{CT} differs by orders of magnitude between the lithiated and the delithiated state, and is decreased compared to the first two cycles. The results indicate the degradation of the artificial layer.

5.5 Conclusion

The lithiation of crystalline silicon coated with a thin layer of aluminum oxide was studied under *operando*-conditions using neutron reflectometry. Additional electrochemical measurements and EIS allow us to gather a multidimensional view on the lithiation process. In total, six cycles were investigated. The evaluation method employed already in chapter 3 was further improved to handle the large amount of experimental data. The main findings are:

delithiation number	nr. 0	nr.1	nr.2	nr.3	nr.4	nr.5	nr.6
maximum Li per Si	0	0.3	0.3	1.0	1.0	1.1	1.0
thickness of lith. zone	0 nm	300 nm	350 nm	760 nm	900 nm	960 nm	970 nm
stored charge	0	0.5 C	0.9 C	4.0 C	5.0 C	6.0 C	6.4 C
thickness SEI-layer	11 nm	9 nm	6 nm	15 nm	16 nm	16 nm	18 nm
fast R_{CT}	210 Ω	660 Ω	740 Ω	510 Ω	660 Ω	620 Ω	1000 Ω
slow R_{CT}	1700 kΩ	910 kΩ	650 kΩ	120 kΩ	380 kΩ	55 kΩ	180 kΩ
R_{sol}	1.8 Ω	2.1 Ω	2.2 Ω	2.2 Ω	2.3 Ω	2.2 Ω	2.3 Ω

Table 5.2: Obtained structural and electrochemical parameter values for the delithiated states. Cycle 0 is the initial wetting period. The first two cycles are marked in blue.

1. The aluminum layer protects the silicon electrode successfully in the first two cycles, although no distinct layer is visible with neutron reflectivity. The layer probably exhibits a mass density gradient or an oxygen-gradient across the layer thickness or both. This creates a rough layer and decreases the contrast.

2. After the first two cycles, side reactions can be found at voltages higher than 700 mV, delaying the lithiation. The protective coating seems to be destroyed or at least degraded at the end of the second cycle. The silicon surface is not protected anymore and side reactions take place. Special care has to be taken to create stable protective coatings.

3. During the lithiation process at voltages $<$ 300 mV, no side reactions are found. All the charge provided here participates in the lithiation process. This means the charge efficiency of the lithium transfer to the silicon is almost one. The same observations were made for the delithiation process. These results are comparable to the observations made in chapter 3. 15 to 20 % of the inserted lithium remain trapped in the silicon [107]. The side reactions are the main reason for the decreased coulombic efficiency.

4. A cyclic expansion and contraction of the SEI-layer observed, as already described elsewhere for the uncoated silicon [49, 145]. The protective coating does not completely suppress the formation of an SEI-layer but the layer itself is thinner [135]. The charge transfer resistance is increased compared to the lithiated state, but the charge transfer is not prevented.

Nevertheless, a detailed degradation of the protective layer could not be followed. Here a better layer quality, probably by another preparation process, would be beneficial. A deuteration of the second solvent in the electrolyte (ethylene carbonate) or the use of isotope-labelled $LiPF_6$-salt could also reveal valuable insights into the SEI-layer formation. This work highlights the importance of proper data handling and automatized analysis for *operando*-measurements.

5.6 Experimental details

The *operando*-neutron reflectometry cell described in chapter 2.5 was used for the experiment. A (100)-n doped silicon wafer was used (circular shape, 6 cm diameter, approx. 1 cm thickness). The wafer was cleaned with various chemicals before coating (EXTRAN MA01 from Merck in ultrapure water, 1:100; solely ultrapure water; Ethanol p.a. with ultrapure water, 1:1; Acetone, purity $>$ 99.5%, 2-Propanol, purity $>$ 99.8%). The protective layer preparation was done by depositing 3.0 nm of aluminum by electron beam evaporation on the silicon wafer under high-vacuum (pressure approx. $2 \cdot 10^{-7}$ mbar). A customized high-vacuum chamber was used. A quartz crystal microbalance determined a deposition rate of 0.1 nm/s. The employed current and voltage of the electron beam were 55 mA and 0.6 kV, respectively. Afterward, the vacuum chamber was flushed with air, and the samples were also stored in air to start the oxidation of the aluminum coating. An X-ray reflectivity measurement of the sample is shown in fig 5.2. Here a custom-made X-ray reflectometer was used (Cu-K_α X-ray radiation, angular accuracy: 0.001 °)
The electrolyte was prepared just before the experiment. Ethylene carbonate (Solvionic, battery grade, $H_2O < 20$ ppm) and d_6-Dimethyl carbonate (deuteration degree 99.84 %, water 0.04%) were mixed in a 1:1 ratio by volume. Afterward, $LiPF_6$-salt (Sigma Aldrich, battery grade, 99.99% trace metal basis) was added, resulting in a one molar electrolyte solution. The cell was assembled approximately six hours before the experiment in a helium-filled glovebox (H_20, $O_2 < 10$ ppm). A detailed description of the cell is given in chapter 2.5. A metallic lithium sheet was used as counter-electrode, while small parts of lithium oxide were removed with a scalpel. A porous polymer foil (Celgard 2700) was used as the separator. Initial electrochemical impedance spectroscopy reveals a cell resistance of roughly 1.8 Ω.
All electrochemical measurements were carried out using a GAMRY Interface 1000 potentiostat. An initial OCV-period of 13 h was used to ensure the wetting of the cell and due to experimental limitations (scheduled short maintenance period of the neutron source). At the beginning and the end of this wetting period, an EIS was measured with a frequency range of 1 MHz to 0.1 Hz, 15 points per decade, 3 mV rms amplitude of the excitation signal. After the wetting period, the cell was cycled with 250 µA, starting with the lithiation. Lithiation was stopped three hours after the cell voltage dropped below 250 mV. Afterward, a two-hour OCV measurement was done, with EIS measurement at the beginning, in the middle, and at the end of the OCV-period. Here the frequency range of 100 kHz to 0.1 Hz was covered, again 15 points per decade and 3 mV rms excitation signal amplitude. Afterward, the delithiation follows, which stops at a threshhold voltage of 3.0 V. In the cycles three to five the current was increased to 500 µA. Here a long voltage plateau at 550 mV was observed in the beginning of the third cycle. The last cycle was done again with 250 µA. In total, six complete cycles were investigated.
The impedance data were analyzed using the equivalent circuit shown in fig. 5.13. A custom made python script was used for data fitting (see chapter 2.6.1). Here the relative deviation between model and data in the real and imaginary part is taken as residuum, of which the square of the modulus is taken. In addition, the same procedure was done for the first derivative of the model

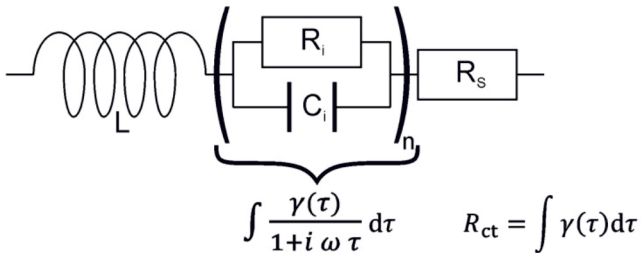

Figure 5.13: Equivalent circuit used for the analysis of the EIS-data. The inductive coil models the inductive behavior of the wires. The series resistance models the ohmic resistance of the electrolyte and electrodes. The faradaic impedance models the impedance arising from the charge transfer through interfaces.

and the experimental data, which is added to the first residua with an additional weigthing factor of 0.25. The residua drawn in fig. 5.7 C is only the modulus of the relative difference between the data and the model.

Neutron measurements were carried out at the OFFSPEC instrument at ISIS Neutron and Muon source [74]. Here a neutron wavelength band of 0.15 to 1.4 nm is available. Initially, 3 virgin state measurements were done, each one lasting one hour. A q_z-range of 0.05 to 2.49 /nm was covered. The *operando*-scans were performed in a smaller q_z-range of 0.083 to 0.99 /nm. Here the time resolution is roughly 6.75 minutes. The Mantid software package was used for data reduction [146]. Data analysis was done using a custom-made python script. Here parts of the refnx-software package were used for the reflectivity calculation [147]. A detailed description of the algorithm can be found in chapter 2.6.2. The source code can be found in the appendix.

As already in chapter 3, the residuum consists of 4 parts. The first part is the reflectivity residuum χ_{refl}, which is calculated based on the difference between simulated reflectivity and the data, weighted by the error.

The second part is the charge residuum χ_{charge}, arising from the difference between the expected charge and the charge calculated from the SLD-profile. The expected charge is the integration of the current for voltages smaller than 300 mV for the lithiation and the complete current during delithiation, since the lithiation of amorphous silicon starts at 300 mV [3]. The SLD-charge is calculated based on the SLD-profile under the assumption of a binary mixture, which allows the determination of the lithium concentration. Integrating along the depth yields the amount of lithium. The expansion of the silicon is taken into account here. However, at low lithium concentrations, the silicon lattice expansion may not be linear [34, 35, 50, 90]. Therefore, the calculated charge values may just serve as an estimation.

The third part χ_{change} is the difference between SLD-profiles to avoid sudden profile changes. Here up to 3 SLD-profiles before and after the current profile are taken. They were weighted by their time difference to the current dataset according to a gaussian distribution.

The last part χ_{bin} was the binary switch again to avoid non-meaningful profiles. The fitting was done over several rounds. The first fitround was done without χ_{change} to generate an initial solution. Afterward also χ_{change} employed to calculate the overall residuum, from the fourth fitround on χ_{refl}

was the major part. After 28 rounds, a fraction of the fitresults were replaced by earlier results since these showed a lower residuum and appeared to be more meaningful. Afterward, the fitroutine continued to validate this result. The average fraction of the different residua at the final result was: $\chi_{refl} \approx 0.763$, $\chi_{change} \approx 0.235$, $\chi_{charge} \approx 0.002$. χ_{bin} was usually zero since this residuum just discards or enables profiles. A detailed description can be found in chapter 2.6. In total, 34 fit rounds were done with each dataset.

Chapter 6

Conclusion

The aim of this thesis was the investigation of two different aging-mechanisms of silicon electrodes, which are the fracturization and the Solid-electrolyte-interphase(SEI)-layer formation. The problem of the electrode aging is schematically shown in fig. 6.1. *Operando*-techniques are used here since this allows us to characterize the silicon electrode during cell operation. Two different *operando*-techniques were used to probe these phenomenons on different length scales. The resulting morphology changes are summarized in fig. 6.2.
The first operando technique is neutron reflectometry, which was used in chapters 3 and 5 to probe the nanometer-scale of the silicon electrode (bottom part of fig. 6.2). This technique is very sensitive to thin layers as well as different elements, especially lithium (see also chapter 2.3). Therefore this method is well suited to study the behavior of the SEI-layer and the insertion and extraction of lithium during cell operation. An initial SEI-layer was found, which gets dissolved at a voltage plateau > 0.5 V. Afterward, the lithium insertion takes place without further side reactions. The SEI-layer grows again in the delithiated state. This cyclic SEI-layer change is schematically shown in fig. 6.2.
The results of chapters 3 and 5 are in line with other neutron-studies [49, 50]. However, X-ray reflectivity studies reveal the inverse behavior of the SEI-layer, a growth during lithiation and a shrinkage during delithiation [51, 91]. It is assumed that the SEI-layer consists of an inner, inorganic part and an outer, organic part [9–11]. X-ray reflectivity is more sensitive to the inorganic part of the SEI-layer, whereas neutrons are more sensitive for the organic part, leading to a complementary

Figure 6.1: Aging of a silicon electrode. On the left, a virgin electrode is shown. During cycling, aging processes take place, leading to a fracturization of the electrode and a continuous growth of the SEI-layer.

view on the SEI-layer[91]. The silicon expansion during lithiation creates cracks in the SEI-layer, which exposes new silicon surface to the electrolyte[3, 18]. Here the SEI-layer grows again, leading to a thickness increase in the subsequent delithiation.

A concentration gradient of the lithium was found within the silicon. A higher lithium concentration was found close to the silicon surface, whereas a lower lithium concentration was found towards the bulk of the silicon. In between, a transition zone was observed, which broadens with cycle number. The results suggest the formation of an amorphous Li-Si interphase with decreasing Li-content towards the bulk of the silicon. This is in contrast to McDowell *et al.* and Liu *et al.* [148, 149], who found atomically smooth interfaces between the lithiated phase and the silicon in their TEM-studies on nanoparticles. It is important to mention, reflectometry measurements average over the whole illuminated area but give depth information with a sub-nm resolution. The observed SLD-values allow us to calculate the depth-dependent lithium concentration in the electrode[50, 150].

The coating of the silicon electrode with aluminum oxide successfully decreases the growth of an SEI-layer and suppresses charge-consuming side reactions, as indicated in fig. 6.2. This was accompanied by an increase in the charge transfer resistance and an increasing amount of trapped lithium. The coating also resulted in higher lithium concentrations, which might be a consequence of a decreased lithium mobility within the silicon electrode. Furthermore, this protective layer was degraded after two cycles and lost its protective properties. Further studies are necessary to understand the origin of this failure since aluminum oxide proved its beneficial properties already [9, 43, 134, 135, 138]. The comparison to coin cell experiments also revealed a decreased performance of the aluminum coating, which may originate from the charge transfer inhibition associated with the artificial coating [141].

The µm-scale was probed by phase-contrast X-ray imaging (top part of fig. 6.2)). This technique is sensitive to material interfaces and can resolve the formation of cracks within the silicon electrode and their dependency on the charging state. This technique was applied in chapter 4. Here an orthogonal crack pattern was found after four cycles, which forms during the second half of the delithiation. During the lithiation, the pattern vanishes since the silicon expands. It reappears in the same position again in the subsequent cycle but grows with cycle number. However, the patches within the pattern seem to resist the fracturization. The appearance of the fractures is different to nanoparticles, where fractures grow during the lithiation [148, 149]. The reason for this different behavior is the different morphology.

The electrodes employed in this work are planar single crystal silicon electrodes. Here a lithiated amorphous phase on top of the still crystalline silicon is formed. Based on simulations done by Shi *et al.*, the fractures should be deflected on the interface between the amorphous and crystalline phase[48]. This should lead to a spalling of electrode material. However, in chapters 3 and 5, this was not observed, even though the highly lithiated zones reached a thickness of several hundred nanometers. Therefore, an inhomogeneous lithiation can be assumed, leading to a better stress distribution, which avoids fracturization [21, 151]. In chapter 4, the lithiated zone exceeded several µm, leading to the growth of fractures oriented in a checkerboard-like pattern. The fractures are aligned with the crystallographic axis of the underlying silicon, as Laue-diffraction revealed. This

indicates, the fractures nucleate in the pristine silicon matrix since silicon gets amorphous during lithiation and not preferred direction should exist in an amorphous phase [3, 18]. However, the fractures vanish once the silicon is lithiated again and reappear in the subsequent delithiation at the same position, as indicated in fig. 6.2as indicated in fig. 6.2. The fractures reappear after the first current peak in the delithiation, which is associated with the dissolution of the highly lithiated phase. This may enable a decrease of the fractures within the silicon, as long as the highly lithiated phase is maintained. The fractures do not heal, although the cracks become invisible for phase-contrast imaging. No spalling of electrode material was observed, which would result from the deflection of the cracks at the crystalline-amorphous interface [48].

Further work should address the artificial coating and an improvement of its properties. The coating suppressed side reactions in the beginning but degraded quickly. A detailed understanding of the degradation process would help to find more durable coatings. Furthermore, a better understanding of the lithium transport through the coating could reveal pathways to decrease the additional charge transfer resistance. Finally, the influence of the artificial coating on the mechanical fracturization should be studied. In combination with capacity-limited cycling, this may slow down the aging of silicon electrodes and pave the way into commercial applications.

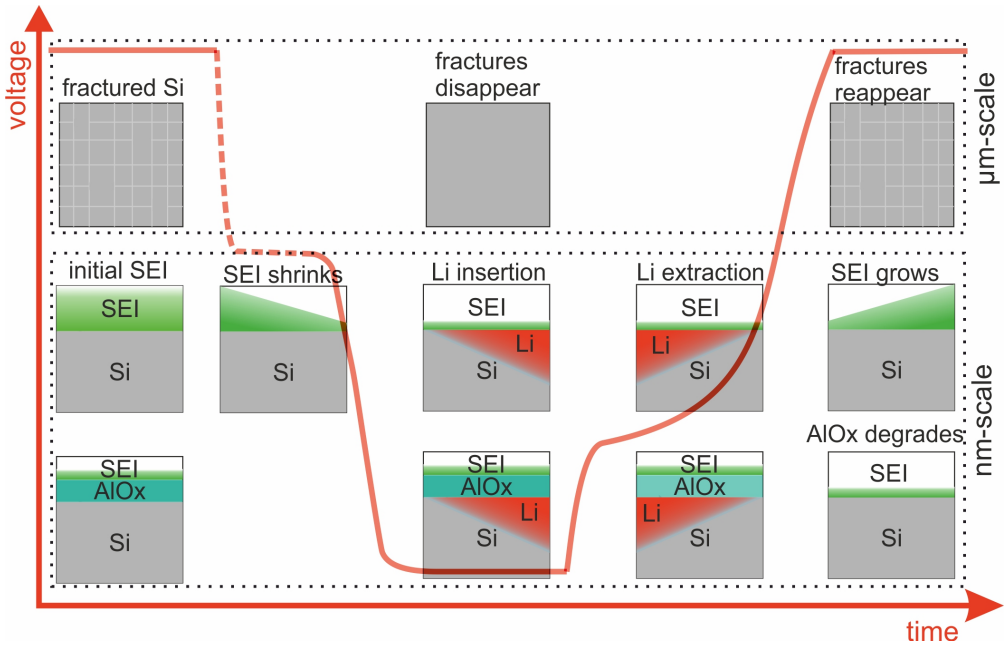

Figure 6.2: Summary of the results. The red line denotes the cell voltage. In the discharged state, a SEI-layer is observed(chapter 3) and a rectangular fracture pattern is found in the case of a cycled electrode (chapter 4). Once a current is applied, a plateau at voltages > 0.5 V is observed, which is associated with the dissolution of the SEI-layer (chapter 3). This is hindered as long as the protective coating is intact (chapter 5)

Appendix A

List of Abbreviations

AlOx	Aluminum oxide
BER II	Berliner Experimentier-Reaktor II
BESSY	Berliner Elektronenspeicherring-Gesellschaft für Synchrotronstrahlung
CPE	Constant Phase Element
EIS	Electrochemical Impedance Spectroscopy
EPDM	Ethylene Propylene Diene Monomer
EQC	Equivalent Circuit
FIB/SEM	Focussed Ion Beam Scanning Electron Microscopy
ILL	Institute Laue-Langevin
LIB	Lithium-Ion Battery
LIPON	Lithium Phosphorus Oxynitride
Li-Si-Cell	Lithium-Silicon-Cell
NR	Neutron Reflectivity
OCV	Open Circuit Voltage
PCI	X-ray phase-contrast imaging/radiography
PEEK	Polyether-Ether-Ketone
R-C-Unit	Resistor-Capacitor-Unit
SEI	Solid-Electrolyte-Interphase
SIFT	Scale-Invariant Fourier Transformation
SLD	Scattering Length Density
TEM	Transmission electron microscopy
TOF	Time-of-Flight
XRR	X-ray reflectivity
ZHiT	Zweipol-Hilbert-Transformation

Appendix B

List of Variables

Variables may contain additional indices, such as a number denoting the associated layer.

variable	meaning	unit
A	Amplitude of the incoming neutron/X-ray beam	particles/(cm^{2}s)
A_W	Warburg coefficient	$\Omega/s^{0.5}$
d	thickness	nm
C	capacitance	C/V = F
E	electrode potential	V
E(0)	standard electrode potential	V
E(beam)	photon energy of the incident beam	eV
F	Faraday constant	C/mol
H_+, H_-	Up-/downwards fields of the wave	particles/(cm^{2}s)
I	current	mA
$\vec{k}$	wave vector	1/nm
L	inductance	Ωs=H
n	refractive index	**1**
n_{mol}	amount of substance	mol
Q	Charge	C
Q_0	coefficient of the constant phase element	s^{ψ}/Ω
q_z	scattering vector	1/nm
R_{gas}	universal gas constant	J/(mol K)
R	resistance	Ω
R_{sol}	cell/solution resistance	Ω
R_{CT}	charge transfer resistance	Ω
SLD	scattering length density	10^{-4}/nm^2
T	temperature	K
t	time	s
U	voltage	V

W_{el}	electrical work	J
x	number of lithium atoms per silicon atom	**1**
Z	impedance	Ω
Z_f	faradaic impedance	Ω
Z^0	Impedance in the limit of low frequencies	Ω
Z^∞	Impedance in the limit of high frequencies	Ω
Z'	real part of the impedance	Ω
Z"	imaginary part of the impedance	Ω
z	depth or distance from surface	nm
z_e	charge number	**1**
α	chemical activity	mol/l
β	incoherent part of the refractive index	**1**
δ	coherent part of the refractive index	**1**
θ	angle of the radiation	rad
κ	linear absorption coefficient	1/nm
λ	wavelength	nm
μ	chemical potential	J/mol
P	reflectance	**1**
ρ	reflection coefficient	**1**
σ	roughness	nm
τ	time constant	s
τ_{trans}	transmission coefficient	**1**
Φ	electric potential	V
ϕ	phase shift between current and voltage	rad
χ	residuum of a model, calculated by the fitness function f	**1**
ψ	quality parameter of a constant phase element	**1**
ω	angle frequency	1/second
$\underline{P}$	reflection matrix	**1**
$\underline{T}$	transmission matrix	**1**

Appendix C

List of Publications

1. **Arne Ronneburg**, Marcus Trapp, Robert Cubitt, Luca Silvi, Sébastien Cap, Matthias Ballauff, and Sebastian Risse: **Surface structure inhibited lithiation of crystalline silicon probed with operando neutron refectivity**. Energy Storage Materials, 18, (2018), p. 182-189. DOI; 10.1016/j.ensm.2018.11.032

2. **Arne Ronneburg**, Markus Osenberg, Kang Dong, André Hilger, Eneli Härk, Luca Silvi, Ingo Manke, Matthias Ballauff, and Sebastian Risse: **Morphological evolution of a single crystal silicon battery electrode during lithiation and delithiation: An operando phase-contrast imaging study**. Energy Storage Materials, 32, (2020), p. 377 - 385, DOI:10.1016/j.ensm.2020.06.007.

Appendix D

Acknowledgement

Now it is time to say 'thank you' to everyone who helped me during my doctoral time.
First of all, I would like to thank Prof. Dr. Matthias Ballauff for the opportunity to conduct this thesis and for his guidance and advice during this time. I'd also like to thank Dr. Sebastian Risse for his support and the time he spend with me discussing various problems.
I'd like to thank Dr. Eneli Härk for the stimulating discussions about various electrochemical problems. Many thanks to Dr. Marcus Trapp, Dr. Luca Silvi, Dr. Roland Steitz and Dr. Daniel Clemens for sharing their knowledge about reflectometry with me and their help during various beamtimes. Also, many thanks to Dr. Kang Dong, Markus Osenberg, Dr. André Hilger and Dr. Ingo Manke for their help with the imaging techniques, the related data analysis and the operation of the BAMline-instrument.
A special thanks also to all the instrument scientists of the different neutron reflectometers used during this work: D17 (Dr. Thomas Saerbeck, Dr. Robert Cubitt), OFFSPEC (Dr. Joshaniel Cooper) and V6 (Dr. Luca Silvi, Dr. Marcus Trapp, Dr. Beatrix-Kamelia Seidlhofer, Dr. Roland Steitz). Another thanks goes to Karsten Harbauer for the deposition of the coating layers and to Jan-Ekkehard Hoffmann for the custom-made X-Ray reflectometer.
Furthermore, thanks to all colleagues who joined the different beamtime-trips: Dr. Marcus Trapp, Dr. Sebastian Risse, Dr. Luca Silvi, Dr. Eneli Härk and Dr. Martin Kärgell.
Another thank you goes to all co-authors and co-workers for their efforts and the stimulating discussions. Also, I'd like to say thank you for all the hints, proof-readers, reported mistakes, and advices which helped to improve this work.
A very special thanks to all the people sharing their time with me during coffee-breaks, lunch-breaks and pleasant conversations, in particular Linda Schmalz, Dr. Eneli Härk, Prof. Dr. Yan Lu, Daniel Besold, Dr. Luca Silvi, Dr. Martin Kärgell, Dr. Sebastian Risse, Dr. Charl Jafta, Dr. Shilin Mei, and Dr. Rafael Müeller.
I hope, I haven't forgotten someone to mention here, but also a 'thank you' to all the unmentionned persons, who helped me during this doctoral time.
Last but maybe most important, I'd like to thank my family and, in particular, Nicole and Hanja for their support during this time and for making me smile when coming home.

Appendix E

Statement of authors contribution

Parts of this dissertation were prepared in close cooperation with coworkers, such as the different publications arising from this work. Hereby I give a declaration which work was done by the coauthors of the publications and which work I did myself for the chapters 3, 4 and 5:
All researdch activities were supervised by Prof. Dr. Matthias Ballauff and Dr. Sebastian Risse.
Chapter 3 was a beamline-experiment performed at the Institute Laue-Langevin (proposal-nr. 1-04-110). The corresponding proposal was written by Dr. Sebastian Risse and Dr. Marcus Trapp. The employed *operando*-cell was developed by Dr. Sebastian Risse based on a cell designed by Dr. Marcus Trapp. Dr. Marcus Trapp and I conducted the experiment at the Institute Laue-Langevin, where Dr. Trapp took care about the neutron instrument and the data reduction whereas I assembled the cell and created the electrochemical sequence. The instrument scientist Dr. Robert Cubitt assisted with the configuration of the neutron instrument as well as the data reduction. The creation of the neutron data analysis script was done by me. Dr. Marcus Trapp, Dr. Sebastian Risse as well as Dr. Luca Silvi supervised the data evaluation process and helped with stimulating discussions. The EIS-analysis script for the NR-cell was created by Dr. Sebastian Risse. Additional coin cell measurements and the data evaluatation was done my myself. The discussion of the results and the writing of the manuscript was done by Dr. Marcus Trapp, Dr. Luca Silvi, Dr. Sebastian Risse, Prof. Dr. Matthias Ballauff and me. All authors joined the review process of the publication.
Chapter 4 was performed at the BAMline-beamline at BESSY II. The corresponding proposal was submitted by Dr. Kang Dong. Markus Osenberg controlled the instrument during the beamtime. The cell assembly was done by me, while the design of the electrochemical sequence was done together with Dr. Sebastian Risse. The reduction and analysis of the beamline-data were done by Markus Osenberg. The EIS-analysis script was created by Dr. Sebastian Risse. Ex-situ FIB/SEM measurements were done by Markus Osenberg and me. The Laue-Diffraction measurement and evaluation was done by Dr. Anna Manzoni. Additional coin cell measurements and the data evaluatation was done by myself. The discussion of the results was done by Markus Osenberg, Dr. Eneli Härk, Dr. Luca Silvi, Prof. Dr. Matthias Ballauff, Dr. Sebastian Risse and me. The writing of the manuscript was done by Dr. Luca Silvi, Dr. Sebastian Risse, Prof. Dr. Matthias Ballauff and me. All authors joined the discussion of the data and the review process of the publication.

Chapter 5 was also a beamline-experiment at the ISIS Neutron and Muon source (proposal-nr. 1820188 - OFFSPEC). The proposal was written by me, together with Dr. Luca Silvi and Dr. Sebastian Risse. The deposition of the protective layer was done by Karsten Harbauer. Dr. Luca Silvi and I conducted the experiment at the neutron instrument together with the instrument Scientist Dr. Joshaniel Cooper. The data reduction was done by Dr. Joshaniel Cooper. The neutron data analysis script was created by me, also the analysis of the electrochemical data was done by me. Dr. Sebastian Risse and Dr. Luca Silvi supervised this and joined the discussion about the results. Additional coin cell measurements and the data evaluatation was done by myself. Dr. Sebastian Risse and Dr. Luca Silvi helped with supervision and discussions during the writing process of the chapter. A publication of this chapter will follow soon.

Appendix F

Statement of authorship/Selbstständigkeitserklärung

Selbstständigkeitserklärung:
Ich erkläre, dass ich die Dissertation selbstständig und nur unter Verwendung der von mir gemäß §7 Abs. 3 der Promotionsordnung der Mathematisch-Naturwissenschaftlichen Fakultät, veröffentlicht im Amtlichen Mitteilungsblatt der Humboldt-Universität zu Berlin Nr. 42/2018 am 11.07.2018 angegebenen Hilfsmittel angefertigt habe.

Potsdam, d. 26. Oktober 2020

.....
Arne Ronneburg

List of Figures

List of Tables

References

[1] Bruno Scrosati. History of lithium batteries. *Journal of Solid State Electrochemistry*, 15(7-8):1623–1630, 2011.

[2] Michal Osiak, Hugh Geaney, Eileen Armstrong, and Colm O'Dwyer. Structuring materials for lithium-ion batteries: Advancements in nanomaterial structure, composition, and defined assembly on cell performance. *Journal of Materials Chemistry A*, 2(25):9433–9460, 2014.

[3] Matthew T. McDowell, Seok Woo Lee, William D. Nix, and Yi Cui. 25th anniversary article: Understanding the lithiation of silicon and other alloying anodes for lithium-ion batteries. *Advanced Materials*, 25(36):4966–4985, sep 2013.

[4] Laurence Croguennec and M. Rosa Palacin. Recent achievements on inorganic electrode materials for lithium-ion batteries. *Journal of the American Chemical Society*, 137(9):3140–3156, 2015.

[5] Atetegeb Meazah Haregewoin, Aselefech Sorsa Wotango, and Bing Joe Hwang. Electrolyte additives for lithium ion battery electrodes: Progress and perspectives. *Energy and Environmental Science*, 9(6):1955–1988, 2016.

[6] Matthew Li, Jun Lu, Zhongwei Chen, and Khalil Amine. 30 Years of Lithium-Ion Batteries. *Advanced Materials*, 30(33):1–24, 2018.

[7] Kjell W. Schroder, Hugo Celio, Lauren J. Webb, and Keith J. Stevenson. Examining solid electrolyte interphase formation on crystalline silicon electrodes: Influence of electrochemical preparation and ambient exposure conditions. *Journal of Physical Chemistry C*, 116(37):19737–19747, 2012.

[8] John B. Goodenough and Kyu-sung Park. The Li-Ion Rechargeable Battery: A Perspective. *Journal of the American Chemical Society*, 135(4):1167–1176, 2013.

[9] E. Peled and S. Menkin. ReviewâSEI: Past, Present and Future. *Journal of The Electrochemical Society*, 164(7):A1703–A1719, 2017.

[10] Aiping Wang, Sanket Kadam, Hong Li, Siqi Shi, and Yue Qi. Review on modeling of the anode solid electrolyte interphase (SEI) for lithium-ion batteries. *npj Computational Materials*, 4(1), 2018.

[11] Yaguang Zhang, Ning Du, and Deren Yang. Designing superior solid electrolyte interfaces on silicon anodes for high-performance lithium-ion batteries. *Nanoscale*, 11(41):19086–19104, 2019.

[12] Yedukondalu Meesala, Anirudha Jena, Ho Chang, and Ru Shi Liu. Recent Advancements in Li-Ion Conductors for All-Solid-State Li-Ion Batteries. *ACS Energy Letters*, 2(12):2734–2751, 2017.

[13] Martin Winter, Brian Barnett, and Kang Xu. Before Li Ion Batteries. *Chemical Reviews*, 118(23):11433–11456, 2018.

[14] Zhe Li, Jun Huang, Bor Yann Liaw, Viktor Metzler, and Jianbo Zhang. A review of lithium deposition in lithium-ion and lithium metal secondary batteries. *Journal of Power Sources*, 254:168–182, 2014.

[15] Satishkumar B. Chikkannanavar, Dawn M. Bernardi, and Lingyun Liu. A review of blended cathode materials for use in Li-ion batteries. *Journal of Power Sources*, 248:91–100, 2014.

[16] Bruno Scrosati and Jürgen Garche. Lithium batteries: Status, prospects and future. *Journal of Power Sources*, 195(9):2419–2430, 2010.

[17] M N Obrovac and V L Chevrier. Alloy Negative Electrodes for Li-Ion Batteries. *Chemical Reviews*, 114(23):11444–11502, 2014.

[18] Maziar Ashuri, Qianran He, and Leon L. Shaw. Silicon as a potential anode material for Li-ion batteries: Where size, geometry and structure matter. *Nanoscale*, 8(1):74–103, 2016.

[19] Xifan Chen, Yuanzhi Zhu, Wenchao Peng, Yang Li, Guo Liang Zhang, Fengbao Zhang, and Xiaobin Fan. Direct exfoliation of the anode graphite of used Li-ion batteries into few-layer graphene sheets: a green and high yield route to high-quality graphene preparation. *Journal of Materials Chemistry A*, 5(12):5880–5885, 2017.

[20] Maria K Y Chan, C. Wolverton, and Jeffrey P. Greeley. First principles simulations of the electrochemical lithiation and delithiation of faceted crystalline silicon. *Journal of the American Chemical Society*, 134(35):14362–14374, 2012.

[21] Kun Feng, Matthew Li, Wenwen Liu, Ali Ghorbani Kashkooli, Xingcheng Xiao, Mei Cai, and Zhingwei Chen. Silicon-Based Anodes for Lithium-Ion Batteries From Fundamentals to Practical Applications. *SMALL*, 14:1702737–1702769, 2018.

[22] Xiuxia Zuo, Jin Zhu, Peter Müller-Buschbaum, and Ya-Jun Cheng. Silicon based lithium-ion battery anodes: A chronicle perspective review. *Nano Energy*, 31(October 2016):113–143, 2017.

[23] Meng Gu, Yang He, Jianming Zheng, and Chongmin Wang. Nanoscale silicon as anode for Li-ion batteries: The fundamentals, promises, and challenges. *Nano Energy*, 17:366–383, 2015.

[24] K W Schroder, H Celio, L J Webb, and K J Stevenson. Examining Solid Electrolyte Interphase Formation on Crystalline Silicon Electrodes: Influence of Electrochemical Preparation and Ambient Exposure Conditions. *Journal of Physical Chemistry C*, 116(37):19737–19747, 2012.

[25] Helena M. Braga, Adam Dębski, and Władysł aw Gąsior. Li-Si phase diagram: Enthalpy of mixing, thermodynamic stability, and coherent assessment. *Journal of Alloys and Compounds*, 616:581–593, 2014.

[26] Ram A Sharma and Randall N Seefurth. Thermodynamic Properties of the LithiumâSilicon System. *Journal of the Electrochemical Society*, 123(12):1763–1768, 1976.

[27] M N Obrovac and Leif Christensen. Structural Changes in Silicon Anodes during Lithium Insertion/Extraction. *Electrochemical and Solid-State Letters*, 7(5):A93, 2004.

[28] Jing Li and J. R. Dahn. An In Situ X-Ray Diffraction Study of the Reaction of Li with Crystalline Si. *Journal of the Electrochemical Society*, 154(3):A156–A161, 2007.

[29] M N Obrovac and L J Krause. Reversible cycling of crystalline silicon powder. *Journal of the Electrochemical Society*, 154(2):A103—-A108, 2007.

[30] Xiao Hua Liu, Li Zhong, Shan Huang, Scott X Mao, Ting Zhu, and Jian Yu Huang. Size-Dependent Fracture of Silicon Nanoparticles During Lithiation. *ACS nano*, 6(2):1522–1531, 2012.

[31] M T McDowell, I Ryu, S W Lee, C Wang, W D Nix, and Y Cui. Studying the kinetics of crystalline silicon nanoparticle lithiation with in situ transmission electron microscopy. *Advanced Materials*, 24(45):6034–6041, 2012.

[32] Zengsheng Ma, Tingting Li, Y. L. Huang, Jun Liu, Yichun Zhou, and Dongfeng Xue. Critical silicon-anode size for averting lithiation-induced mechanical failure of lithium-ion batteries. *RSC Advances*, 3(20):7398, 2013.

[33] B. Jerliu, L. Dörrer, E. Hüger, G. Borchardt, R. Steitz, U. Geckle, V. Oberst, M. Bruns, O. Schneider, and H. Schmidt. Neutron reflectometry studies on the lithiation of amorphous silicon electrodes in lithium-ion batteries. *Physical chemistry chemical physics*, 15(20):7777–84, 2013.

[34] V. L. Chevrier and J. R. Dahn. First Principles Model of Amorphous Silicon Lithiation. *Journal of The Electrochemical Society*, 156(6):A454, 2009.

[35] Shan Huang and Ting Zhu. Atomistic mechanisms of lithium insertion in amorphous silicon. *Journal of Power Sources*, 196(7):3664–3668, 2011.

[36] Xiao Hua Liu, He Zheng, Li Zhong, Shan Huang, Khim Karki, Li Qiang Zhang, Yang Liu, Akihiro Kushima, Wen Tao Liang, Jiang Wei Wang, Jeong Hyun Cho, Eric Epstein, Shadi A. Dayeh, S. Tom Picraux, Ting Zhu, Ju Li, John P. Sullivan, John Cumings, Chunsheng Wang, Scott X. Mao, Zhi Zhen Ye, Sulin Zhang, and Jian Yu Huang. Anisotropic swelling and fracture of silicon nanowires during lithiation. *Nano Letters*, 11(8):3312–3318, 2011.

[37] Seok Woo Lee, Matthew T. McDowell, Jang Wook Choi, and Yi Cui. Anomalous shape changes of silicon nanopillars by electrochemical lithiation. *Nano Letters*, 11(7):3034–3039, 2011.

[38] M J Chon, V A Sethuraman, A McCormick, V Srinivasan, and P R Guduru. Real-Time Measurements of Stress and Damage Evolution during Initial Electrochemical Lithiation and Delithiation of Crystalline Silicon. *Physical review letters*, 107(4):045503, 2011.

[39] Zhidan Zeng, Nian Liu, Qiaoshi Zeng, Seok Woo Lee, Wendy L. Mao, and Yi Cui. In situ measurement of lithiation induced stress in silicon nanoparticles using micro-raman spectroscopy. *Nano Energy*, pages 105–110, 2016.

[40] Jeannine R. Szczech and Song Jin. Nanostructured silicon for high capacity lithium battery anodes. *Energy and Environmental Science*, 4(1):56–72, 2011.

[41] Gabriel M. Veith, Loïc Baggetto, Robert L. Sacci, Raymond R. Unocic, Wyatt E. Tenhaeff, and James F. Browning. Direct measurement of the chemical reactivity of silicon electrodes with LiPF6-based battery electrolytes. *Chemical Communications*, 50(23):3081–3084, 2014.

[42] Yang Jin, Sa Li, Akihiro Kushima, Xiaoquan Zheng, Yongming Sun, Jin Xie, Jie Sun, Weijiang Xue, Guangmin Zhou, Jiang Wu, Feifei Shi, Rufan Zhang, Zhi Zhu, Kangpyo So, Yi Cui, and Ju Li. Self-healing SEI enables full-cell cycling of a silicon-majority anode with a coulombic efficiency exceeding 99.9%. *Energy and Environmental Science*, 10(2):580–592, 2017.

[43] S. C. DeCaluwe, B. M. Dhar, L. Huang, Y. He, K. Yang, J. P. Owejan, Y. Zhao, A. A. Talin, J. A. Dura, and H. Wang. Pore collapse and regrowth in silicon electrodes for rechargeable batteries. *Physical chemistry chemical physics*, 17(17):11301–12, 2015.

[44] Juchuan Li, Nancy J Dudney, Jagjit Nanda, and Chengdu Liang. *ACS Applied Materials &.*

[45] Langli Luo, Hui Yang, Pengfei Yan, Jonathan J. Travis, Younghee Lee, Nian Liu, Daniela Molina Piper, Se Hee Lee, Peng Zhao, Steven M. George, Ji Guang Zhang, Yi Cui, Sulin Zhang, Chunmei Ban, and Chong Min Wang. Surface-coating regulated lithiation kinetics and degradation in silicon nanowires for lithium ion battery. *ACS Nano*, 9(5):5559–5566, 2015.

[46] Gabriel M. Veith, Mathieu Doucet, Robert L. Sacci, Bogdan Vacaliuc, J. Kevin Baldwin, and James F. Browning. Determination of the Solid Electrolyte Interphase Structure Grown on a

Silicon Electrode Using a Fluoroethylene Carbonate Additive. *Scientific Reports*, 7(1):1–15, 2017.

[47] Sunny Hy, Yi Hsiu Chen, Ho Ming Cheng, Chun Jern Pan, Ju Hsiang Cheng, John Rick, and Bing Joe Hwang. Stabilizing Nanosized Si Anodes with the Synergetic Usage of Atomic Layer Deposition and Electrolyte Additives for Li-Ion Batteries. *ACS Applied Materials and Interfaces*, 7(25):13801–13807, 2015.

[48] Feifei Shi, Zhichao Song, Philip N. Ross, Gabor A. Somorjai, Robert O. Ritchie, and Kyriakos Komvopoulos. Failure mechanisms of single-crystal silicon electrodes in lithium-ion batteries. *Nature Communications*, 7(May):1–8, 2016.

[49] Gabriel M. Veith, Mathieu Doucet, J. Kevin Baldwin, Robert L. Sacci, Tyler M. Fears, Yongqiang Wang, and James F. Browning. Direct Determination of Solid-Electrolyte Interphase Thickness and Composition as a Function of State of Charge on a Silicon Anode. *Journal of Physical Chemistry C*, 119(35):20339–20349, 2015.

[50] Beatrix-Kamelia Seidlhofer, Bujar Jerliu, Marcus Trapp, Erwin Hüger, Sebastian Risse, Robert Cubitt, Harald Schmidt, Roland Steitz, and Matthias Ballauff. Lithiation of Crystalline Silicon As Analyzed by Operando Neutron Reflectivity. *ACS Nano*, 10(8):7458–7466, 2016.

[51] Chuntian Cao, Hans Georg Steinrück, Badri Shyam, and Michael F. Toney. The Atomic Scale Electrochemical Lithiation and Delithiation Process of Silicon. *Advanced Materials Interfaces*, 4(22):1–7, 2017.

[52] Sashini N. S. Hapuarachchi, Ziqi Sun, and Cheng Yan. Li-Ion Batteries: Advances in In Situ Techniques for Characterization of Failure Mechanisms of Li-Ion Battery Anodes (Adv. Sustainable Syst. 8-9/2018). *Advanced Sustainable Systems*, 2(8-9):1870038, 2018.

[53] Arne Ronneburg, Marcus Trapp, Robert Cubitt, Luca Silvi, Sébastien Cap, Matthias Ballauff, and Sebastian Risse. Surface structure inhibited lithiation of crystalline silicon probed with operando neutron reflectivity. *Energy Storage Materials*, 18(December 2018):182–189, 2018.

[54] Arne Ronneburg, Markus Osenberg, Kang Dong, André Hilger, Eneli Härk, Luca Silvi, Ingo Manke, Matthias Ballauff, and Sebastian Risse. Morphological evolution of a single crystal silicon battery electrode during lithiation and delithiation: An operando phase-contrast imaging study. *Energy Storage Materials*, 32(July):377–385, 2020.

[55] Carl H. Hamann and Wolf Vielstich. *Elektrochemie*. WILEY-VCH Verlag GmbH & Co. KGaA, 4th editio edition, 2005.

[56] William M. Haynes. CRC Handbook of Chemistry and Physics (Internet Version). *Taylor and Francis Boca Raton FL*, page 0, 2017.

[57] Jun Lu, Tianpin Wu, and Khalil Amine. State-of-the-art characterization techniques for advanced lithium-ion batteries. *Nature Energy*, 2(3):17011, 2017.

[58] Andrzej Lasia. *Electrochemical Impedance Spectroscopy and its Applications*. 2013.

[59] B.-Y. Chang and S.-M. Park. Electrochemical Impedance Spectroscopy. In *Annual Review Of Analytical Chemistry*, volume 3, pages 207–229. John Wiley {&} Sons, Inc., 2008.

[60] H. Schichlein, A. C. Müller, M. Voigts, A. Krügel, and E. Ivers-Tiffée. Deconvolution of electrochemical impedance spectra for the identification of electrode reaction mechanisms in solid oxide fuel cells. *Journal of Applied Electrochemistry*, 32(8):875–882, 2002.

[61] Francesco Ciucci and Chi Chen. Analysis of electrochemical impedance spectroscopy data using the distribution of relaxation times: A Bayesian and hierarchical Bayesian approach. *Electrochimica Acta*, 167:439–454, 2015.

[62] C. a. Schiller, F. Richter, E. Gülzow, and N. Wagner. Validation and evaluation of electrochemical impedance spectra of systems with states that change with time. *Physical Chemistry Chemical Physics*, 3(3):374–378, 2001.

[63] L. G. Parratt. Surface Studies of Solids by Total Reflection of X-rays. *Physical Review*, 95(2):359, 1954.

[64] Jean Daillant and Alain Gibaud. *X-ray and Neutron Reflectivity*. 2009.

[65] Hans-Joachim Eichler, Matthias Freyberger, Harald Fuchs, Florian Haug, Heinrich Kaase, Jürgen Kross, Heinwig Lang, Hannes Lichte, Heinz Niedrig, Tilman Pfau, Helmut Rauch, Wolfrang P. Schleich, Günter Schmahl, Erwin Sedlmayr, Felix Serick, Karl Vogel, Horst Weber, and Kurt Weber. Röntgenoptik. In Heinz Niedrig, editor, *Bergmann-Schaefer Lehrbuch der Experimentalphysik Band 3: Optik*, pages 1005–1007. Walter de Gruyter, Berlin/New York, 10 edition, 2004.

[66] Varley F. Sears. Neutron scattering lengths and cross sections. *Neutron News*, 3(3):26–37, 1992.

[67] Helmut Fritzsche. Neutron Reflectometry*. *Characterization of Materials*, (OCTOBER 2012), 2012.

[68] L Névot and P Croce. Caractérisation des surfaces par réflexion rasante de rayons X. Application à l'étude du polissage de quelques verres silicates. *Revue de Physique Appliquee*, 15(3):761–779, 1980.

[69] F. Abelès. La détermination de l'indice et de l'épaisseur des couches minces transparentes. *J. Phys. Radium,*, 11(7):310–314, 1950.

[70] Amitesh Paul, Thomas Krist, Anke Teichert, and Roland Steitz. Specular and off-specular scattering with polarization and polarization analysis on reflectometer V6 at BER II, HZB. *Physica B: Condensed Matter*, 406(8):1598–1606, 2011.

[71] Marcus Trapp. V6: The Reflectometer at BER II. *Journal of large-scale research facilities JLSRF*, 3:1–5, 2017.

[72] R. Cubitt and G. Fragnetto. D17: The new reflectometer at the ILL. *Applied Physics A: Materials Science and Processing*, 74(SUPPL.I):329–331, 2002.

[73] Thomas Saerbeck, Robert Cubitt, Andrew Wildes, Giuliana Manzin, Ken H. Andersen, and Philipp Gutfreund. Recent upgrades of the neutron reflectometer D17 at ILL. *Journal of Applied Crystallography*, 51(2):249–256, 2018.

[74] R. M. Dalgliesh, S. Langridge, J. Plomp, V. O. De Haan, and A. A. Van Well. Offspec, the ISIS spin-echo reflectometer. *Physica B: Condensed Matter*, 406(12):2346–2349, 2011.

[75] Franz Pfeiffer, Timm Weitkamp, Oliver Bunk, and Christian David. Phase retrieval and differential phase-contrast imaging with low-brilliance X-ray sources. *Nature Physics*, 2(4):258–261, 2006.

[76] Atsushi Momose. Recent Advances in X-ray Phase Imaging. 2005.

[77] David M. Paganin and Daniele Pelliccia. Tutorials on X-ray Phase Contrast Imaging: Some Fundamentals and Some Conjectures on Future Developments. 2019.

[78] Hongyu Chen, Melissa M. Rogalski, and Jeffrey N. Anker. Advances in functional X-ray imaging techniques and contrast agents. *Physical Chemistry Chemical Physics*, 14(39):13469–13486, 2012.

[79] A. Snigrev, I. Snigreva, V. Kohn, S. Kuznetsov, and I. Schelokov. On the possibilities of xâray phase contrast microimaging by coherent highâenergy synchrotron radiation. *Review of Scientific Instruments*, 66(12):5486–5492, 1995.

[80] Anna Burvall, Ulf Lundström, Per A. C. Takman, Daniel H. Larsson, and Hans M. Hertz. Phase retrieval in X-ray phase-contrast imaging suitable for tomography. *Optics Express*, 19(11):10359, 2011.

[81] David G. Lowe. Distinctive image features from scale-invariant keypoints. *International Journal of Computer Vision*, 60(2):91–110, 2004.

[82] Beat Münch, Pavel Trtik, Federica Marone, and Marco Stampanoni. Stripe and ring artifact removal with combined wavelet-Fourier filtering. *EMPA Activities*, 17(2009-2010 EMPA ACTIVITIES):34–35, 2009.

[83] W. Görner, M. P. Hentschel, B. R. Müller, H. Riesemeier, M. Krumrey, G. Ulm, W. Diete, U. Klein, and R. Frahm. BAMline: The first hard X-ray beamline at BESSY II. *Nuclear Instruments and Methods in Physics Research, Section A: Accelerators, Spectrometers, Detectors and Associated Equipment*, 467-468:703–706, 2001.

[84] D. Larcher and J-M M. Tarascon. Towards greener and more sustainable batteries for electrical energy storage. *Nature Chemistry*, 7(1):19–29, 2015.

[85] Sebastian Risse, Natalia A. Cañas, Norbert Wagner, Eneli Härk, Matthias Ballauff, and K. Andreas Friedrich. Correlation of capacity fading processes and electrochemical impedance spectra in lithium/sulfur cells. *Journal of Power Sources*, 323:107–114, 2016.

[86] M.J.D. Powell. An efficient method for finding the minimum of a function of several variables without calculating derivatives. *The Computer Journal*, 7(2):155–162, 1964.

[87] P.S. Pershan. X-ray or neutron reflectivity: Limitations in the determination of interfacial profiles. *Physical Review*, 50(3):2369–2372, 1994.

[88] Rainer Storn and Kenneth Price. Differential Evolution- A Simple and Efficient Adaptive Scheme for Global Optimization over Continuous Spaces. *Technical Report TR-95-012*, pages 1–12, 1995.

[89] Pauli Virtanen, Ralf Gommers, Travis E. Oliphant, Matt Haberland, Tyler Reddy, David Cournapeau, Evgeni Burovski, Pearu Peterson, Warren Weckesser, Jonathan Bright, Stéfan J. van der Walt, Matthew Brett, Joshua Wilson, K. Jarrod Millman, Nikolay Mayorov, Andrew R.J. Nelson, Eric Jones, Robert Kern, Eric Larson, C. J. Carey, Îlhan Polat, Yu Feng, Eric W. Moore, Jake VanderPlas, Denis Laxalde, Josef Perktold, Robert Cimrman, Ian Henriksen, E. A. Quintero, Charles R. Harris, Anne M. Archibald, Antônio H. Ribeiro, Fabian Pedregosa, Paul van Mulbregt, Aditya Vijaykumar, Alessandro Pietro Bardelli, Alex Rothberg, Andreas Hilboll, Andreas Kloeckner, Anthony Scopatz, Antony Lee, Ariel Rokem, C. Nathan Woods, Chad Fulton, Charles Masson, Christian Häggström, Clark Fitzgerald, David A. Nicholson, David R. Hagen, Dmitrii V. Pasechnik, Emanuele Olivetti, Eric Martin, Eric Wieser, Fabrice Silva, Felix Lenders, Florian Wilhelm, G. Young, Gavin A. Price, Gert Ludwig Ingold, Gregory E. Allen, Gregory R. Lee, Hervé Audren, Irvin Probst, Jörg P. Dietrich, Jacob Silterra, James T. Webber, Janko Slavič, Joel Nothman, Johannes Buchner, Johannes Kulick, Johannes L. Schönberger, José Vinícius de Miranda Cardoso, Joscha Reimer, Joseph Harrington, Juan Luis Cano Rodríguez, Juan Nunez-Iglesias, Justin Kuczynski, Kevin Tritz, Martin Thoma, Matthew Newville, Matthias Kümmerer, Maximilian Bolingbroke, Michael Tartre, Mikhail Pak, Nathaniel J. Smith, Nikolai Nowaczyk, Nikolay Shebanov, Oleksandr Pavlyk, Per A. Brodtkorb, Perry Lee, Robert T. McGibbon, Roman Feldbauer, Sam Lewis, Sam Tygier, Scott Sievert, Sebastiano Vigna, Stefan Peterson, Surhud More, Tadeusz Pudlik, Takuya Oshima, Thomas J. Pingel, Thomas P. Robitaille, Thomas Spura, Thouis R. Jones, Tim Cera, Tim Leslie, Tiziano Zito, Tom Krauss, Utkarsh Upadhyay, Yaroslav O. Halchenko,

and Yoshiki Vázquez-Baeza. SciPy 1.0: fundamental algorithms for scientific computing in Python. *Nature Methods*, 17(3):261–272, 2020.

[90] B. Jerliu, E. Hüger, L. Dörrer, B.-K. Seidlhofer, R. Steitz, V. Oberst, U. Geckle, M. Bruns, and H. Schmidt. Volume Expansion during Lithiation of Amorphous Silicon Thin Film Electrodes Studied by In-Operando Neutron Reflectometry. *Journal of Physical Chemistry C*, 118(18):9395–9399, 2014.

[91] Chuntian Cao, Hans Georg Steinrück, Badri Shyam, Kevin H Stone, and Michael F Toney. In Situ Study of Silicon Electrode Lithiation with X-ray Reflectivity. *Nano Letters*, 16(12):7394–7401, 2016.

[92] Alison L. Michan, Giorgio Divitini, Andrew J. Pell, Michal Leskes, Caterina Ducati, and Clare P. Grey. Solid Electrolyte Interphase Growth and Capacity Loss in Silicon Electrodes. *Journal of the American Chemical Society*, 138(25):7918–7931, 2016.

[93] Vijay A. Sethuraman, Venkat Srinivasan, and John Newman. Analysis of Electrochemical Lithiation and Delithiation Kinetics in Silicon. *Journal of The Electrochemical Society*, 160(2):A394–A403, 2013.

[94] Marc-Antoni Goulet, Maria Skyllas-Kazacos, and Erik Kjeang. The importance of wetting in carbon paper electodes for vanadium redox reactions. *Carbon*, 101:390–398, 2016.

[95] Elad Pollak, Gregory Salitra, Valentina Baranchugov, and Doron Aurbach. In situ conductivity, impedance spectroscopy, and ex situ Raman spectra of amorphous silicon during the insertion/extraction of lithium. *Journal of Physical Chemistry C*, 111(30):11437–11444, 2007.

[96] T.L. Kulova, A.M. Skundin, Yu.V. Pleskov, E.I. Terukov, and O.I. Kon'kov. Lithium insertion into amorphous silicon thin-film electrodes. *Journal of Electroanalytical Chemistry*, 600(1):217–225, 2007.

[97] A Nelson. Co-refinement of multiple-contrast neutron/X-ray reflectivity data using MOTOFIT. *Journal of Applied Crystallography*, 39:273–276, 2006.

[98] Amir H. Al-Bayati, Kevin G. Orrman-Rossiter, J.a. van den Berg, and D.G. Armour. Composition and structure of the native Si oxide by high depth resolution medium energy ion scatering. *Surface Science*, 241(1-2):91–102, 1991.

[99] Arnaud Bordes, Eric De Vito, Cédric Haon, Adrien Boulineau, Alexandre Montani, and Philippe Marcus. Multiscale Investigation of Silicon Anode Li Insertion Mechanisms by Time-of-Flight Secondary Ion Mass Spectrometer Imaging Performed on an in Situ Focused Ion Beam Cross Section. *Chemistry of Materials*, 28(5):1566–1573, 2016.

[100] J Browning, J Baldwin, J G Winiarz, H Kaiser, H Taub, R L Sacci, G M Veith, T M Fears, M Doucet, J F Browning, and J K S Baldwin. Evaluating the solid electrolyte interphase

formed on silicon electrodes: A comparison of ex situ X-ray photoelectron spectroscopy and in situ neutron reflectometry. *Phys. Chem. Chem. Phys.*, 00:1–3, 2016.

[101] Bertrand Philippe, Remi Dedryvere, Mihaela Gorgoi, Håkan Rensmo, Danielle Gonbeau, and Kristina Edstrom. Role of the LiPF 6 Salt for the Long-Term Stability of Silicon Electrodes in Li-Ion Batteries â A Photoelectron Spectroscopy Study. *Chemistry of Materials*, 25(3):394–404, 2013.

[102] Anton Tokranov, Ravi Kumar, Chunzeng Li, Stephen Minne, Xingcheng Xiao, and Brian W. Sheldon. Control and Optimization of the Electrochemical and Mechanical Properties of the Solid Electrolyte Interphase on Silicon Electrodes in Lithium Ion Batteries. *Advanced Energy Materials*, 6(8):1–12, apr 2016.

[103] Anton Tokranov, Brian W. Sheldon, Chunzeng Li, Stephen Minne, and Xingcheng Xiao. In Situ Atomic Force Microscopy Study of Initial Solid Electrolyte Interphase Formation on Silicon Electrodes for Li-Ion Batteries. *ACS Appl. Mater. Interfaces*, 6(9):6672–6686, 2014.

[104] Qianqian Liu, Chunyu Du, Bin Shen, Pengjian Zuo, Xinqun Cheng, Yulin Ma, Geping Yin, and Yunzhi Gao. Understanding undesirable anode lithium plating issues in lithium-ion batteries. *RSC Advances*, 6(91):88683–88700, 2016.

[105] Samuel Tardif, Ekaterina Pavlenko, Lucille Quazuguel, Maxime Boniface, Manuel Maréchal, Jean Sébastien Micha, Laurent Gonon, Vincent Mareau, Gérard Gebel, Pascale Bayle-Guillemaud, François Rieutord, and Sandrine Lyonnard. Operando Raman Spectroscopy and Synchrotron X-ray Diffraction of Lithiation/Delithiation in Silicon Nanoparticle Anodes. *ACS Nano*, 11(11):11306–11316, 2017.

[106] V. A. Sethuraman, V. Srinivasan, A. F. Bower, and P. R. Guduru. In Situ Measurements of Stress-Potential Coupling in Lithiated Silicon. *Journal of The Electrochemical Society*, 157(11):A1253, 2010.

[107] Bujar Jerliu, Erwin Hüger, Michael Horisberger, Jochen Stahn, and Harald Schmidt. Irreversible lithium storage during lithiation of amorphous silicon thin film electrodes studied by in-situ neutron re fl ectometry. *Journal of Power Sources*, 359:415–421, 2017.

[108] David Rehnlund, Fredrik Lindgren, Solveig Böhme, Tim Nordh, Yiming Zou, Jean Pettersson, Ulf Bexell, Mats Boman, Kristina Edström, and Leif Nyholm. Lithium trapping in alloy forming electrodes and current collectors for lithium based batteries. *Energy and Environmental Science*, 10(6):1350–1357, 2017.

[109] Matt Pharr, Kejie Zhao, Xinwei Wang, Zhigang Suo, and Joost J. Vlassak. Kinetics of initial lithiation of crystalline silicon electrodes of lithium-ion batteries. *Nano Letters*, 12(9):5039–5047, 2012.

[110] Florian Strauß, Erwin Hüger, Paul Heitjans, Thomas Geue, Jochen Stahn, and Harald Schmidt. Lithium Permeation through Thin Lithium-Silicon Films for Battery Applications Investigated by Neutron Reflectometry. *Energy Technology*, pages 1582–1587, 2016.

[111] Xiao Hua Liu, Li Zhong, Shan Huang, Scott X Mao, Ting Zhu, and Jian Yu Huang. Size-dependent fracture of silicon nanoparticles during lithiation.âSupporting Information1. *ACS nano*, 6(2):1522–31, 2012.

[112] Lucion Roiban, Siddardha Koneti, Takeshi Wada, Hidemi Kato, Francisco J. Cadete Santos Aires, Sergiu Curelea, Thierry Epicier, and Eric Maire. Three dimensional analysis of nanoporous silicon particles for Li-ion batteries. *Materials Characterization*, 124:165–170, 2017.

[113] Chenfei Shen, Mingyuan Ge, Anyi Zhang, Xin Fang, Yihang Liu, Jiepeng Rong, and Chongwu Zhou. Silicon(lithiated)-sulfur full cells with porous silicon anode shielded by Nafion against polysulfides to achieve high capacity and energy density. *Nano Energy*, 19:68–77, 2016.

[114] Kang Dong, Henning Markötter, Fu Sun, André Hilger, Nikolay Kardjilov, John Banhart, and Ingo Manke. In situ and Operando Tracking of Microstructure and Volume Evolution of Silicon Electrodes by using Synchrotron Xâray Imaging. *ChemSusChem*, 12(1):261–269, 2018.

[115] Chonghang Zhao, Takeshi Wada, Vincent De Andrade, Doga Gürsoy, Hidemi Kato, and Yu Chen Karen Chen-Wiegart. Imaging of 3D morphological evolution of nanoporous silicon anode in lithium ion battery by X-ray nano-tomography. *Nano Energy*, 52:381–390, 2018.

[116] J. M. Paz-Garcia, O. O. Taiwo, E. Tudisco, D. P. Finegan, P. R. Shearing, D. J.L. Brett, and S. A. Hall. 4D analysis of the microstructural evolution of Si-based electrodes during lithiation: Time-lapse X-ray imaging and digital volume correlation. *Journal of Power Sources*, 320:196–203, 2016.

[117] Oluwadamilola O. Taiwo, Thomas M.M. Heenan, Donal P. Finegan, Daniel J.L. Brett, Paul R. Shearing, Juan M. Paz-García, Stephen A. Hall, Rajmund Mokso, Pablo Villanueva-Pérez, and Alessandra Patera. Microstructural degradation of silicon electrodes during lithiation observed via operando X-ray tomographic imaging. *Journal of Power Sources*, 342:904–912, 2017.

[118] Y. Merla, E. Peled, F. Tariq, P. D. Lee, D. S. Eastwood, M. Biton, V. Yufit, K. Freedman, B. Wu, G. Offer, D. Golodnitsky, Z. Chen, and N. Brandon. In-Operando X-ray Tomography Study of Lithiation Induced Delamination of Si Based Anodes for Lithium-Ion Batteries. *ECS Electrochemistry Letters*, 3(7):A76–A78, 2014.

[119] Fu Sun, Henning Markötter, Ingo Manke, André Hilger, and Saad S Alrwashdeh. Applied Surface Science Complementary X-ray and neutron radiography study of the initial lithiation

process in lithium-ion batteries containing silicon electrodes. *Applied Surface Science*, 399:359–366, 2017.

[120] Lukas Zielke, Fu Sun, Henning Markötter, André Hilger, Riko Moroni, Roland Zengerle, Simon Thiele, John Banhart, and Ingo Manke. Synchrotron X-ray Tomographic Study of a Silicon Electrode Before and After Discharge and the Effect of Cavities on Particle Fracturing. *ChemElectroChem*, 3(7):1170–1177, 2016.

[121] M. J. Chon, V. A. Sethuraman, A. McCormick, V. Srinivasan, and P. R. Guduru. Real-time measurement of stress and damage evolution during initial lithiation of crystalline silicon. *Physical Review Letters*, 107(4):1–4, 2011.

[122] M. Jana and Raj N. Singh. A study of evolution of residual stress in single crystal silicon electrode using Raman spectroscopy. *Applied Physics Letters*, 111(6):0–5, 2017.

[123] Eric Sivonxay, Muratahan Aykol, and Kristin A Persson. The lithiation process and Li diffusion in amorphous SiO2 and Si from first-principles. *Electrochimica Acta*, page 135344, 2019.

[124] Tomoya Kawaguchi, Koki Shimada, Tetsu Ichitsubo, and Shunsuke Yagi. Surface-layer formation by reductive decomposition of LiPF6 at relatively high potentials on negative electrodes in lithium ion batteries and its suppression. *Journal of Power Sources*, 271:431–436, 2014.

[125] Anna T.S. Freiberg, Johannes Sicklinger, Sophie Solchenbach, and Hubert A. Gasteiger. Li2CO3 decomposition in Li-ion batteries induced by the electrochemical oxidation of the electrolyte and of electrolyte impurities. *Electrochimica Acta*, 346:136271, 2020.

[126] B. Jerliu, E. Hüger, L. Dörrer, B. K. Seidlhofer, R. Steitz, M. Horisberger, and H. Schmidt. Lithium insertion into silicon electrodes studied by cyclic voltammetry and: Operando neutron reflectometry. *Physical Chemistry Chemical Physics*, 20(36):23480–23491, 2018.

[127] Feifei Shi, Allen Pei, David Thomas Boyle, Jin Xie, Xiaoyun Yu, Xiaokun Zhang, Yi Cui, David Thomas, Jin Xie, Xiaoyun Yu, Xiaokun Zhang, and Yi Cui. Lithium metal stripping beneath the solid electrolyte interphase. *Proceedings of the National Academy of Sciences*, 115(34):8529–8534, 2018.

[128] T. D. Hatchard and J. R. Dahn. In Situ XRD and Electrochemical Study of the Reaction of Lithium with Amorphous Silicon. *Journal of The Electrochemical Society*, 151(6):A838–A842, 2004.

[129] Doron Aurbach. Impedance spectroscopy of lithium electrodes Part 1 . General behavior in propylene carbonate solutions and the correlation to surface chemistry and cycling efficiency. *Journal of Electroanalytical Chemistry*, 348:155–179, 1993.

[130] Doron Aurbach and Arie Zaban. The behaviour in propylene carbonate solutions - The significance of the data obtained. *Journal of Electroanalytical Chemistry*, 367(1-2):15–25, 1994.

[131] Kevin Rhodes, Nancy Dudney, Edgar Lara-Curzio, and Claus Daniel. Understanding the Degradation of Silicon Electrodes for Lithium-Ion Batteries Using Acoustic Emission. *Journal of the Electrochemical Society*, 157(12):A1354, 2010.

[132] Johannes Schindelin, Ellen T. Arena, Barry E. DeZonia, Mark C. Hiner, Kevin W. Eliceiri, Curtis T. Rueden, and Alison E. Walter. ImageJ2: ImageJ for the next generation of scientific image data. *BMC Bioinformatics*, 18(1):1–26, 2017.

[133] Ian H Witten, Eibe Frank, and Mark a Hall. *Data Mining: Practical Machine Learning Tools and Techniques*. 2011.

[134] Yang He, Daniela Molina Piper, Meng Gu, Jonathan J. Travis, Steven M. George, Se Hee Lee, Arda Genc, Lee Pullan, Jun Liu, Scott X. Mao, Ji Guang Zhang, Chunmei Ban, and Chongmin Wang. In situ transmission electron microscopy probing of native oxide and artificial layers on silicon nanoparticles for lithium ion batteries. *ACS Nano*, 8(11):11816–11823, nov 2014.

[135] Collin R. Becker, S. M. Prokes, and Corey T. Love. Enhanced Lithiation Cycle Stability of ALD-Coated Confined a-Si Microstructures Determined Using in Situ AFM. *ACS Applied Materials and Interfaces*, 8(1):530–537, 2016.

[136] Elmira Memarzadeh Lotfabad, Peter Kalisvaart, Kai Cui, Alireza Kohandehghan, Martin Kupsta, Brian Olsen, and David Mitlin. ALD TiO2 coated silicon nanowires for lithium ion battery anodes with enhanced cycling stability and coulombic efficiency. *Physical Chemistry Chemical Physics*, 15(32):13646–13657, 2013.

[137] A. Reyes Jiménez, R. Nölle, R. Wagner, J. Hüsker, M. Kolek, R. Schmuch, M. Winter, and T. Placke. A step towards understanding the beneficial influence of a LIPON-based artificial SEI on silicon thin film anodes in lithium-ion batteries. *Nanoscale*, 10(4):2128–2137, 2018.

[138] Yang Zhao and Xueliang Sun. Molecular Layer Deposition for Energy Conversion and Storage. *ACS Energy Letters*, 3(4):899–914, 2018.

[139] Jaewook Shin and EunAe Cho. Agglomeration Mechanism and a Protective Role of Al2O3 for Prolonged Cycle Life of Si Anode in Lithium-Ion Batteries. *Chemistry of Materials*, 30(10):3233–3243, 2018.

[140] Qing Ai, Deping Li, Jianguang Guo, Guangmei Hou, Qing Sun, Qidi Sun, Xiaoyan Xu, Wei Zhai, Lin Zhang, Jinkui Feng, Pengchao Si, Jun Lou, and Lijie Ci. Artificial Solid Electrolyte Interphase Coating to Reduce Lithium Trapping in Silicon Anode for High Performance Lithium-Ion Batteries. *Advanced Materials Interfaces*, 6(21):1901187, 2019.

[141] Sung Chul Jung and Young Kyu Han. How do Li atoms pass through the Al2O3 coating layer during lithiation in Li-ion batteries? *Journal of Physical Chemistry Letters*, 4(16):2681–2685, 2013.

[142] S. D. Beattie, T. Hatchard, A. Bonakdarpour, K. C. Hewitt, and J. R. Dahn. Anomalous, High-Voltage Irreversible Capacity in Tin Electrodes for Lithium Batteries. *Journal of The Electrochemical Society*, 150(6):A701, 2003.

[143] Tetsuya Kawamura, Shigeto Okada, and Jun-ichi Yamaki. Decomposition reaction of LiPF6-based electrolytes for lithium ion cells. *Journal of Power SourcesJournal of Power Sources*, 156(2):547 – 554, 2006.

[144] Huck Beng Chew, Binyue Hou, Xueju Wang, and Shuman Xia. Cracking mechanisms in lithiated silicon thin film electrodes. *International Journal of Solids and Structures*, 51(23-24):4176–4187, 2014.

[145] Ivana Hasa, Atetegeb Meazah Haregewoin, Liang Zhang, Wan-yu Tsai, Jinghua Guo, Gabriel M Veith, Philip N Ross, and Robert Kostecki. Electrochemical Reactivity and Passivation of Silicon Thin-Film Electrodes in Organic Carbonate Electrolytes. 2020.

[146] O. Arnold, J. C. Bilheux, J. M. Borreguero, A. Buts, S. I. Campbell, L. Chapon, M. Doucet, N. Draper, R. Ferraz Leal, M. A. Gigg, V. E. Lynch, A. Markvardsen, D. J. Mikkelson, R. L. Mikkelson, R. Miller, K. Palmen, P. Parker, G. Passos, T. G. Perring, P. F. Peterson, S. Ren, M. A. Reuter, A. T. Savici, J. W. Taylor, R. J. Taylor, R. Tolchenov, W. Zhou, and J. Zikovsky. Mantid - Data analysis and visualization package for neutron scattering and μ SR experiments. *Nuclear Instruments and Methods in Physics Research, Section A: Accelerators, Spectrometers, Detectors and Associated Equipment*, 764:156–166, 2014.

[147] Andrew R.J. Nelson and Stuart W. Prescott. Refnx: Neutron and X-ray reflectometry analysis in python. *Journal of Applied Crystallography*, 52:193–200, 2019.

[148] Matthew T. McDowell, Ill Ryu, Seok Woo Lee, Chongmin Wang, William D. Nix, and Yi Cui. Studying the kinetics of crystalline silicon nanoparticle lithiation with in situ transmission electron microscopy. *Advanced Materials*, 24(45):6034–6041, 2012.

[149] Xiao Hua Liu, Jiang Wei Wang, Shan Huang, Feifei Fan, Xu Huang, Yang Liu, Sergiy Krylyuk, Jinkyoung Yoo, Shadi A. Dayeh, Albert V. Davydov, Scott X. Mao, S. Tom Picraux, Sulin Zhang, Ju Li, Ting Zhu, and Jian Yu Huang. In situ atomic-scale imaging of electrochemical lithiation in silicon. *Nature nanotechnology*, 7:749–756, 2012.

[150] Mikhail V. Avdeev, Ivan A. Bobrikov, and Viktor I. Petrenko. Neutron methods for tracking lithium in operating electrodes and interfaces. *Physical Sciences Reviews*, 0(0):1–15, 2018.

[151] Yonghao An, Brandon C. Wood, Jianchao Ye, Yet Ming Chiang, Y. Morris Wang, Ming Tang, and Hanqing Jiang. Mitigating mechanical failure of crystalline silicon electrodes for lithium

batteries by morphological design. *Physical Chemistry Chemical Physics*, 17(27):17718–17728, 2015.

Wär nicht das Auge sonnenhaft, die Sonne
könnt es nie erblicken.

— **Johann Wolfgang von Goethe**
German writer and scientist